学位論文

Electronic Structures and Carrier Dynamics at Metal Oxide Surfaces

(金属酸化物の表面電子構造と表面におけるキャリアダイナミクス)

平成２６年１２月 博士（理学）申請
東京大学 大学院理学系研究科 物理学専攻
湯川 龍

Supervisor: Professor Iwao Matsuda

Abstract

Surface donors and acceptors yield band bending of a semiconductor surface because of the charge transfer between the bulk and the surface. When one focuses on an n-type semiconductor surface, surface donors yield downward band bending and a so-called accumulation layer, where electron carriers are accumulated within thin layers from the surface, is formed. With a large number of surface donors, the conduction band minimum (CBM) crosses the Fermi level and a two-dimensional electron gas (2DEG) is formed at the surface. On the other hand, surface acceptors yield upward band bending and a so-called depletion layer, where few electron carriers exist, is formed. The electronic structures and associated phenomena such as carrier transport and carrier dynamics can be controlled to some extent by appropriate surface treatments. Nowadays, methods to control surfaces and interfaces of oxide-metal semiconductors such as ZnO and $SrTiO_3$ (STO) have been developed, and the surfaces and interfaces of the oxide-metal semiconductors have attracted increasing attention due to their physical properties.

In this thesis, electronic structures and carrier dynamics of metal-oxide semiconductor surfaces related with their band bending structures have been studied by polarization-dependent angle-and time-resolved photoelectron spectroscopy (PES) measurements. Fundamental understanding of the electronic structures and carrier dynamics can be obtained by comparing experimentally obtained band bending structures with the theoretically calculated results. Therefore, as a first step a calculation model that is applicable to wide-gap semiconductors with multiple anisotropic subband structures is proposed. This model treats the subbands which have anisotropic energy dispersions using the anisotropic effective-mass approximations so that the model can easily be applied to accumulation layers of a variety of wide-gap semiconductor surfaces such as ZnO and STO. Second, metallization of hydrogen-adsorbed STO(001) surface has been experimentally proved by angle-resolved photoelectron spectroscopy (ARPES) and four-point-probes electrical conductivity measurements. Furthermore, polarization dependent ARPES studies have clarified the electronic structures of the 2DEG at the surface. Third, high-resolution ARPES results have showed spectral weight at the lower energy sides of 2DEG states of not only at the STO(001) surface, but also at the hydrogen-terminated ZnO($10\bar{1}0$) surface, indicating many-body interactions inherent to the 2DEG states. Finally, a relaxation process of surface photovoltage effects on a ZnO(0001) surface have been studied by time-resolved PES studies. A depletion-type

band structure and a thermionic relaxation process of the photoexcited carriers have been clarified.

Thus, studies in this thesis have clarified the electronic structures and carrier dynamics strongly related with their band bending structures at the metal oxide semiconductor surfaces.

Acknowledgements

It is my great pleasure to express my special gratitude to the following people for my doctoral thesis.

First of all, I would like to express my deepest gratitude to my supervisor, Prof. Iwao Matsuda, not only for giving me the chance of working in his group, but also having invited me to the exciting and splendid world of physics. I was given in pursuing science, the time he made available for explanations and discussions, as well as the excellent atmosphere in the group. His deep understanding of physics and exceptional experimental expertise has set a good example of an experimental physicist for me. His enthusiasm in physics, as well as serious working attitude, has created a very productive environment for the group. I feel lucky to have him as my advisor.

I would like to thank Dr. Susumu Yamamoto for his thoughtful advises on the experiments, writing manuscripts, and future academic plans. He always takes care of my research life at the SPring-8, and frequently drove me to restaurants and shopping stores from the SPring-8.

I also would like to thank Dr. Kenichi Ozawa, who introduced me the experimental technics and spent a great deal of time teaching me about the metal oxide semiconductors and English grammars. His productive advice makes the research more valuable one.

I need to thank Prof. Marie D'Angelo for reminding me of the sense of fun in the scientific research. Very enjoyable experiments with her encouraged me to decide to go to the doctoral course. She also helped me a lot at the SOLEIL and at the University of Paris in France.

I certainly think that the Matsuda laboratory was the best choice in my doctoral course. One of the reasons is owing to the presence of the very nice members in the lab. They hold a lot of parties and helped me a lot. Therefore, the laboratory was a really comfortable place for me. I would like to thank Dr. Manami Ogawa, who taught me not only time-of-flight systems but also the history of Europe, and Mr. Fumitaka Nakamura who introduced me the angle-resolved photoemission systems. He always drove me to the photon factory from the Kashiwa campus. I also like to thank Mr. Shingo Yamamoto who has planed exotic events as presented by "BLUE NOTE KASHIWA". Many ideas were generated by discussions with him. I would like to

thank Mr. Yuya Kubota for taking care of me and the laboratory members, Ms. Ro-Ya Liu for advising me about physics theory, Mr. Kazushi Fujikawa for helping the experiments at SPring-8, Mr. Takashi Someya for getting me to play sports and brewing delicious coffees, Mr. Kazuma Akikubo who has never declined any of my suggestions nor invitations, Mr. Suguru Itou for teaching me the Feynman diagram and shearing some space on his desk, Ms. Kaori Takeuchi for taking care of the laboratory members. I also need to thank Mr. Rei Hobara who has been the adviser of electronic systems and computer programs.

I am grateful to Mr. Masami Fujisawa, Ms. Ayumi Harasawa, Ms. Akiko Fukushima, Ms. Yumiko Aihara, Ms. Misa Harada, Ms. Yoshie Kaneko, Ms. Akiko Someya. Their kind support for the experiments and travels enabled me to concentrate on my research.

I am grateful to the members, Prof. Yoshihisa Harada, Dr. Jun Miyawaki, Dr. Hideharu Niwa, Mr. Hisao Kiuchi, Mr. Junki Nakajima, Mr. Naoki Itamoto, Prof. Hiroki Wadati, Dr. Kou Takubo, Mr. Tomoyuki Tsuyama, Dr. Koji Horiba, Dr. Naoka Nagamura, Prof. Tadashi Abukawa, Prof. Takeaki Sakurai, Ms. Misa Harada, Ms. Mihoko Araki, Ms. Yukimi Yamamoto. They have spared a great deal of time for helping and teaching me at SPring-8.

I would like to thank Prof. Shu-Jung Tang and his group members Mr. Chung Huang Lin, and Mr. Meng-Kai Lin for supporting my experiments and stay in Taiwan. Deep understanding of physics has been obtained by discussion with them.

I am also grateful to Prof. Tai-Chang Chiang and his group members Dr. Tom J. Miller, Dr. Guang Bian, Mr. Wong Man-Hong, Mr. Caizhi Xu, Ms. Jie Ren, Mr. Longxiang Zhang, Mr. Saohan Wang, Mr. Gazzy Weng, Ms. Xinyue Fang for the valuable discussion on ARPES results. They took care of my three month stay at University of Illinois at Urbana Champaign and at Synchrotron Radiation Center.

I need to thank Prof. Nobuhiko Sarukura and his group members Dr. Toshihiko Shimizu, Mr. Yuki Minami, Mr. Ren Arita who have supported our time-resolved photoluminescence experiments at Osaka university.

I also would like to thank Prof. Shuji Hasegawa and Prof. Toru Hirahara for the help in the four-probes electrical conductivity experiments. It was a very nice chance for me to learn the systems and physics of the surface electrical conductivities.

I would like to thank Prof. Fumio Komori and his group members: Dr. Toshio Miyamachi, Dr. Yaji Koichiro, Mr. Takusi Iimori, Dr. Koichiro Ienaga, Dr. Masamichi

Yamada, Mr. Sunghun Kim, Mr. Yukio Takahashi. They brought us the precious chance to practice presentation skills at meeting. They also gave me the fundamental knowledge of STM systems.

I also want to thank Prof. Hiroshi Sakama, Mr. Masato Emori, Prof. Hiroshi Daimon, Mr. Satoshi Kitagawa for their help with the time-resolved PES experiments and discussions at SPring-8.

I need to thank the professors and their group members at Hiroshima university: Prof. Kenya Shimada, Dr. Hideaki Iwasawa, Dr. Schwier Eike Fabian, Dr. Jian Jiang, Mr. Taiki Horike, Mr. Taiki Horike, Mr. Yorito Nagata, Prof. Taniguchi Masaki, and Prof. Hirofumi Namatame for helping our high-resolution ARPES experiments at BL-1 beamline of HiSOR, giving me the knowledge of polaronic effect, and helping our research life in Hiroshima.

I would like to thank Prof. Hiroshi Kumigashira and Dr. Kohei Yoshimatsu for taking care of our ARPES measurements at BL-28 at Photon Factory. They also gave me precious samples grown by the pulsed laser deposition method.

I am happy to thank collaborators in the synchrotron center SOLEIL, France: Dr. Fausto Sirotti, Dr. Mathieu Silly, and Dr. Amina Taleb-Ibrahimi, and also collaborators in the synchrotron center ELETTRA, Italy: Dr. Carlo Carbone, Dr. Paolo Moras, and Dr. Polina Sheverdyaeva for their thoughtful help of our ARPES experiments, giving experimental advices, and showing us around the beautiful towns. I also thank Dr. Yoshiyuki Ohtsubo, who taught me how to make good analysis program at SOLEIL.

I am grateful to professers in ISSP: Prof. Akito Kakizaki, Dr. Yasuo Takeichi, Prof. Takeo Kato, Prof. Yukio Hasegawa, Dr. Yasuo Yoshida, Dr. Yukio Ishida, who have taught me the knowledge on fundamental physics to advanced technological applications.

I need to thank Prof. Tetsuya Hasegawa who has been taking care of my course work of the Advanced Leading Graduate Course for Photon Science (ALPS). His advice encouraged my research life.

Finally, I would like to thank my parents as well as my brother for their kind support and understanding during all my studies.

Contents

Abbreviations

1D, 2D, 3D	**One**- **Two**- **Three**-**d**imensional
2DEG	**Two**-**D**imensional **E**lectron **G**as
2DEL	**Two**-**D**imensional **E**lectron **L**iquid
2D-IR	**Two**-**d**imensional **I**offe-**R**egel
4PP	**Four**-**P**oint **P**robes
AEA	**A**nisotropic **E**ffective-mass **A**pproximations
AES	**A**uger **E**lectron **S**pectroscopy
ARPES	**A**ngle-**R**esolved **P**hoto**e**lectron **S**pectroscopy
ARTOF	**A**ngle-**R**esolved **T**ime **o**f **F**light
CBM	**C**ondction **B**and **M**inimum
cph	**c**oherent **ph**onon
e	**e**lectron
EDC	**E**nergy **D**istribution **C**urve
EHP	**E**lectron-**H**ole **P**lasma
fcc	**f**ace-**c**entered **c**ubic
FEL	**F**ree **E**lectron **L**aser
FM	**F**erro-**m**agnetic
FWHM	**F**ull-**W**idth at **H**alf-**M**aximum
HAXPES	**H**ard **X**-ray **P**hoto**e**lectron **S**pectroscopy
h	**h**ole
hcp	**h**exagonal **c**losed-**p**acked structure
HEMT	**H**igh **E**lectron **M**obility **T**ransistor
HHG	**H**igh **H**armonic **G**eneration
IGS	**I**n-**G**ap **S**tate

LASER	**L**ight **A**mplification by **S**timulated **E**mission of **R**adiation
LDA	**L**ocal **D**ensity **A**pproximations
LEED	**L**ow-**E**nergy **E**lectron **D**iffraction
LT	**L**ow **T**emperature
MS	**M**etallic **S**tates
MTFA	**M**odified **T**homas-**F**ermi **A**pproximation
OAS	**O**ptical **A**dsorption **S**pectroscopy
PES	**P**hoto**e**lectron **S**pectroscopy
ph	**ph**onon
RT	**R**oom **T**emperature
SCL	**S**pace **C**harge **L**ayer
SHG	**S**econd **H**armonic **G**eneration
SO	**S**pin **O**rbit
SPV	**S**urface **P**hoto**v**oltage
SR	**S**ynchrotron **R**adiation
STO	**$SrTiO_3$**
STM	**S**canning **T**unneling **M**icroscope
UHV	**U**ltra **H**igh **H**igh **V**acuum
UV	**U**ltra**V**iolet
VBM	**V**alence **B**and **M**aximum
XAS	**X**-ray **A**bsorption **S**pectroscopy
XPS	**X**-ray **P**hotoelectron **S**pectroscopy

Physical Constants

Speed of Light in vacuum	c	$=$	$2.99792458 \times 10^{8}\ \mathrm{m \cdot s^{-1}}$
Planck's constant	h	$=$	$6.62606957 \times 10^{-34}\ \mathrm{J \cdot s}$
reduced Planck's constant	$\hbar = \frac{h}{2\pi}$	$=$	$1.054571726 \times 10^{-34}\ \mathrm{J \cdot s}$
Boltzmann constant	k_{B}	$=$	$1.3806488 \times 10^{-23}\ \mathrm{J \cdot K^{-1}}$
electron mass	m_{e}	$=$	$9.10938188 \times 10^{-31}\ \mathrm{kg}$
elementary charge	e	$=$	$1.602176462 \times 10^{-19}\ \mathrm{C}$
Bohr radius	a_0	$=$	$5.291772083 \times 10^{-11}\ \mathrm{m}$
Hartree energy	E_h	$=$	$4.35974381 \times 10^{-18}\ \mathrm{J}$
Vacuum permeability	$\mu_0 = 4\pi \times 10^{-7}$	$=$	$1.2566370614 \times 10^{-6}\ \mathrm{N \cdot A^{-2}}$
Vacuum permittivity	$\epsilon_0 = \frac{1}{\mu_0 c^2}$	$=$	$8.854187817620 \times 10^{-12}\ \mathrm{F \cdot m^{-1}}$

The International System of Units (Le Système International d'Unités: SI units) is mainly used in this thesis. Some of the useful conversion formulae are listed in this page.

1 eV = $1.60217657 \times 10^{-19}$ J

$h\nu$ [eV] = $\frac{hc}{e}\frac{1}{\lambda[nm]} \simeq \frac{1240}{\lambda[nm]}$

1 Å = 10^{-10} m

0.1 $Å^{-1}$ = 1 nm^{-1}

$k_{\parallel}[\mathrm{nm}^{-1}] = 5.12\sqrt{E_k[\mathrm{eV}]}\sin\theta$

$k_{\parallel}[Å^{-1}] = 0.512\sqrt{E_k[\mathrm{eV}]}\sin\theta$

1 in (inch) = 25.4 mm

1 mi (mile) = 1609.344 m

1 Pa = 1 N/m^2 = 1×10^{-2} mbar = 7.5×10^{-3} Torr

1 atm = 101325 Pa = 1013.25 mbar = 760 Torr

1 T = 10^4 G (Gauss)

Earth's magnetic field = $24-66 \times 10^{-6}$ T = 0.24−0.66 G

0 K (Kelvin) = −273.15 °C (Celsius) = 459.67 °F (Fahrenheit)

x K = $x - 273.15$ °C = $\frac{9}{5}(x - 273.15) + 32$ °F

273.15 K = 0 °C = 32.0 °F

1 L (Langmuir) = 1×10^{-6} Torr s $\simeq 1.3 \times 10^{-4}$ Pa s

Symbols

$\boldsymbol{A}$	Vector potential of the electromagnetic field
A_{spectral}	Spectral function
E	Energy
E_{A}	Bulk accepter level
E_{B}	Binding energy
$\mathbb{E}_c$	Critical electric field
E_{D}	Bulk donor level
E_{F}	Fermi energy
E_k	Kinetic energy of a photoelectron in the vacuum
$E_{k,\mathrm{F}}$	Kinetic energy of a photoelectron emitted from the Fermi edge in the vacuum
E_k^{A}	Kinetic energy of a photoelectron detected at an electron analyzer
$E_{k,\mathrm{F}}^{\mathrm{A}}$	Kinetic energy of a photoelectron emitted from the Fermi edge at an electron analyzer
E_{pass}	Pass energy
f_{FD}	Fermi-Dirac distribution function
$h\nu$	Photon energy
I^s	ARPES intensities taken with s-polarized photons
I^p	ARPES intensities taken with p-polarized photons
k	Electron wavenumber
k_{F}	Fermi wavenumber
V_0	Inner potential
V_{s}	Surface potential

V_{s}	Surface potential during relaxation
V_{SPV}	Surface photovoltage shift
N_{A}	Bulk accepter density
N_{A}^{-}	Ionized accepter density
N_{C}	Conduction band density of states
n_{2D}	Density of 2D electrons
N_{D}	Bulk donner density
N_{D}^{+}	Ionized donor density
N_{ss}	Surface carrier density
N_{V}	Valence band density of states
L^{A}	Mean-free-path of an analyzing photoelectron
L_{D}	Depth of the depletion layer
L_{th}	Thermal length
p_s	Hall density trapped at a surface
R	Electrical resistance
R_{S}	Sample resistance
T	Temperature
t_{h}	Electron hopping integral
w_{if}	Transition probability from initial to final states
η	Ideality factor
μ	Carrier mobility
Σ	Self-energy of an electron
σ_{1D}	Wire conductivity
σ_{2D}	Sheet conductivity
σ_{3D}	Bulk conductivity
$\Delta\sigma$	Sheet conductivity change
$\Delta\sigma_{\mathrm{sat}}$	$\Delta\sigma$ after a saturation
σ_{th}	Thermal cross section of capturing an electron
τ_0	Carrier lifetime in the absence of a band bending effect
τ_{s}	Relaxation time in the absence of SPV
Φ	Work function of a solid
Φ_{A}	Work function of an analyzer

Chapter 1

Introduction

1.1 Background of the present study

Surface physics has in these decades become a fundamental branch of condensed matter research. The surface of a solid is a particular type of an interface where it contacts other solids, the atmosphere, or the vacuum. The development of experimental techniques such as photoelectron spectroscopy, Hall effect, and scanning tunneling microscopy have revealed the exotic nature of surface physics such as low-dimensional electron liquids, Rashba effects and photoresponsivity. Many phenomena at the surfaces cannot be understood without a profound knowledge of the surface, interface effects, and underlying physics. Obviously, surface physics becomes more and more important in solid physics, because the recent development of electronic devices require nano-scale electronic parts, which surfaces affect strongly the electronic properties of the materials. Thus, it is natural that we are attracted by surface science.

A band bending structure at a semiconductor surface strongly affects the properties of surface physics. Potential energies of semiconductor surfaces are easily shifted by their surface treatments. Surfaces are terminated by vacuum, adsorbates, or ions with different electric charges from those in the bulk. In order to conserve a charge neutrality, electrons or holes are accumulated at the semiconductor surface and a charged layer, a so called "space charge layer" (SCL), is formed [1]. When one focuses on an n-type semiconductor surface, surface acceptors yield upward band bending and a so-called depletion layer is formed. Surface donors, on the other hand, yield downward band bending and a so-called accumulation layer, where electron carriers are accumulated within a thin layer from the surface, is formed. If there exist a sufficient amount of

surface donors and if a conduction band minimum (CBM) crosses the Fermi level, accumulated electrons form metallic states at the surface. Since the electrons at the accumulation layer is confined along the surface normal direction, the electrons can transport only in directions parallel to the surface. The electronic properties of these confined electrons are described by the two-dimensional electron gas (2DEG) model where electrons can move freely in two dimensions. The 2DEG is one of the important factors to understand a high-electron-mobility transistor (HEMT) [2] and quantum hall effect [3, 4]. A lot of experimental and theoretical effort has been devoted to obtain the 2DEG structures at a variety of semiconductor surfaces and interfaces of, e.g., Si, Ge, InAs, and GaAs for many decades [1].

Over the past forty years, accumulation layers formed at hydrogen-adsorbed ZnO surfaces have been studied [5–12]. Heiland and Kunstmann reported sheet conductivity changes of the ZnO($000\bar{1}$) and ZnO(0001) surfaces by adsorption of atomic H [5]. A first-principles investigation showed hydrogen acts as a shallow donor in ZnO [6]. Angle-resolved photoelectron spectroscopy (ARPES) studies showed that metallic states are formed at ZnO($10\bar{1}0$) and ZnO($000\bar{1}$) surfaces [10–12]. A 2DEG was found at an interface of $LaAlO_3/SrTiO_3$ [13] and attracted much attention over ten years [13–17], because a high carrier mobility exceeding 10,000 $cm^2V^{-1}s^{-1}$ [13] and a superconductivity [18] of the 2DEGs were observed. Recent ARPES results revealed that 2DEGs are formed at a cleaved and ultraviolet light-irradiated $SrTiO_3(001)$ surfaces [19–21]. The 2DEGs at the surfaces and interfaces consist of electrons in the Ti $3d$ bands [13, 19–23]. Therefore, the 2DEGs show a lot of intriguing physical properties such as anisotropy, strong-correlation, and Rashba effect [19–21, 23]. However, these 2DEGs at $SrTiO_3(001)$ surfaces may be induced by the oxygen vacancies, which can be scatterers for conducting electrons [19, 20]. Therefore, formation of 2DEG at a well defined $SrTiO_3(001)$ is required for the application to the future electronic devices.

Many of the metal-oxide semiconductors have wide band gaps exceeding 3.2 eV and have transparency to visible light. Metal-oxide semiconductor surfaces and interfaces attract an increasing attention for their photoresponsivity such as photocatalytic effect, photovoltaic effect and photoluminescence. A variety of time-resolved experiments have been conducted on ZnO crystals to investigate the carrier dynamics. However, very little has been reported about the band-bending structures of the surfaces. Since the electron-hole recombination time, which is the key factor for the photocatalytic efficiency and photovoltaic effect, is strongly related with the band bending structure at the surface, fundamental knowledge to relate the carrier recombination time with the band bending structure is called for.

1.2 Purpose of the present study

The main purpose of this thesis is to clarify carrier dynamics and electronic structures at metal-oxide semiconductor surfaces related with their band bending structures. The objective of this thesis is fourfold.

The first objective is to construct a theoretical model for the accumulation layers at the surfaces of *n*-type oxide semiconductors such as $SrTiO_3$ and ZnO. Previous theoretical models have mainly focused on the accumulation layers of semiconductors which have subbands with isotropic *s*-orbital symmetry, and are hardly applicable for an accumulation layer of a $SrTiO_3$ surface which has subbands with anisotropic *d*-orbital symmetry. The *ab initio* calculation is a powerful method to obtain complicated band structures of solids. However, the calculation requires a lot of time and can easily be a black box. Therefore, a much simpler but reasonable calculation method has been required.

The second objective is to prove metallization of the $SrTiO_3(001)$ surface by hydrogen adsorption and clarify the electronic structures by the polarization-dependent ARPES measurements. Recently, 2DEGs at $SrTiO_3$ surfaces were experimentally discovered at the cleaved and ultraviolet-light irradiated $SrTiO_3(001)$ surfaces [19, 20]. However, these 2DEGs may be generated by electron doping from oxygen vacancies at the surfaces that can be electron scatterers. Therefore, the realization of the 2D metallization at a well-defined $SrTiO_3$ surface has been desired for. *Ab initio* calculations predicted that 2DEGs are formed at hydrogen adsorption on a SrO- or TiO_2-terminated $SrTiO_3(001)$ surface. Metallization of the surface can be confirmed by surface electrical conductivity measurements with four-point-probes system. Moreover, the electronic structure of the surface can be studied by polarization-dependent ARPES measurements. In this respect, transport measurements and polarization-dependent ARPES measurements were performed.

The third objective is to clarify the detailed electronic properties of 2DEGs at hydrogen-adsorbed $ZnO(10\bar{1}0)$ and $SrTiO_3(001)$ surfaces. ARPES studies showed spectral weight at the lower energy sides of the two-dimensional metallic states at both the surfaces. This spectral weight may be originated from many-body interactions [19]. To clarify the electronic structures at the hydrogen-adsorbed $SrTiO_3(001)$ and $ZnO(10\bar{1}0)$ surfaces, high-resolution ARPES measurements have been performed. The ARPES results of the $H/SrTiO_3(001)$ surface are compared with those of the $H/ZnO(10\bar{1}0)$ surface.

The forth objective of this thesis to study the electron-hole recombination process at the ZnO(0001) surface. Irradiation of laser light with the energy exceeding the bulk band gap of a semiconductor induce electron-hole pairs. When the band of an n-type semiconductor is bent upward at the surface, the photoexcited electrons and holes transfer to the bulk side and the surface side, respectively, by the potential gradient near the surface. The transfer of these carriers induces surface photovoltage (SPV) effects. By time-resolved photoelectron spectroscopy measurements of the ZnO(0001) surface, the carrier transfer and recombination process have been clarified.

1.3 Structure of this thesis

Chapter 2 describes the fundamental physics and theory used in the following chapters. The approaches to calculate the band bending structures and corresponding subband structures are briefly presented. The theory to describe the relaxation process of the SPV effect is also described in this chapter.

Chapter 3 describes experimental systems and techniques. In order to clarify the electronic structure and carrier dynamics at the metal-oxide surfaces, a variety of experiments have been carried out with methods such as ARPES, Hall effect, low-energy electron diffraction (LEED), optical absorption spectroscopy (OAS), and four-point-probes (4PP) measurements. Especially, experimental methods of ARPES and surface electrical conductivity measurements with 4PP are described in this chapter.

Chapter 4 describes a simplified model for calculation of an accumulation layer at n-type wide-gap semiconductor surfaces. The model presented here can be applied for a semiconductor in which subband are originated with anisotropic d-orbitals.

Chapter 5 describes experimental realization of hydrogen-induced metallization at a $SrTiO_3(001)$ surface. Metal-insulator transition at the $SrTiO_3(001)$ surface has been experimentally demonstrated by ARPES and electrical conductivity with 4PP measurements. The electronic states forming in the band gap (in-gap states: IGSs) and electronic structures at the valence bands are based on the polarization-dependent ARPES results.

The origin of the ARPES intensities observed at $SrTiO_3(001)$ and $ZnO(10\bar{1}0)$ surfaces is discussed in Chapter 6. With high-resolution ARPES results and theoretical calculations, the detailed electronic and band bending structures of their surfaces are discussed.

Chapter 7 describes the time-resolved PES results on SPV effect measured on a ZnO(0001) surface. The upward band bending structure of the surface is theoretically calculated with the parameters obtained by Hall and PES measurements. The recombination process of electron-hole pairs and carrier lifetime are discussed based on the delay-time and pumping-laser-power dependent PES results.

In Chapter 8, the major findings presented in this thesis are summarized and the future prospect are discussed.

Chapter 2

Basic principles

2.1 Space-charge layer at semiconductor surfaces

Throughout a semiconductor film and surface, a potential variation $V(z)$ is obtained by solving the Poisson equation[1] [1, 24]:

$$\frac{d^2V(z)}{dz^2} = -\frac{e^2}{\epsilon(z)\epsilon_0}\{N_{\rm D}^+(z) \ - N_{\rm A}^-(z) \ - n(z) \ + p(z)\}, \tag{2.1}$$

where e denotes the elementary charge, $N_{\rm D}^+(z)$ is the ionized donor density, $N_{\rm A}^-(z)$ is the ionized acceptor density, $n(z)$ is the electron density in the conduction band, and $p(z)$ is the hole density in the valence band. $\epsilon(z)$ and ϵ_0 are the relative and vacuum dielectric constants, respectively. Here, z is set normal to the surface and $z = 0$ at the surface. Figure 2.1 illustrates band diagrams of n-type semiconductors. $E_{\rm C}$, $E_{\rm D}$, and $E_{\rm V}$ denote the energies of the conduction band minimum (CBM), the bulk donor level, and the valence band maximum (VBM), respectively. The densities of ionized donors are distributed in an energy range of about $4k_{\rm B}T$ from the Fermi level ($E_{\rm F}$) by the Fermi statistics:

$$N_{\rm D}^+(z) = N_{\rm D} - N_{\rm D}\frac{1}{1+\exp\{(E_{\rm D}(z)-E_{\rm F})/k_{\rm B}T\}}, \tag{2.2a}$$

$$N_{\rm A}^-(z) = N_{\rm A} - N_{\rm A}\frac{1}{1+\exp\{(E_{\rm F}-E_{\rm A}(z))/k_{\rm B}T\}}, \tag{2.2b}$$

where $N_{\rm D}$ is the bulk donor density, and $N_{\rm A}$ and $E_{\rm A}$ are the bulk acceptor density and its energy level. $k_{\rm B}$ is the Boltzmann constant and T is the temperature. From Eq.

[1] $V(z)$ takes the dimension of energy in this thesis.

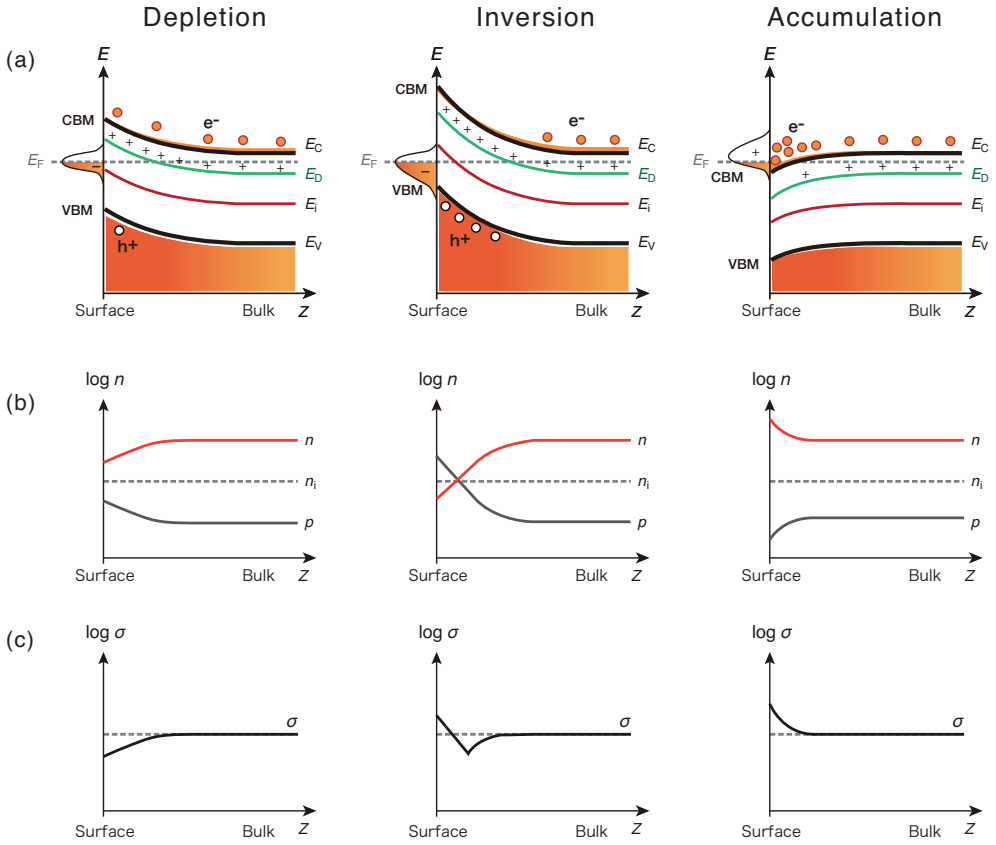

FIGURE 2.1: Schematic band diagrams of space charge layers for n-type semiconductor [1]. Band bending (a), carrier densities n and p (b), and local conductivities σ are shown for the depletion layer, the inversion layer, and the accumulation layer of an n-type semiconductor. The dotted line in (a) shows the Fermi energy. The electron carriers and hole carriers are shown by orange circles and white circles, respectively.

(2.2a), one obtains that if $E_D(z) - E_F \gg k_B T$, $N_D^+(z) \approx N_D$, and if $E_D(z) - E_F \ll k_B T$, $N_D^+(z) \approx N_D \exp\{(E_D(z) - E_F)/k_B T\}$. In the bulk of a semiconductor, where the location is deep enough from the surface and is not affected by the surface charges, no potential variation exists and the left hand side of Eq. (2.1) is zero $[\frac{dV(z)}{dz} = 0]$. In an n-type semiconductor, in which electron donors are doped in the crystal and the acceptors and hole densities can be ignored $[N_A^-(z) = 0, p = 0]$, Eq. (2.1) is simplified to

$$n = N_D^+. \tag{2.3}$$

One obtains that the carrier density is equal to the ionized donor density in the bulk of a semiconductor.

At a semiconductor surface, the continuous crystal structure is terminated by the

vacuum or adsorbed ions and the band-bending structure at the surface is different form that in the bulk. In order to conserve the charge neutrality at the surface, electron carriers or holes are accumulated at the surface and create a space charge layer (SCL). As a consequence, the band of the semiconductor surface bends upward or downward (so called band bending) as illustrated in Fig. 2.1 [1]. An adsorbed ions become surface donors or acceptors. When the surface ions work as acceptors, the acceptors themselves are negatively charged. The electric field induced by the negative charges repels the electron carriers at the surface, or attracts holes from the bulk, and holes are accumulated near the surface [Fig. 2.1(b)]. The decrease of the electron carriers reduces the conductivity at the surface [Fig. 2.1(c)]. If a large number of acceptors adsorb at the surface, strong band bending is induced and finally the number of hole carriers exceeds the number of electron carriers. In this case, holes are the major carriers of the surface conductivity. This type of the SCL is called an inversion layer. When surface donors exist at a semiconductor surface, the surface donors themselves are positively charged, and attract electron carriers from the bulk or repel hole carriers. As a consequence, electron carriers are accumulated near the surface. This type of the SCL is called an accumulation layer. At an accumulation layer, a large number of electron carriers can be accumulated near the surface and a high electrical conductivity at the surface is expected.

It should be noted that the same discussion can be applied for p-type semiconductor surfaces. A band bends downward at the depletion layer. Carrier holes are accumulated at the upward bent VBM in the accumulation layer of the semiconductor surface.

When one focuses on the discussion on the SCL of an n-type wide-gap semiconductor ($E_{\mathrm{g}} > 3$ eV), even if the band is largely bent upward (~ 1 eV), there still remains a wide energy difference between the Fermi level and the VBM (~ 2 eV) which is much larger than the thermal excitation energy of electrons ($E_{\mathrm{F}} \sim 25$ meV at room temperature). Therefore, a hole density is much smaller than the electron carrier density and the hole density can be neglected [$p(z) = 0$]. The band bending structure of an n-type wide-gap semiconductor can be obtained by solving the simplified Poisson equation at the surface:

$$\frac{d^2V(z)}{dz^2} = -\frac{e^2}{\epsilon(z)\epsilon_0}\{N_{\mathrm{D}} - n(z)\}. \tag{2.4}$$

2.1.1 Effective mass approach and bulk Fermi level

For the purpose of obtaining the band bending structure of a semiconductor, the effective mass approach is a reasonable approximation. In the tight-binding model for a material with the cubic lattice symmetry, an electron energy dispersion can be written in the nearest neighbor approximation [25]:

$$E(k) = -2t_{\rm h}(\cos k_x a + \cos k_y a + \cos k_z a), \tag{2.5}$$

where $t_{\rm h}$ is the electron hopping integral, a is the lattice constant, and k_β ($\beta = x,\ y,\ z$) is the wave numbers along the β axes. In the long wavelength limit ($k_\beta a \sim 0$), Eq. (2.5) is approximated as $E(k) = 2t_{\rm h}a^2\boldsymbol{k}^2 \equiv \hbar^2\boldsymbol{k}^2/2m^*$, with $m^* = \hbar^2/2t_{\rm h}a^2$ being the effective mass. The same discussion can be applied for non-cubic structures with anisotropic effective mass approximations as discussed in Chapter 4. With the isotropic effective mass approximation, the bulk CBM position ($V_{\rm bulk}$) against the Fermi level is calculated using Eq. (2.3), where electron carrier density is obtained by

$$n = \int_{-\infty}^{\infty} dE\ g(E) f_{\rm FD}(E). \tag{2.6}$$

Here, $f_{\rm FD}(E)$ is the Fermi-Dirac distribution function:

$$f_{\rm FD}(E) = \frac{1}{1 + \exp\{(E - E_{\rm F})/(k_{\rm B}T)\}}, \tag{2.7}$$

and $g(E)$ is the density of states of the conduction-band electrons

$$g(E) = \frac{\sqrt{2m^{*3}(E - V_{\rm bulk})}}{\pi^2\hbar^3} \times \Theta(E - V_{\rm bulk}), \tag{2.8}$$

where Θ is the unit step function: $\Theta(x) = 1$ for $x \geq 0$ and 0 otherwise. $N_{\rm D}$ can be obtained by the Hall measurements. Once one obtains $N_{\rm D}$, the bulk CBM position is calculated using Eq. (2.3).

2.1.2 Depletion layer of an *n*-type semiconductor

The band structures of a depletion layer at the n-type wide gap semiconductor surface are calculated using Eq. (2.4). The electron carrier density n is obtained from Eq. (2.6), which is the function of the CBM position. Therefore, one needs to solve the Poisson equation self-consistently. The self-consistent calculation is conducted until one obtains

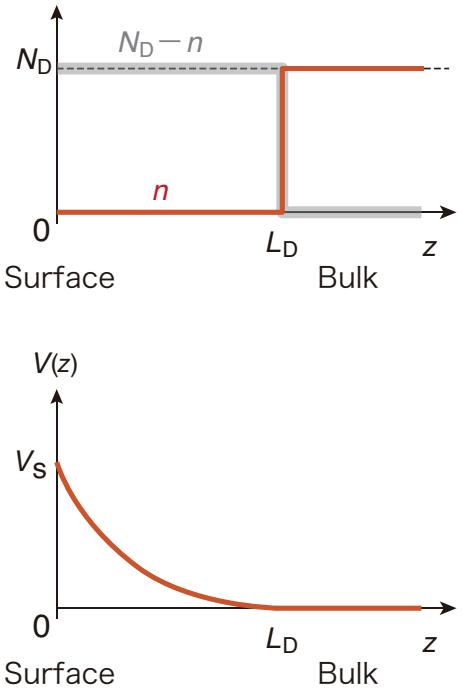

FIGURE 2.2: The electron carrier density and potential variation against the depth z.

a given surface potential $V_s = V(0)$ or a surface carrier density N_{ss}:

$$N_{ss} = \frac{\epsilon(0)\epsilon_0}{e^2}\left[\frac{dV(z)}{dz}\right]_{z=0}. \tag{2.9}$$

Although the band diagram is obtained by the self-consistent calculation, the depth of the depletion layer L_D is roughly estimated using a more simplified model. Within the model, thermionic excitations of the electrons are ignored and the electron carrier density takes $n = N_D$ at $z > L_D$ and $n = 0$ at $z < L_D$ (Fig. 2.2). By ignoring the variation of ϵ against z, one obtains

$$\frac{d^2V(z)}{dz^2} = -\frac{e^2N_D}{\epsilon\epsilon_0}, \tag{2.10}$$

at $z < L_D$. This differential equation is easily solved and $V(z) = e^2N_D/(2\epsilon\epsilon_0)\cdot(z-L)^2$ is obtained. By writing the surface potential as $V_s = V(0)$, L_D is given by

$$L_D = \sqrt{\frac{2\epsilon\epsilon_0 V_s}{e^2N_D}}. \tag{2.11}$$

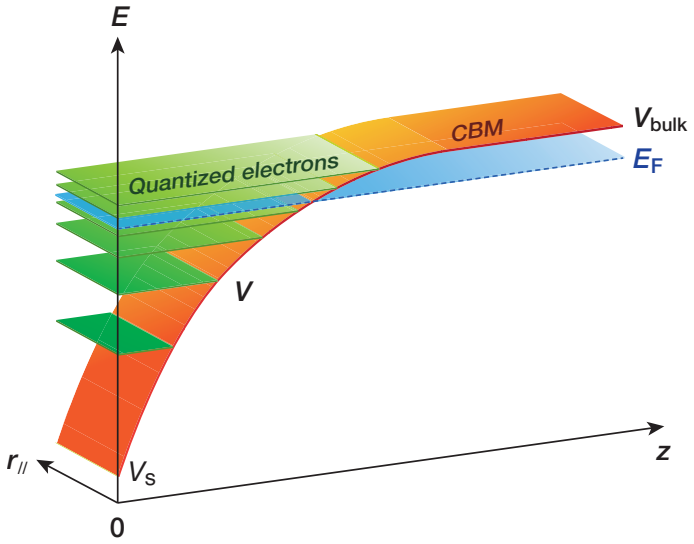

FIGURE 2.3: Schematic picture of the accumulation layer and the subband minima of the quantized electrons. The red curve shows the energy variation of the CBM position. The green plates indicate the subband minima of the quantized electrons.

2.1.3 Accumulation layer of an *n*-type semiconductor

In the depletion layer of an n-type semiconductor, the electric field is screened by ionized donors, the density of which N_{D}^{+} is lower than N_{D}. On the other hand, the electric field in an accumulation layer of an n-type semiconductor is screened by the electron carriers the density of which can be much higher than N_{D}. Therefore, the accumulation layer can be much thinner than the depletion layer.

In an accumulation layer, electrons are quantized due to the quantum confinement between the two potential barriers of the bulk band gap and the surface as depicted in Fig. 2.3. These quantized electrons construct a subband structure. The energies of subbands are obtained by solving the Schrödinger equation along the z axis:

$$\left\{-\frac{\hbar^2}{2m^*}\frac{\partial^2}{\partial z^2} + V(z)\right\}\phi_{k_{\parallel}j}(z) = E_j^0\phi_{k_{\parallel}j}(z), \tag{2.12}$$

where $\hbar$ is the reduced Planck constant, $\phi_{k_{\parallel}j}$ and E_j^0 are the wave function and the eigenenergy of a subband with quantum number j, respectively. The Schrödinger equation can be solved analytically only if the potential variation $V(z)$ is written in a simple equation. Therefore, self-consistent calculations are required. Further detailed solutions are described in Chapter 4.

2.2 Surface photovoltage and recombination process

This section describes the physical model of the surface photovoltage (SPV) effect and a relaxation process of photoexcited carriers. The SPV effect has been studied for many years for the use of solar cells and the optical switch. Recent studies have shown that the carrier lifetime of photoexcited carriers can be obtained by analyzing the relaxation process of the SPV effect [26]. Since carrier recombination time is one of the important factors of the photocatalytic effect, understanding of physical model of the SPV effect is of great importance.

2.2.1 Surface photovoltage effect

The surface potential of a depletion layer of an n-type semiconductor can be decreased by photon irradiation. This effect is called surface photovoltage effect. The physical model of SPV effect is illustrated in Fig. 2.4 and can be explained by the following processes [27, 28]. When a photon with the energy larger than the bulk band gap of a semiconductor is irradiated at the semiconductor surface, the photon excites an electron in the valence band to the conduction band, and an electron-hole (e-h) pair is created [Fig. 2.4(a)]. The photoexcited electron and hole transfer to the bulk side and surface side, respectively, by the potential gradient of the band bending [Fig. 2.4(a)]. The electric field induced by these transferred electrons and holes works to cancel the electric field induced by the surface acceptors. As a result, the band bending shifts to the lower energy side and becomes flatter [Fig. 2.4(b)].

The photoexcited electrons and holes recombine at recombination centers and the band bends back toward higher energy side. The timescale for the photoexcitation is below femtosecond. The time scale of carrier transfer is from femtosecond to picosecond. The time scale of the relaxation process widely spread from the order of picosecond to larger than milisecond depending on the semiconductors and their surface treatments [26, 29–31]. The two-photon adsorption process or the existence of impurity states in the band gap enables the photoexcitation of electrons even if the photon energy is smaller than the bulk band gap of the semiconductor.

In contrast to the SPV effect in the depletion layer, photoexcited electrons and holes are transfered to the surface side and the bulk side, respectively, at an accumulation layer. As a result, the band bending is shifted to the higher energy side [26].

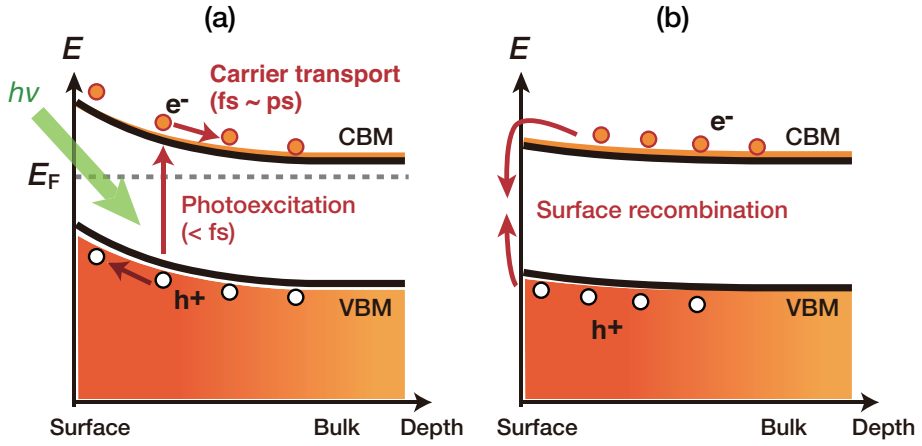

FIGURE 2.4: Qualitative explanation of the SPV effect [27, 28]. The photoexcitation process by the laser irradiation and carrier transfer driven by the potential gradient (a) and the thermionic recombination process (b) are illustrated.

2.2.2 Recombination process

A transition probability from a state to another state decreases with the energy difference between the states. Therefore, the recombination process of photoexcited e-h pairs is due to the transitions mainly though the surface states, impurity states located near the surface, or adsorbed ions.

The recombination process of SPV effect can be explained mainly by thermionic process [29, 32]. In the thermionic relaxation process at the depletion layer of an n-type semiconductor surface, electron carriers thermally overcome the potential barrier and recombine with the holes trapped at the surface (see Fig. 2.4).

The equation of the thermionic relaxation time is obtained as following steps [27, 32]: The decay rate of trapped holes can be expressed by the hole density which is trapped at the surface p_{s}, the thermal velocity of an electron carrier υ_{th}, and the thermal cross section of capturing an electron σ_{th}:

$$\frac{dp_{\mathrm{s}}(t)}{dt} = -\sigma_{\mathrm{th}}\upsilon_{\mathrm{th}}n_{\mathrm{t}}p_{\mathrm{s}}(t) \tag{2.13a}$$

$$= -\frac{p_{\mathrm{s}}(t)}{\tau_{\mathrm{th}}}, \tag{2.13b}$$

where n_{t} is the electron density expressed as $n_{\mathrm{t}} = N_{\mathrm{c}}\exp(-V_{\mathrm{s}}^{*}/kT)$. Here, N_{c} is the density of states of the bulk conduction band and V_{s}^{*} is the surface potential during

the relaxation process. From Eq. (2.13a) to Eq. (2.13b), the equation

$$\frac{1}{\tau_{\mathrm{th}}} = -\sigma_{\mathrm{th}} \upsilon_{\mathrm{th}} N_{\mathrm{c}} \exp\left(-\frac{V_{\mathrm{s}}^*}{k_{\mathrm{B}} T}\right) \tag{2.14}$$

is used [27, 28]. By writing $p_{\mathrm{s}}(0) = p_{0\mathrm{s}}$ and with Eq. (2.13b), one obtains

$$p_{\mathrm{s}}(t) = p_{0\mathrm{s}} \exp\left(-\frac{t}{\tau_{\mathrm{th}}}\right). \tag{2.15}$$

If one denotes the surface potential before the photoexcitation by V_{s} and V_{s}^* as the potential during the relaxation, the surface photovoltage shift V_{SPV} can given by as $V_{\mathrm{SPV}} = V_{\mathrm{s}} - V_{\mathrm{s}}^*$. By introducing an ideality factor η which can be understood from diode theory [33], Eq. (2.14) can be rewritten as

$$\frac{1}{\tau_{\mathrm{th}}} = \sigma_{\mathrm{th}} \upsilon_{\mathrm{th}} N_{\mathrm{c}} \exp\left(-\frac{V_{\mathrm{s}} - V_{\mathrm{SPV}}}{\eta k_{\mathrm{B}} T}\right) \tag{2.16a}$$

$$= \frac{1}{\tau_{\mathrm{s}}} \exp\left(\frac{V_{\mathrm{SPV}}}{\eta k_{\mathrm{B}} T}\right), \tag{2.16b}$$

where τ_{s} is defined by

$$\tau_{\mathrm{s}} = \frac{1}{\sigma_{\mathrm{th}} \upsilon_{\mathrm{th}} N_{\mathrm{c}}} \exp\left(\frac{V_{\mathrm{s}}}{\eta k_{\mathrm{B}} T}\right). \tag{2.17}$$

Surface photovoltage shift V_{SPV} is given by the fractional charge density $\Delta_n = \Delta n / n_0$, where n_0 is the electron density before the photoexcitation [27, 28]:

$$V_{\mathrm{SPV}} = \eta k_{\mathrm{B}} T \ln(1 + \Delta_n). \tag{2.18}$$

The above equations give the differential equation of V_{SPV} as

$$\frac{dV_{\mathrm{SPV}}}{dt} = -\frac{\eta k_{\mathrm{B}} T}{\tau_{\mathrm{s}}} (e^{\frac{V_{\mathrm{SPV}}}{\eta k_{\mathrm{B}} T}} - 1). \tag{2.19}$$

The solution of this equation gives the temporal variation of the SPV shift:

$$V_{\mathrm{SPV}}(t) = -\eta k_{\mathrm{B}} T \ln\left[1 - \left\{1 - \exp\left(-\frac{V_{\mathrm{SPV}}(0)}{\eta k_{\mathrm{B}} T}\right)\right\} \mathrm{e}^{-t/\tau_{\mathrm{s}}}\right]. \tag{2.20}$$

The fast relaxation of the SPV shift can be explained by a tunneling model [29, 32]. In the tunneling model, the electron carriers in the CBM tunnel though the potential barrier at the surface and combine with holes in the surface states. The tunneling probability is given by a function of the mean width of a SCL and the Bohr-type

radius of electronic states at the surface. Since the depletion layer of a low-doped semiconductor is thick [> 10 nm, see Eq. (2.11)] and the tunneling probability is very small, tunneling model is usually neglected at low-doped semiconductor surfaces.

Chapter 3

Experimental methods

In this thesis, we have obtained the electronic structures of semiconductor surfaces by angle-resolved photoelectron spectroscopy (ARPES) measurements. The temporal variation of the surface photovoltage (SPV) effects has been obtained by time-resolved photoelectron spectroscopy (trPES) system, where SPV shifts are induced by femtosecond laser pulses and photoelectrons excited by a synchrotron radiation (SR) light are proved by a time-of-flight type electron analyzer. A four-point probes (4PP) electrical conductivity method was applied to monitor the surface conductivity changes of a semiconductor surface during the hydrogen adsorption procedures. In this chapter, the experimental systems to describe the measurement systems are introduced.

3.1 Photoelectron spectroscopy

Photoelectron spectroscopy (PES) is a powerful technique with which one can directly obtain the electronic structure of a solid in a momentum space. In this section, an intuitive view of photoemission process and equations which describe the angle-resolved photoemission processes are introduced.

3.1.1 An intuitive view of photoemission process

The theory of the photoemission process is explained with the photoelectric effect developed by Einstein in 1905 [34]. The schematic image of the photoemission process is depicted in Fig. 3.1. When a photon with the energy $h\nu$ is irradiated to an atom, an electron in the atom is excited. If the photoexcited electron has the energy larger

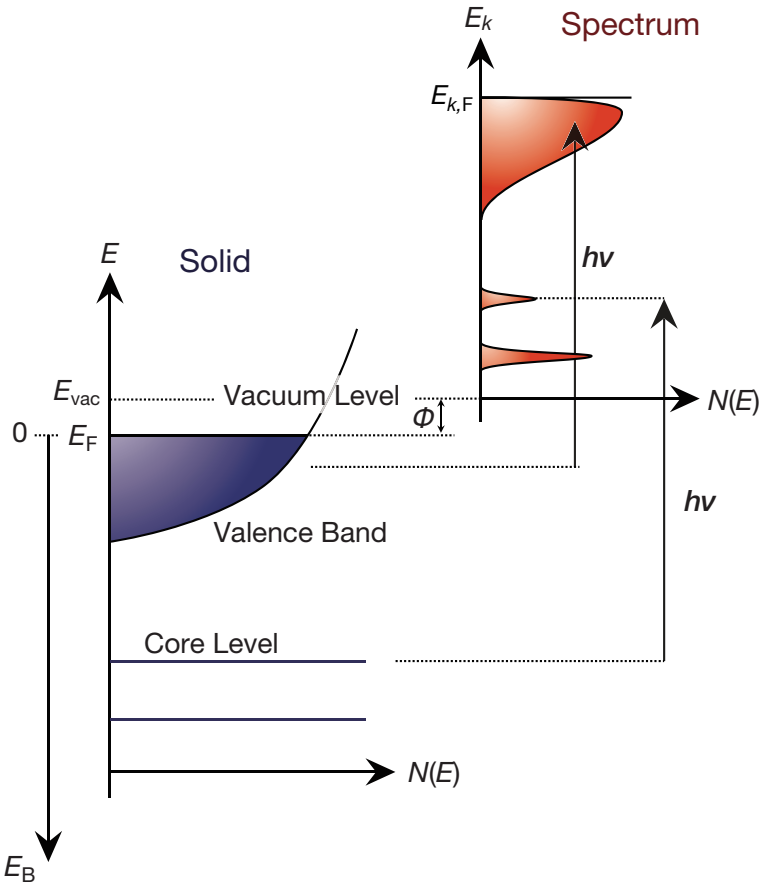

FIGURE 3.1: Schematic drawing of the photoemission process [35]. The electron density of states $N(E)$ in the solid (left) and in the vacuum (right) are shown.

than the vacuum level, the excited electron can go out of the atom to the vacuum as a photoelectron. In the photoexcitation process, the energy conservation law requires

$$E_k = h\nu - E_{\mathrm{B}}, \tag{3.1}$$

where E_k is the kinetic energy of photoelectron and E_{B} is the binding energy of the electron. If photoelectrons are escaped from a solid, they lose energy called work function Φ which is defined by the energy difference between the vacuum level E_{vac} and the Fermi level E_{F} in the bulk and varies from 3 to 6 eV depending on the solid and the orientation of the crystal [35]. The energy conservation law is rewritten as

$$E_k = h\nu - E_{\mathrm{B}} - \Phi. \tag{3.2}$$

Once one measures E_k by a photoelectron analyzer, E_B in a solid can be obtained with the evaluated values of $h\nu$ and Φ using Eq. (3.2). In a usual PES system, synchrotron radiation (SR), a high-harmonic generation (HHG) laser, a gas-discharge lamp, or an X-ray tube are used as light sources. The photoelectrons with a certain energy are collected by a photoelectron analyzer and the number of photoelectrons are counted. By sweeping the energy window of the photoelectron analyzer, one can obtain a spectrum $N(E)$ in a solid as depicted in Fig. 3.1. $E_{k,\mathrm{F}}$ in the figure is given by $E_{k,\mathrm{F}} = h\nu - \Phi$ and denotes the kinetic energy of a photoelectron emitted from the Fermi edge in the vacuum.

The most succeeded model for the photoemission process called the three step model is developed by Berglund and Spicer [36]. Figure 3.2 shows schematic image of the three step model. In the model, first, an electron in the valence band is excited by a photon. In this step, the energies of photoexcited electrons distribute within the same energy width of the valence band electrons ΔE_VB. In this transition, the wave vectors of the initial state $\boldsymbol{k}_\mathrm{i}$ and of the final state $\boldsymbol{k}_\mathrm{f}$ follow the conservation law $\boldsymbol{k}_\mathrm{f} = \boldsymbol{k}_\mathrm{i} + \boldsymbol{G}$, where $\boldsymbol{G}$ is the reciprocal lattice vector (see Fig. 3.3). Here, the momentum of an incident photon ($= h\nu/c$, c is the speed of light) is neglected[1]. In the second process, the photoexcited electrons transport to the surface. In this transportation process, some photoexcited electrons lose their energies by the inelastic scattering with ions in the solid and generate the secondary electrons. In the third process, electrons penetrate though the surface. An electron with higher energy than E_vac (or Φ from the Fermi level) can escape from the solid and be a photoelectron.

In the first step, the transition probability w_if of the electron from the initial state ϕ_i with the energy E_i to the final state ϕ_f with the energy E_f follows the Fermi Golden Rule:

$$w_\mathrm{if} = \frac{2\pi}{\hbar} |\langle \phi_\mathrm{f} | \Delta | \phi_\mathrm{i} \rangle|^2 \, \delta(E_\mathrm{f} - E_\mathrm{i} - h\nu), \tag{3.3a}$$

$$\Delta = \frac{e}{2m_e c}(\boldsymbol{A}\cdot\boldsymbol{p} + \boldsymbol{p}\cdot\boldsymbol{A}) - e\phi + \frac{e^2}{2m_e c^2}|\boldsymbol{A}|^2 \approx \frac{e}{m_e c}\boldsymbol{A}\cdot\boldsymbol{p}, \tag{3.3b}$$

where $\boldsymbol{A}$ is the vector potential, ϕ is the scalar potential, and $\boldsymbol{p}$ is the momentum operator. Here, one can take the gauge $\phi = 0$ and the two photon emission term can be neglected $|\boldsymbol{A}|^2 \approx 0$. The commutation law gives $\boldsymbol{A}\cdot\boldsymbol{p} + \boldsymbol{p}\cdot\boldsymbol{A} = 2\boldsymbol{A}\cdot\boldsymbol{p} + i\hbar(\boldsymbol{\Delta}\cdot\boldsymbol{A})$. The second term of the equation $[i\hbar(\boldsymbol{\Delta}\cdot\boldsymbol{A})]$ is called a surface photoemission term, and can be large at a surface where dielectric constants change a lot between the surface and

[1] The wave vector shift of a photoexcited electron by a 100 eV photon is about 0.5 nm^{-1}.

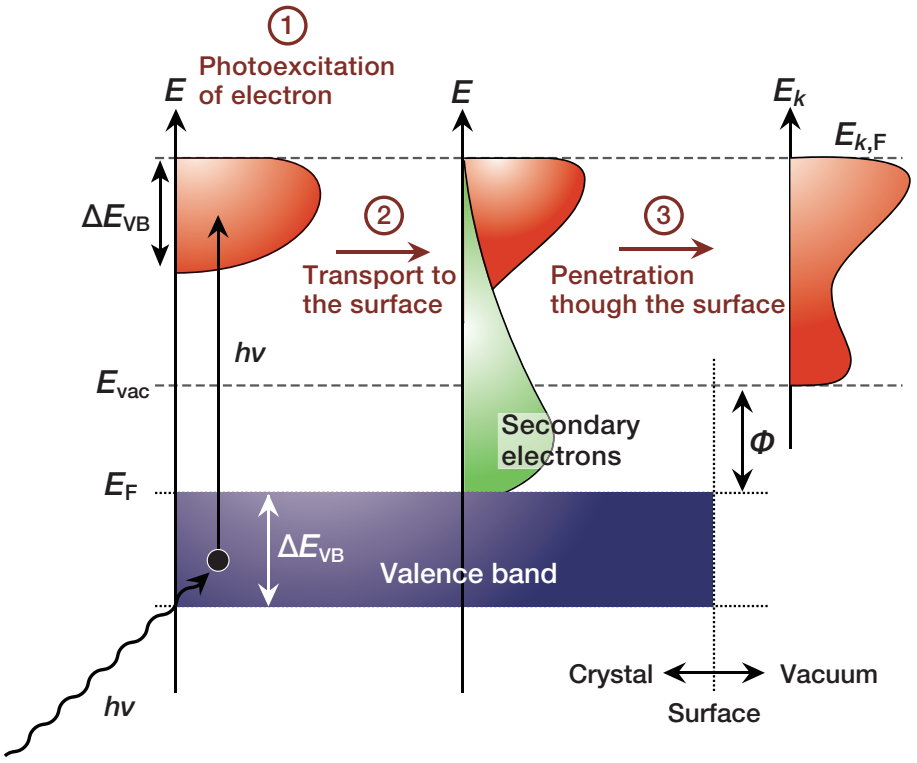

FIGURE 3.2: Schematic diagram of the three step model of the PES process [35]. Processes of (1) photoexcitation of an electron, (2) transport of the photoexcited electrons to the surface, and (3) penetration though the surface are depicted. The horizontal axes denote the electron densities of states in the crystal and vacuum.

the vacuum [37, 38]. However the surface photoemission term is frequently neglected because of the symmetry of $\boldsymbol{A}$ in a crystal. By neglecting the surface photoemission term, Eq. (3.3b) can be rewritten as

$$\Delta \approx \frac{e}{m_e c}\boldsymbol{A}\cdot\boldsymbol{p}, \tag{3.4a}$$

$$w_{\mathrm{if}} \approx \frac{2\pi e^2}{m_e^2 c^2 \hbar}\left|\langle\phi_{\mathrm{f}}\left|\boldsymbol{A}\cdot\boldsymbol{p}\right|\phi_{\mathrm{i}}\rangle\right|^2 \delta(E_{\mathrm{f}} - E_{\mathrm{i}} - h\nu). \tag{3.4b}$$

In the free-electron final-state model, the final state is approximated by the free-electron state with the energy

$$E_{\mathrm{f}} = \frac{\hbar^2 k_{\mathrm{f}}^2}{2m_e} + E_0, \tag{3.5}$$

where E_0 is the energy minimum of the free-electron final-state and takes the value of the theoretical muffin-tin zero [35]. The inner potential V_0 is defined by $V_0 = E_{\mathrm{vac}} - E_0$ as shown in Fig. 3.3.

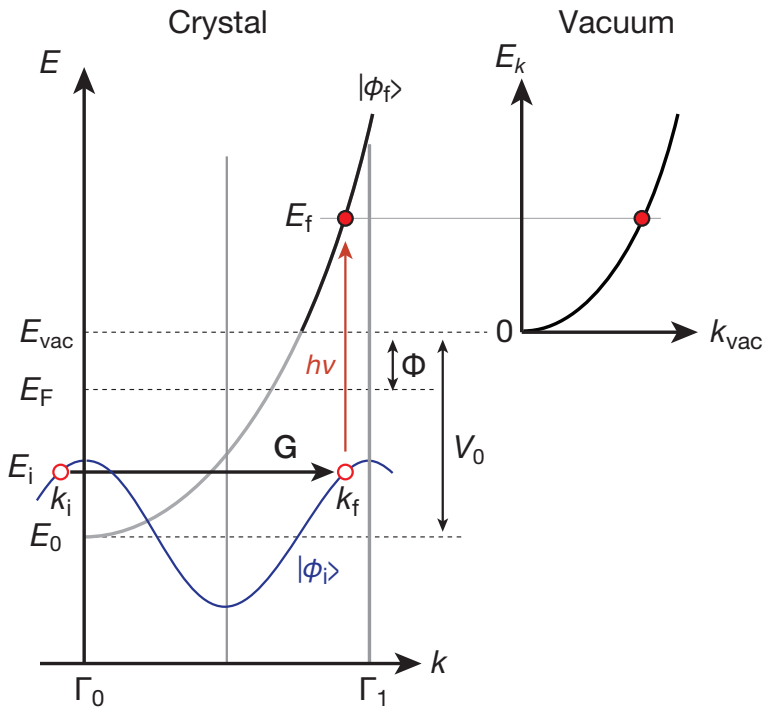

FIGURE 3.3: Schematics of the free-electron final-state model in the PES process [35]. An electron in the initial state $|\phi_i\rangle$ is excited with a photon with $h\nu$ to the free-electron final-state $|\phi_f\rangle$.

Some of the photoexcited electrons are scattered in the second step. Since the electron-phonon scattering probabilities are large only at very low energies ($<$ 100 meV), electron-electron scattering process plays an important role in the transportation process. The mean-free paths (, or mean-escape depths) against the kinetic energies of photoelectrons are shown in Fig. 3.4. As can be seen from the figure, the mean-free paths against the kinetic energies are independent of elements, and therefore, the curve on the graph is called a universal curve. The mean-free path takes the minimum value of ~ 0.6 nm at $E_k \sim 50$ eV and is shorter than 2 nm in a wide energy range from 5 to 2000 eV. Therefore, PES is understood as a surface sensitive experimental method.

In the final step, a photoexcited electron which has a momentum large enough to overcome the surface potential barrier can escape from the surface. This condition is written as

$$\frac{\hbar^2}{2m_e}k_{s\perp}^2 \geq \frac{\hbar^2}{2m_e}k_{s\perp}^{c2} = E_{vac} - E_0 \equiv V_0, \tag{3.6}$$

where $k_{s\perp}$ is the surface normal component of the wave vector of the photoexcited electron in the solid k_s. $k_{s\perp}^c$ is the surface normal component of the critical wave number in the solid (see Fig. 3.5).

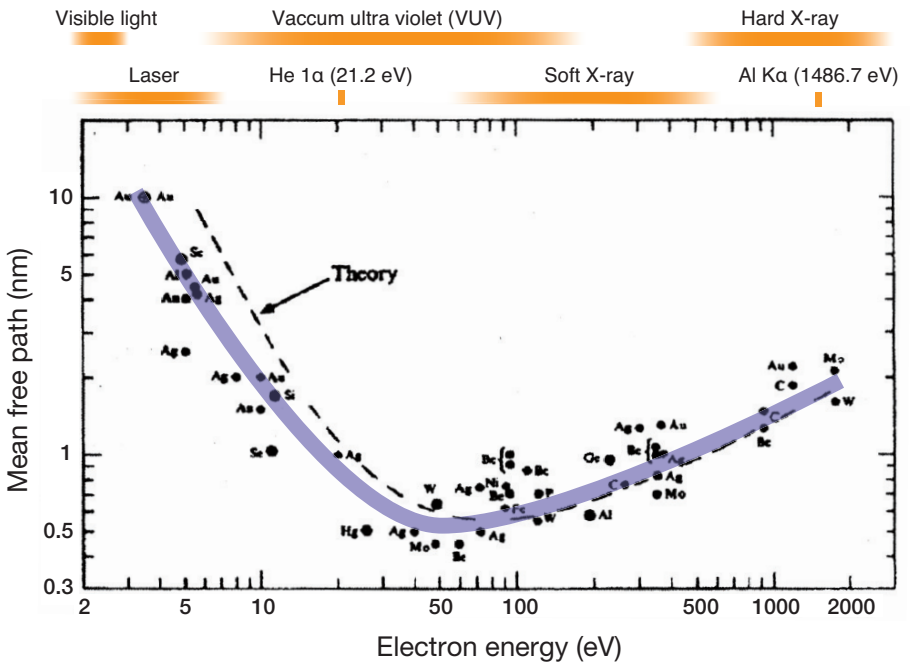

FIGURE 3.4: Universal curve of electrons in solids [39]. The dashed curve shows the theoretically obtained universal curve independent of elements. The purple thick curve is a guide to the eye. Characteristic energy scales of the light sources are indicated above the graph.

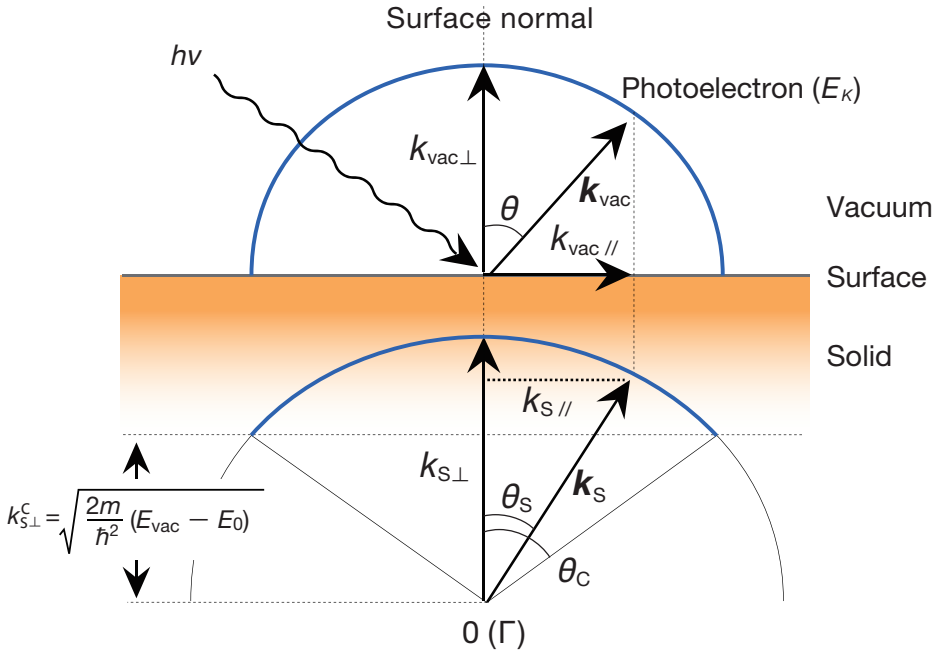

FIGURE 3.5: Schematic diagram of the wave vectors of photoexcited electrons in a solid and vacuum [39]. Blue solid curves show the internal and external escape cones of the photoexcited electrons having momentums on a circle with radii of k_{vac} in the vacuum and $k_{s\perp}$ at the surface.

The kinetic energy of an excited electron in the solid E_s and that of an electron in the vacuum E_k are given by

$$E_\mathrm{s} = \frac{\hbar}{2m_e}|\boldsymbol{k}_\mathrm{f}|^2 = E_\mathrm{f} + (E_\mathrm{F} - E_0) \tag{3.7a}$$

$$E_k = E_\mathrm{f} - E_\mathrm{vac}. \tag{3.7b}$$

Here, the kinetic energies are defined with $E_\mathrm{F} = 0$. When a photoexcited electron in the solid transports to the surface in a critical angle $\theta_\mathrm{s} < \theta_\mathrm{c}$ (Fig. 3.8), the electron can escape from the surface into the vacuum. The equation of the critical angle can be obtained from Eq. 3.6 as

$$\cos\theta_\mathrm{c} = \frac{k^\mathrm{c}_{\mathrm{s}\perp}}{|\boldsymbol{k}_\mathrm{vac}|} = \frac{\sqrt{\frac{2m_eV_0}{\hbar^2}}}{\sqrt{\frac{2m_e(E_\mathrm{f}-E_0)}{\hbar^2}}} = \sqrt{\frac{V_0}{E_\mathrm{f}-E_0}}. \tag{3.8}$$

As described in Fig. 3.5, the surface parallel component of the wave vectors in the solid $k_{\mathrm{s}\parallel}$ and that in vacuum $k_{\mathrm{vac}\parallel}$ are conserved. Therefore, one can obtain $k_{\mathrm{vac}\parallel}$ by detecting the kinetic energy E_k and the emission angle θ from the equation:

$$k_{\mathrm{vac}\parallel} = k_{\mathrm{s}\parallel} = \frac{\sqrt{2m_eE_k}}{\hbar}\sin\theta. \tag{3.9}$$

This equation is expressed as $k_{\mathrm{vac}\parallel}[\mathrm{nm}^{-1}] = 5.12\sqrt{E_k[\mathrm{eV}]}\sin\theta$ in units of nm^{-1} for $k_{\mathrm{vac}\parallel}$ and electron volt (eV) for E_k. By measuring the energy distributions of photoelectrons in every detection angle, E-k band dispersions are obtained. The wavenumber perpendicular to the surface between the surface $k_{\mathrm{f}\perp}$ and vacuum $k_{\mathrm{vac}\perp}$ is not conserved, and $k_{\mathrm{vac}\perp}$ can be obtained by

$$k_{\mathrm{vac}\perp} = \frac{\sqrt{2m_eE_k}}{\hbar}\sqrt{E_k\cos^2\theta + V_0}. \tag{3.10}$$

The inner potential V_0 of a crystal is experimentally obtained by plotting PES intensities with various photon energies and comparing the intensity-$k_{\mathrm{vac}\perp}$ spectrum with the theoretically-obtained band dispersions of the crystal. The inner potential varies from 10 to 20 eV depending on the crystal.

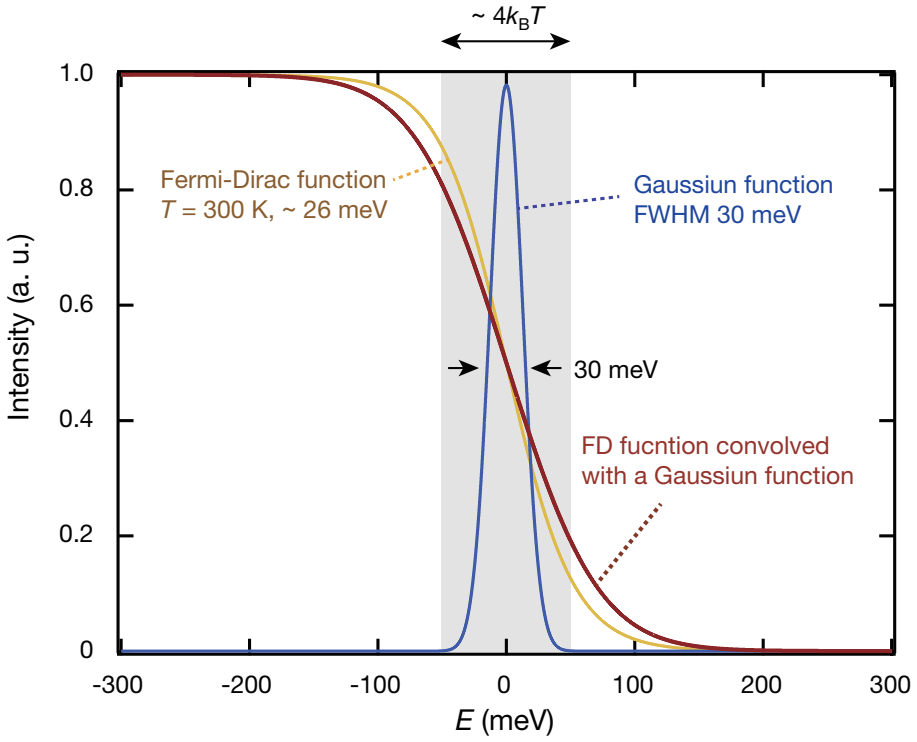

FIGURE 3.6: Fermi-edge fitting curves. The Fermi-Dirac function at $T = 300$ K ($k_{\mathrm{B}}T \sim 26$ meV), the Gaussian function with the full width at half maximum (FWHM) of 30 meV, and the Fermi-Dirac function convolved with a Gaussian function are shown by orange, blue, and red curves, respectively. The shaded area shows the energy window of width $\sim 4k_{\mathrm{B}}T$.

3.1.2 Fermi level

$k_{\mathrm{s}\parallel}$ can be obtained from E_k using Eq. (3.9). Because the absolute values of E_k are hardly obtained by the electron analyzer, the well-known parameters of $h\nu$ and Φ obtained by a PES spectrum are used to calculate E_k using the equation:

$$E_k = h\nu - \Phi - E_{\mathrm{B}} = h\nu - \Phi + E_k^{\mathrm{A}} - E_{k,\mathrm{F}}^{\mathrm{A}}. \tag{3.11}$$

Here, the kinetic energy of a photoelectron detected at the electron analyzer (E_k^{A}) is given by $E_k^{\mathrm{A}} = h\nu - E_{\mathrm{B}} - \Phi_{\mathrm{A}}$, where Φ_{A} is the work function of the photoelectron analyzer, and the kinetic energy of a photoelectron emitted from the Fermi edge at the electron analyzer ($E_{k,\mathrm{F}}^{\mathrm{A}}$) is given by $E_{k,\mathrm{F}}^{\mathrm{A}} = h\nu - \Phi_{\mathrm{A}}$.

$E_{k,\mathrm{F}}^{\mathrm{A}}$ is obtained by fitting a photoelectron spectrum with the Fermi-Dirac (FD) function. The FD function at $T = 300$ K ($k_{\mathrm{B}}T \sim 26$ meV) is shown in Fig. 3.6. The energy broadening of the incident photons and the limited resolution of the electron

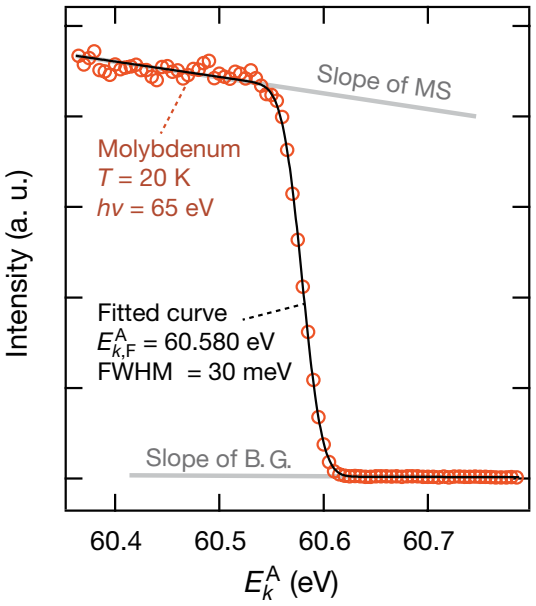

FIGURE 3.7: Photoelectron spectrum of Mo taken at $T = 20$ K with $h\nu = 65$ eV (orange circles). The black solid curve is the fitted curve. The gray lines indicate the slope of the density of states and the back ground intensities.

analyzer should be considered in addition to the energy broadening of the FD function. The Gaussian function with full-width at half-maximum (FWHM) of 30 meV and the FD function convolved by the Gaussian function are shown in Fig. 3.6. Figure 3.7 shows a PES spectrum taken on a Mo at $T = 20$ K and $h\nu = 65$ eV. The fitting curve is also shown in the figure as a black solid curve. The slope of the metallic state (MS) and back ground (B.G.) intensities are approximated by linear functions. $E^{\mathrm{A}}_{k,\mathrm{F}}$ was obtained by fitting the PES spectra with a linear function multiplied by the FD function and convolved with a Gaussian function.

3.1.3 Spectral function and incoherent process

The spectral function of the photoelectron with wavenumber $\boldsymbol{k}$ and energy ω can be expressed by an imaginary part of the one-particle Green function: $G^{-}(\boldsymbol{k}, \omega)$ [1]:

$$A^{-}(\boldsymbol{k}, \omega) = \frac{1}{\pi}\mathrm{Im}\{\mathrm{G}^{-}(\mathrm{k}, \omega)\}. \tag{3.12}$$

For the non-interacting case, the spectral function becomes:

$$A_0(\boldsymbol{k}, \omega) = \delta(\epsilon_k - \omega), \tag{3.13}$$

where ϵ_k is the energy of the initial state. For an intercting Fermi liquid, one obtains the following expression for the spectral function [1, 40]:

$$A(\boldsymbol{k},\omega) = \frac{1}{\pi}\mathrm{Im}\{\mathrm{G}^{-}(\mathrm{k},\omega)\}\frac{1}{|\omega - \epsilon_{\mathrm{k}} - \mathrm{Re}\Sigma(\mathrm{k},\omega)|^2 + |\mathrm{Im}\Sigma(\mathrm{k},\omega)|^2}, \tag{3.14}$$

where $\Sigma(\boldsymbol{k},\omega)$ denotes the self-energy of an electron. By defining the renormalization factor Z_k as $Z_k = (1 - \partial\mathrm{Re}\Sigma/\partial\omega)^{-1}$ and the lifetime of a quasi-particle excitation τ_k as $\tau_k = (Z_k\mathrm{Im}\Sigma)^{-1}$, one can decompose the spectral function in two parts [1, 40]

$$A(\boldsymbol{k},\omega) = Z_k\frac{\tau_k}{(\omega - \epsilon_k)^2 + (\frac{1}{\tau_k})^2} + A^{\mathrm{inc}}(\boldsymbol{k},\omega), \tag{3.15}$$

where $A^{\mathrm{inc}}(\boldsymbol{k},\omega)$ is the incoherent part of the spectral function.

3.1.4 Photoelectron spectrometer

All ARPES spectra shown in this thesis were obtained with a hemispherical electron analyzer. The a time-resolved PES results were obtained with a time-of-flight (TOF) electron spectrometer. With the hemispherical analyzer, kinetic energies of photoexcited electrons are determined by an electric field applied between two hemispheres. With the TOF electron spectrometer, the kinetic energies are determined by monitoring the flight time of the photoelectrons from the sample surface to the electron detector.

3.1.5 Hemispherical analyzer

Figure 3.8 shows the schematic drawing of a hemispherical analyzer system. Photoexcited electrons are collected by an electron lens. Photoelectrons passing though the entrance slit are deflected and focused on to the entrance slit of the analyzer by the electric field applied between the two hemispheres. The higher voltage of V_{in} is applied to the inner hemisphere than the voltage applied to the outer sphere V_{out}. The deflected photoelectrons with the pass energy E_{pass} of

$$E_{\mathrm{pass}} = \frac{e(V_{\mathrm{in}} - V_{\mathrm{out}})}{\frac{R_2}{R_1} - \frac{R_1}{R_2}} \tag{3.16}$$

are able to pass between the two hemispheres. Electron with energies larger than E_{pass} deviate toward the outer side of the exit slit, and those with energies smaller than E_{pass}

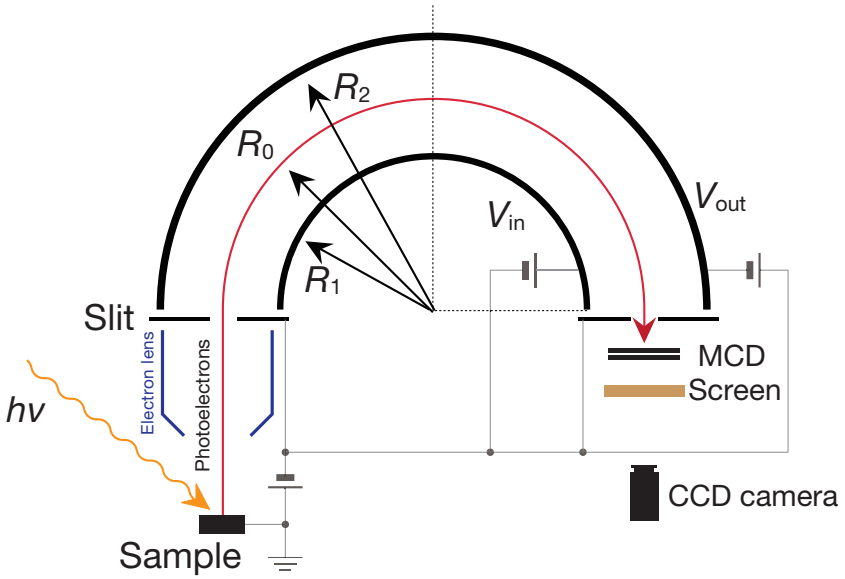

FIGURE 3.8: Schematic drawing of the hemispherical analyzer system [41]. The radius of the inner and outer hemispheres are R_1 and R_2, respectively, and the mean radius is R_0. The red curve illustrates the trajectory of a photoelectron.

deviate toward the inner side of the slit. The energy resolution ΔE of the system is given using the slit width w by

$$\frac{\Delta E}{E_{\text{pass}}} = \frac{w}{2R_0} + \frac{\alpha^2}{4}, \tag{3.17}$$

where α is a value of angular spread which is determined by the lens in front of the entrance slit. In order to resolve energies of photoelectrons with large E_k with high-resolution, modern analyzer systems fix the applied voltages of the hemispheres and decelerate photoelectrons by retarding potential V_{R} applied in the electron lens located in front of the entrance slit (see Fig. 3.8). The Fermi level of the electron analyzer (E_{F}^{A}) is given by $E_{\text{F}}^{\text{A}} = E_{\text{F}} + eV_{\text{R}}$. As shown in Fig. 3.9, the energy is conserved as $E_k + \Phi = h\nu - E_{\text{B}} = E_{\text{pass}} + \Phi_{\text{A}} + eV_{\text{R}}$. It should be noted that the work function of the sample is not directly detected by the analyzer.

Electrons passing through the exit slit are amplified using multi-channel plates (MCPs) and hit a phosphor screen. Bright spots at the screen are monitored by a CCD camera connected to a PC. One dimension of the 2D screen is used to resolve the kinetic energy of the photoelectron energies and the other dimension is used to resolve emission angles. Modern hemispherical analyzers can detect photoelectrons with a wide emission angles of $\pm 30°$ [41].

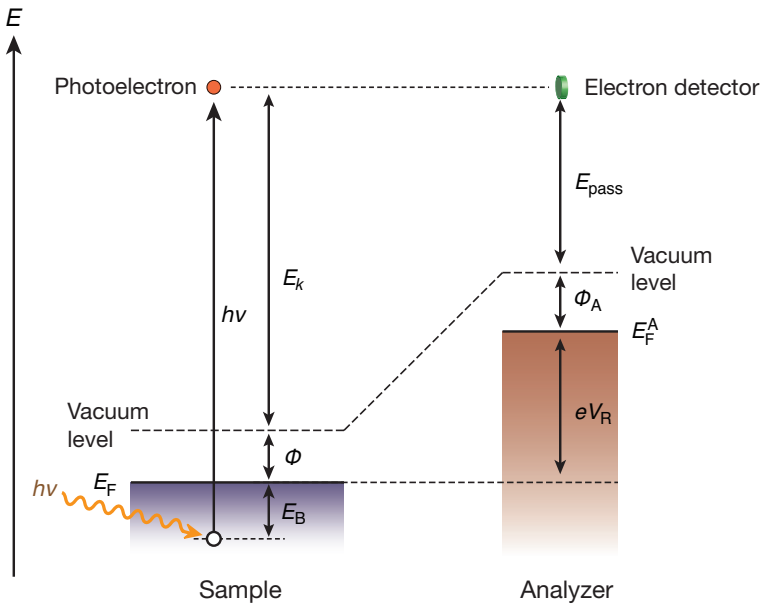

FIGURE 3.9: Schematic representation of the photoexcitation and the electron detection system.

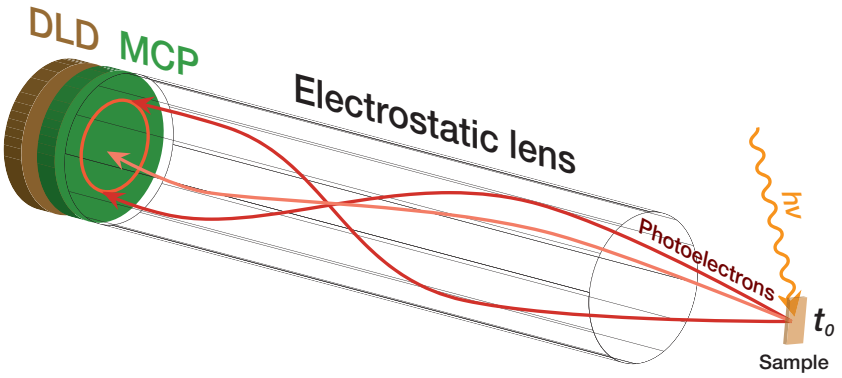

FIGURE 3.10: Schematic drawing of the time of flight analyzer system. Red curves represent the trajectories of photoelectrons bent by the electrostatic lens.

3.1.6 Time-of-flight analyzer

The schematic drawing of the time-of-flight (TOF) analyzer system is shown in Fig. 3.10. Photoelectrons emitted from a sample travel through the cylindrical analyzer and are decelerated by the electrostatic lens. The number of electrons are amplified by the two Multi-channel plates (MCP) and the multiplied electrons are changed to electric signals at the Delay Line Detector (DLD) [42]. If external electric or magnetic fields

are neglected, a kinetic energy of a photoelectron E_k is obtained by [43]

$$E_k = \frac{m_e}{2}\left(\frac{d_{\mathrm{drift}}}{t_{\mathrm{TOF}}}\right)^2, \tag{3.18}$$

where d_{drift} is the drift length and t_{TOF} is the time of flight of the photoelectron. The equation of the energy resolution ΔE_k of the system is obtained from Eq. (3.20) as

$$\Delta E_k = \sqrt{\frac{8E_k^3}{m_e}}\frac{\Delta t_{\mathrm{TOF}}}{d_{\mathrm{drift}}}, \tag{3.19}$$

where Δt_{TOF} is the time resolution of t_{TOF}. Therefore, a TOF analyzer with a longer cylinder have higher energy resolution. The ARTOF 10k analyzer uses electric lens to earn long drift length. The time of flight (t_{TOF}), detecting position in x and y coordinates, and the photoelectron counts are measured by the DLD. The matrix of the (t_{TOF}, x, y) is converted to (E_k, θ, ϕ) by a transformation matrix which depends on parameters of the electron lens. One of the advantages of the angle-resolved time-of-flight (ARTOF) analyzer (ARTOF 10k analyzer, VG-Scienta) is that one can obtain a band dispersion map along the k_x and k_y directions without rotating the sample. Up to 250 times larger transmission efficiency of photoelectrons can be acquired with the ARTOF than with the hemispherical analyzer because of the slit less structure [44]. The main disadvantage of the TOF electron spectrometer is that the light source is limited to the pulsed light and constant wave (CW) lamps or CW lasers can not be used.

3.1.7 Time-resolved photoelectron spectroscopy

In this thesis, time-resolved photoelectron spectroscopy (trPES) measurements have been conducted at the soft X-ray beamline BL07LSU of SPring-8 [45–47]. A femto-second pulse laser is used as a pumping light and photoelectrons excited by SR are detected with a TOF electron spectrometer. Timing tree of the time-resolved photoelectron spectroscopy system is shown in Fig. 3.11. Sine signal of the master oscillator, which is synchronized with the SR, is transmitted to two delay generators. The sine signals and digital signals from the delay generator are sent to the pulse-laser system, and a trigger signal is sent to a time-to-digital (TDC) converter mounted on a computer. Therefore, the SR pulsed light and the pulsed laser are synchronized.

The total time resolution of this system, where the femto-second pulsed laser is used for pumping and the SR with the pulse width of $\sim$ 50 ps is used as the probe pulse,

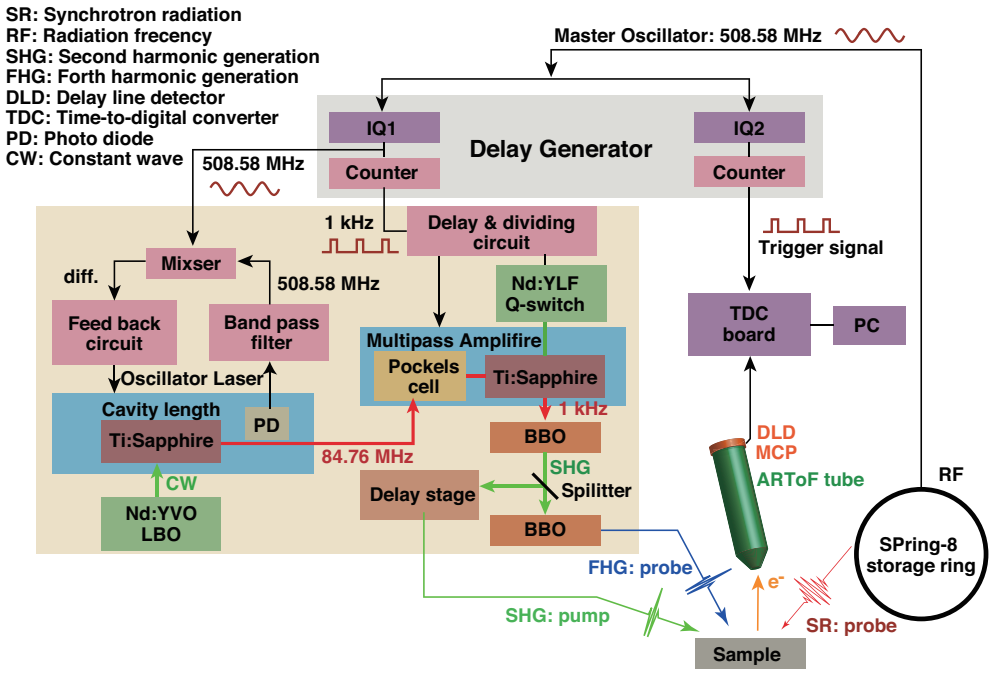

FIGURE 3.11: Timing tree of the time-resolved spectroscopy system [45]. Sine signal of the master oscillator with the frequency of 508.58 MHz is transmitted to two delay generators. One digital signal from the delay generator is used as a trigger signal. The sin and digital signals from another delay generator are transmitted to the laser system.

is about 50 ps. The time scales of the various physical and chemical phenomena are listed in Fig. 3.12 [46]. The time scale associated with electron-electron (*e-e*), electron-phonon (*e-ph*), electron-coherent phonon (*e-cph*) interaction are in the range from 10 fs to 10 ps, and shorter than SR pulse width. In order to observe these phenomena, a femto-second pump-probe system is required. Therefore, more slower phenomena such as surface redox reaction, phonon-phonon (*ph-ph*) coupling, and carrier transferring can be studied by the current time-resolved PES system. One of the advantages of the current laser-pump SR-probe system is that one can observe spectral changes of the valence band and core levels in *real time*, which give us information about chemical reactions and potential shifts at solid surfaces.

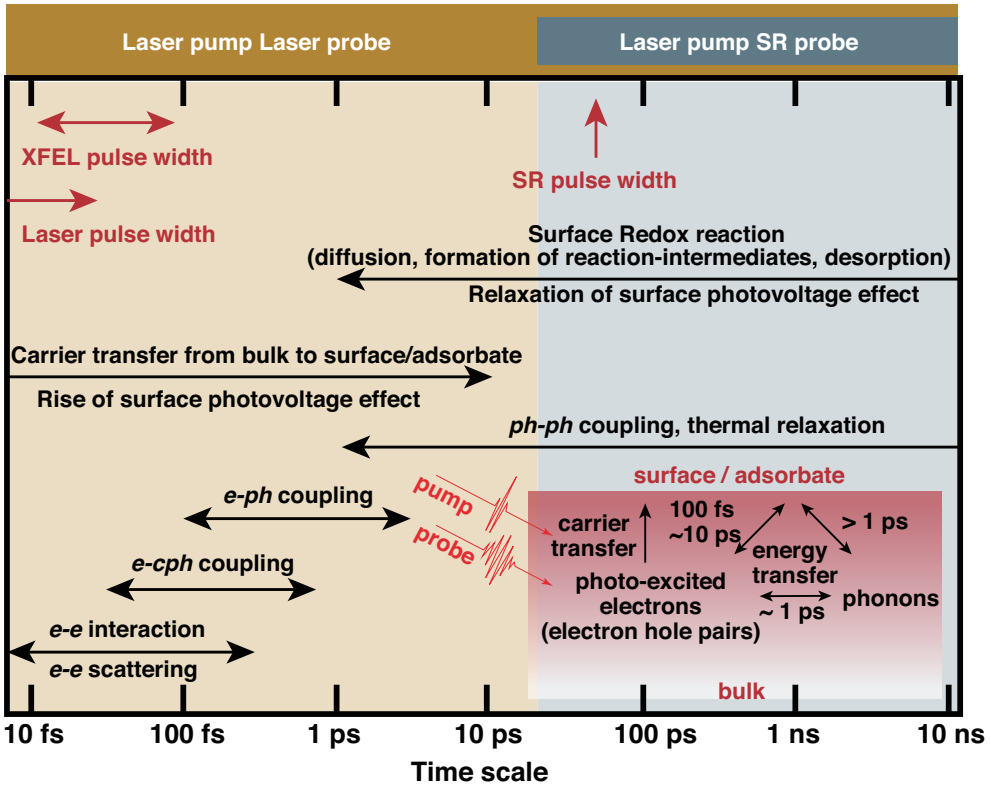

FIGURE 3.12: Various chemical and physical phenomena and their time scales. Typical time scale of XFEL, laser pulse width, and SR light sources are also shown for comparison [46].

3.2 Electrical conductivity measurement

There are various methods to obtain the electrical conductivities of solids or solid surfaces, such as two-probe method, four probes method, and van der Pauw method [48]. They have been developed to obtain accurate electrical conductivities for variously shaped materials. In this section, two-probes and four-probes electrical conductivity measurement systems, and linear four-point probes measurement systems are introduced.

3.2.1 Two- and four-probes electrical conductivity measurements

A two-probes method is the simplest method to measure the conductivity of a solid. Figure 3.13(a) illustrates schematic drawing of a two-probes electrical conductivity measurement system. In an equivalent circuit shown in Fig. 3.13(b), R_{S} represents the sample resistance, R_{Ci} $(i = 1, 2)$ is a contact resistance, and $R_{\mathrm{I-A}}$ and $R_{\mathrm{I-V}}$ represent the internal resistances of the voltmeter and ammeter, respectively. The typical resistances are $R_{\mathrm{I-V}} \sim 1$ GΩ, $R_{\mathrm{I-A}} \sim 1$ Ω, and R_{Ci} in the range of $0-1$ kΩ. As illustrated in the equivalent circuit in Fig. 3.13(b), Ohm's law $R_{\mathrm{S}} = V/A$ is valid only when R_{Ci} and $R_{\mathrm{I-A}}$ are small enough and $R_{\mathrm{I-V}}$ is large enough compared to R_{S}.

Figure 3.13(c) illustrates the schematic drawing of a four-probes conductivity measurement system. In this system, the voltmeter is separated from the current circuit, and little electrical current pass through the circuit with the voltmeter. As a result, no voltage differences are generated at the contacts with R_{C3} and R_{C4} in Fig. 3.13(d), and an accurate voltage difference at the sample can be measured. With the four-probes method, the sample resistance is obtained by

$$R_{\mathrm{S0}} \cong \frac{V}{A}. \tag{3.20}$$

The four-probes methods are widely used to obtain the resistances of small samples and samples with high electrical conductivities.

3.2.2 Linear four-probes electrical conductivity methods

Linear four-point probes systems in various dimensions are illustrated in Fig. 3.14 and listed in Table 3.1. The four-point probes with probe spacing (s) are mounted linearly on conductors of various dimensions in Fig. 3.14. l, w, and h are the length,

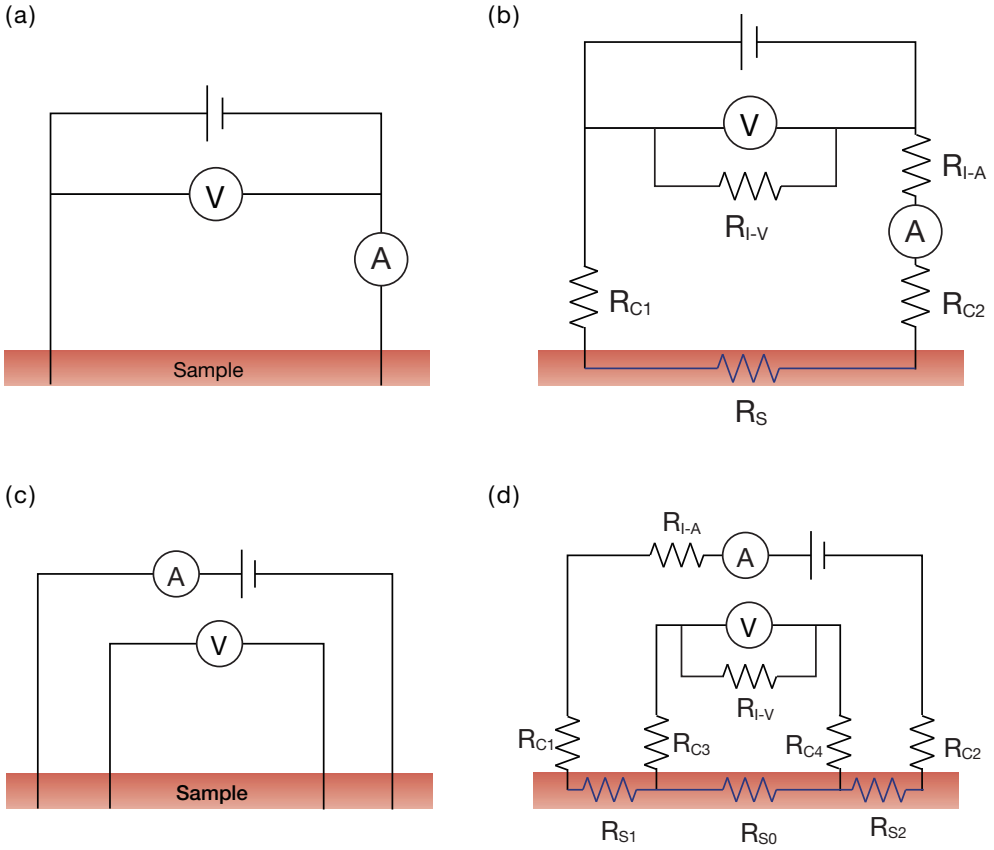

FIGURE 3.13: Schematic drawing of the two- and four-probes electrical conductivity measurement systems. A power supply, voltmeter and ammeter are connected to a sample with (a) two- and (c) four-probes. (b) and (d) are the equivalent circuit models of (a) and (c), respectively.

TABLE 3.1: Electrical conductivity in one, two, and three dimensional conductors. The sheet conductivity has the same dimension with the electrical conductivity Ω^{-1}. To clearly indicate the sheet conductivity, the unit is written as Ω^{-1}/squre or $\Omega^{-1}/\square$.

Dimension	Name	Expression	Unit
One	Wire conductivity	$\sigma_{1D} = \sigma \times h \times w$	$(\Omega^{-1}\mathrm{m})$
Two	Sheet conductivity	$\sigma_{2D} = \sigma \times h$	$(\Omega^{-1}/\square)$
Three	Bulk conductivity	$\sigma_{3D} = \sigma$	$(\Omega^{-1}\mathrm{m}^{-1})$

width, and height of a solid, respectively. (a) shows an one-dimensional conductor where $w, h \ll l$ and $l \ll s$, (b) shows a two-dimensional conductor like a metallic sheet where $h \ll s$ and $w, l \gg s$, and (c) shows a three-dimensional conductor where $w, h, l \ll s$. If the electrical conductivities are expressed by σ, resistances are given by

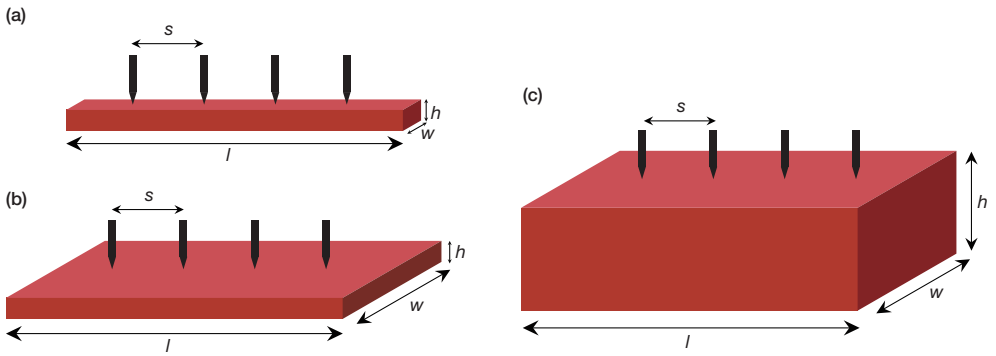

FIGURE 3.14: Schematic illustrations of linear four-point probes on (a) one dimensional, (b) two dimensional, and (c) three dimensional conductors. The probes are linearly mounted on the conductors in equal spacing of s.

the equations:

$$\text{Wire resistance:} \quad \frac{\Delta V}{I} = \frac{1}{\sigma}\frac{s}{hw} \propto s, \tag{3.21a}$$

$$\text{Sheet resistance:} \quad \frac{\Delta V}{I} = \frac{1}{\sigma}\frac{1}{hw}\ln 2, \tag{3.21b}$$

$$\text{Bulk resistance:} \quad \frac{\Delta V}{I} = \frac{1}{\sigma}\frac{1}{2\pi s}, \tag{3.21c}$$

where ΔV is the potential difference between the interior probes, and I is the electric current flowing between the outer probes.

One of the important points in these equation is in the relation between $\Delta V/I$ and the probe spacing s. Values of $\Delta V/I$ are proportional to s in a wire, and inversely proportional to s in a bulk, but is equal to the sheet resistance. Therefore, by monitoring $\Delta V/I$ with changing probes separations, one can know the dimension of conductors, and thus calculate the exact value of electrical conductivity σ. It should be noted that equations (3.21)(a-c) are obtained in a model where the ratios h, w, l are large enough against s.

3.2.3 Surface conductivity

Figure 3.15 illustrates the schematics of four-point probes measurement systems on surfaces and the paths of electric current [49, 50]. The semiconductor surface can generally be divided into three layers: a surface layer, a space charge layer, and a bulk layer. The total conductivity should be evaluated with three different conductivities at the each layer [see Fig. 3.15(b)]. A contribution of the bulk layer to the conductivity becomes small when the probe spacing is small enough. Conductivity changes during

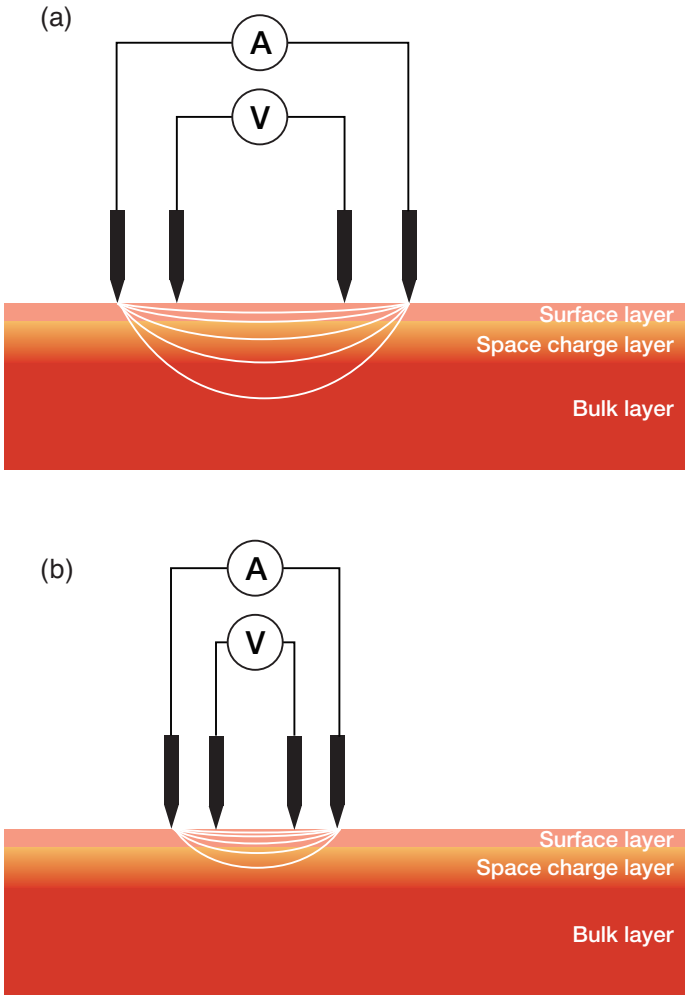

FIGURE 3.15: Schematic illustrations of the four-point probes conductivity measurements of the surface. White lines illustrate the paths of electric current [49, 50]. (a) When probe spacing is large, bulk properties contribute to the measured conductivity. (b) When the probe spacing is small, the bulk contribution to the measured conductivity can be neglected [51].

surface treatments can be attributed to changes at the surface layer or the space charge layer.

Chapter 4

Theoretical approach for multiple subband structures of wide-gap semiconductor surfaces

A simplified theoretical model that well reproduces the dispersion curves of the multiple subbands in a two-dimensional electron gas in the accumulation layer at the surfaces of wide-gap semiconductors is proposed in this chapter. The electronic band structures containing multiple subbands with different orbital characteristics are derived by self-consistently solving the Poisson-Schrödinger equations with anisotropic effective mass approximations. Calculations were carried out on the two-dimensional electron gas states formed at the surfaces of $SrTiO_3$ and ZnO for comparison. The calculated subband structures at the $SrTiO_3$ surface was in excellent agreement with those reported in a previous angle-resolved photoelectron spectroscopy experiment, confirming the validity of the present model. The calculations further indicate the existence of a high electron density, exceeding 2×10^{21} cm^{-3} and a high electric field of 20 $MVcm^{-1}$ at the surface.

4.1 Introduction

An electron gas localized at a surface or an interface is inherently two-dimensional (2D). It has intriguing low-dimensional properties that are significant for studying solid-state physics and in the development of electronic devices. A typical 2D electron system forms in the accumulation layer at a surface [52, 53]. An accumulation layer

is a type of space charge layer in an n-type semiconductor whose bulk band bends downward as it approaches the surface. The bulk band near a surface energetically splits into subbands when the thickness of the accumulation layer is thin enough to induce quantum confinement between the vacuum and the bulk band gap. With a sufficiently large band-bending effect, the subband minima in an accumulation layer can cross the Fermi level, generating 2D metallic states at the surface [53]. Such 2D metallic states in the accumulation layer have attracted increasing interest owing to their intriguing properties including 2D plasmon excitations, the Rashba effect, and band gap narrowing [54–56].

The energies of the subbands are fundamental parameters of the 2D metallic states. Various theoretical approaches have been carried out to calculate them. In the simplest approximation, the potential in the space charge layer is modeled as a triangle potential [57]. This is the so-called "wedge model" (see Appendix A.1). The energies of the subbands can be analytically solved in terms of Airy functions and they roughly match the experimental results. Alternatively, *ab initio* calculations have been carried out to accurately determine the band structures of the accumulation layer at semiconductor surfaces [23, 58, 59]. Whereas the theoretical results have shown fairly good agreement with the experiments, the calculations require long computation times and a large number of parameters. The *ab initio* approach is lacking in feasibility to deal with various types of surfaces. Therefore, a much simpler approach is required to evaluate the electronic structure of the 2D metallic states in an accumulation layer. In principle, proper determination of the electronic structure requires large calculations for self-consistently solving the Poisson-Schrödinger equations [60, 61]. Recently, King *et al*. adopted the modified Thomas-Fermi approximation (MTFA) proposed by Übensee *et al*. [62] (see Appendix A.2) to reduce the computational time and to reproduce their angle-resolved photoelectron spectroscopy (ARPES) results [24]. However, the application of this model is restricted to isotropic two-dimensional electron gas (2DEG) systems. Thus, calculations were performed on InAs, InN and In_2O_3 surfaces [24, 63] which have subbands with s-orbital symmetry.

In this chapter, a calculation method that is applicable to wide-gap semiconductors with multiple anisotropic subband structures is proposed. This model treats the subbands that have anisotropic energy dispersions with anisotropic effective-mass approximations (AEA) so the model can easily be applied to a variety of wide-gap semiconductor surfaces such as ZnO and $SrTiO_3$. Recently, researchers used ARPES to observe the anisotropic 2DEG subband structures of the d_{xy}, d_{yz} and d_{xz} orbitals in

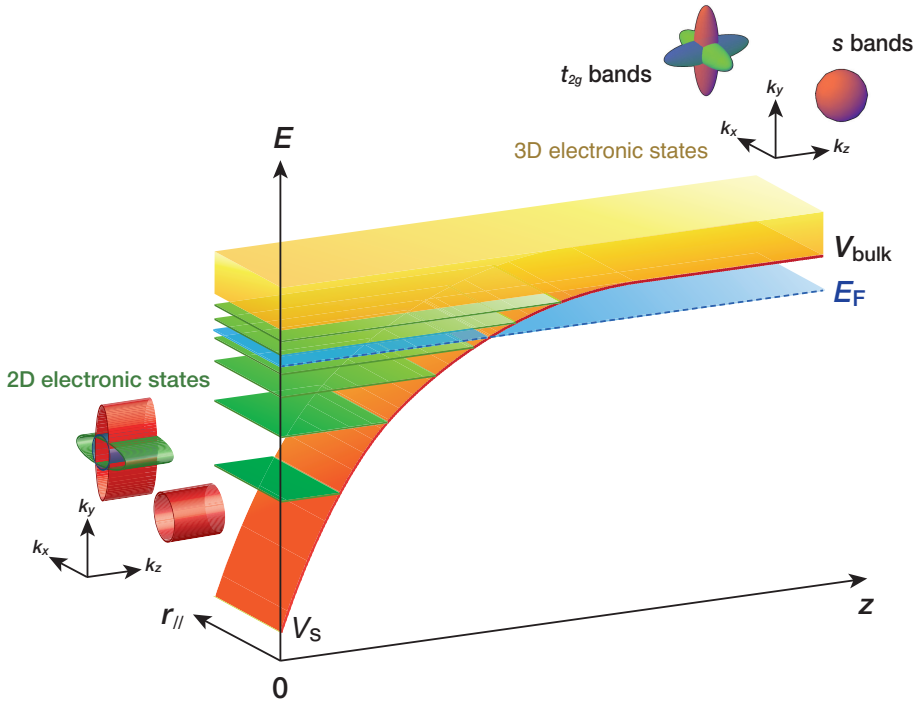

FIGURE 4.1: Schematic picture of the band bending at a semiconductor surface. The orange curved plate, yellow box above V_{bulk} and green sheets represent the potential curve $V(z)$, the bulk and 2D states, respectively. The Fermi surfaces of both the 3D and 2D states are illustrated in k space for the s and d-t_{2g} bands.

the accumulation layers in various $SrTiO_3(001)$ surfaces [19, 20, 23, 64, 65]. The present AEA model accurately reproduces the complicated electronic structures.

This chapter is organized as follows: Section 4.2 describes a theoretical approach to solve the band structures of an accumulation layer with the AEA model. In Section 4.3.1, the model is applied to an isotropic 2DEG system at a ZnO surface, where the conduction band is made of Zn 4s orbitals. Appropriateness of the AEA model is examined by comparing the calculated results with those of the MTFA and wedge models. In Section 4.3.2, the AEA model calculation is extensively performed on the anisotropic 2DEG system at the $SrTiO_3(001)$ surface. The calculated results are compared with experimentally-obtained ARPES data. In addition, the appearance of the 2D metallic states in the ARPES spectra is discussed in terms of their depth profile and the mean-escape-depth of the photoelectrons.

4.2 Theory

Here, we describe the development of an appropriate and simple model to calculate an accumulation layer containing anisotropic multiple subbands. The calculations are simplified by using the effective mass approximations and by separating the 2D electrons confined in the potential wall from the bulk electrons. Some of the notation in this chapter is the same as that used by Lüth [53], Abe *et al.* [66] and King *et al.* [24].

Here, the x- and y-axes are parallel to the surface and the z-axis is along the surface normal with $z = 0$ at the surface, as illustrated in Fig. 4.1. The anisotropic effective mass of an electron is represented by 3×3 tensors as $m_{\beta,\beta'}$, where $\beta, \beta' = x,\ y,\ z$. By taking the x-, y- and z-axes along the long or short axes of the bulk constant energy ellipsoids, the tensors are diagonalized and the effective masses of the electrons can be represented by three components along the three axes ($m_{\beta,\beta'} = m_\beta \cdot \delta_{\beta,\beta'}$).

In the anisotropic effective-mass model, the Schrödinger equation for a single particle in an accumulation layer is given by:

$$\left\{ -\frac{\hbar^2}{2m_{\alpha x}}\frac{\partial^2}{\partial x^2} \ -\frac{\hbar^2}{2m_{\alpha y}}\frac{\partial^2}{\partial y^2} \ -\frac{\hbar^2}{2m_{\alpha z}}\frac{\partial^2}{\partial z^2} + V(z) \right\} \Psi_\alpha(\boldsymbol{r}) = E_\alpha \Psi_\alpha(\boldsymbol{r}), \tag{4.1}$$

where $V(z)$ is the potential variation along the z direction and $\hbar$ is the reduced Planck's constant. Here, $m_{\alpha\beta}$, Ψ_α and E_α are the effective mass, the wave function and the energy of an electron in the α orbital, respectively. Here, $V(z)$ was set to ∞ at $z < 0$ for simplicity, because the work function was much larger than the magnitude of band-bending at the surface. Using a Bloch wave function with momentum parallel to the surface, the eigenfunction of subband j is given by

$$\Psi_{\alpha j}(\boldsymbol{r}) = \frac{1}{\sqrt{A}} \exp\{i\boldsymbol{k}_\parallel \boldsymbol{r}_\parallel\} \cdot \phi_{\alpha k_\parallel j}(z), \tag{4.2}$$

where $k_x x + k_y y = \boldsymbol{k}_\parallel \boldsymbol{r}_\parallel$, and A, k_β and $\phi_{k_\parallel j}$ are the normalization factor, the wavenumber along the β axis and the eigenfunction along the z axis, respectively. When $E_{\alpha j}(\boldsymbol{k}_\parallel)$ is given by the sum of $E_{\alpha\parallel}(\boldsymbol{k}_\parallel)$ and $E^0_{\alpha j}$, where $E_{\alpha\parallel}(\boldsymbol{k}_\parallel) = \hbar^2 k_x^2/(2m_{\alpha x}) + \hbar^2 k_y^2/(2m_{\alpha y})$, the one-dimensional Schrödinger equation along the z-axis is given by

$$\left\{ -\frac{\hbar^2}{2m_{\alpha z}}\frac{\partial^2}{\partial z^2} \ + V(z) \right\} \phi_{\alpha k_\parallel j}(z) = E^0_{\alpha j} \phi_{\alpha k_\parallel j}(z). \tag{4.3}$$

Here, $E^0_{\alpha j}$ is the eigenenergy of the subband minimum.

$V(z)$ can be obtained by solving the Poisson equation [24, 33]:

$$\frac{d^2V(z)}{dz^2} = -\frac{e^2}{\epsilon(z)\epsilon_0}\{N_\mathrm{D} \ - N_\mathrm{A} \ - n(z) \ + p(z)\}, \tag{4.4}$$

where e denotes the elementary charge, N_D is the bulk donor density, N_A is the bulk acceptor density, $n(z)$ is the electron density in the conduction band, and $p(z)$ is the hole density in the valence band. $\epsilon(z)$ and ϵ_0 are the relative and vacuum dielectric constants, respectively. For n-type wide-gap semiconductors, N_A and $p(z)$ can be neglected. Thus, Eq. (4.4) becomes

$$\frac{d^2V(z)}{dz^2} = -\frac{e^2}{\epsilon(z)\epsilon_0}\{N_\mathrm{D} \ - n(z)\}. \tag{4.5}$$

Eq. (4.5) can be further simplified by dividing the electron density into two components: the density of 3D electrons (n_3D), whose energies are larger than the potential deep inside the bulk (V_bulk), and the density of 2D electrons (n_2D), which are confined in the potential well, as shown in Fig. 4.1.

$$\begin{aligned} n(z) &= n_\mathrm{3D}(z) + n_\mathrm{2D}(z) && \text{(4.6a)} \\ &\approx n_\mathrm{3D} + n_\mathrm{2D}(z). && \text{(4.6b)} \end{aligned}$$

In Eq. (4.6b), n_3D is assumed to be constant against z. This assumption is valid when $n_\mathrm{2D}(z)$ is large enough so that the variation in $n_\mathrm{3D}(z)$ can be neglected.

n_3D and $n_\mathrm{2D}(z)$ can be obtained by integrating the density of states that are 3D in nature ($g_{\mathrm{3D},\alpha}$) and 2D in nature ($g_{\mathrm{2D},\alpha j}$) with respect to E.

$$\begin{aligned} n_\mathrm{3D} &= \sum_\alpha \int_{-\infty}^{\infty} dE \ g_{\mathrm{3D},\alpha}(E) f_\mathrm{FD}(E), && \text{(4.7a)} \\ n_\mathrm{2D}(z) &= \sum_{\alpha,j} n_{\alpha,j}(z) \\ &= \sum_{\alpha,j} \int_{-\infty}^{\infty} dE \ g_{2D,\alpha j}(E) \ f_\mathrm{FD}(E) |\phi_{\alpha k_\parallel j}(z)|^2, && \text{(4.7b)} \end{aligned}$$

where $n_{\alpha,j}$ is the partial electron density of each subband and $f_\mathrm{FD}(E)$ is the Fermi-Dirac function given by $f_\mathrm{FD}(E) = [1 + \exp\{(E - E_\mathrm{F})/(k_\mathrm{B}T)\}]^{-1}$. Here, k_B is the Boltzmann constant and T is the temperature of the semiconductor. n_3D and n_2D have the same dimension of m^{-3} because $|\phi_{\alpha k_\parallel j}(z)|^2$ has the dimension m^{-1}.

In the AEA model, the density of states for the 3D and 2D electrons, including the spin degeneracies, are given by

$$\begin{aligned} g_{3\mathrm{D},\alpha}(E) &= \frac{\sqrt{2m_{\alpha x}m_{\alpha y}m_{\alpha z}(E-V_{\mathrm{bulk}})}}{\pi^2\hbar^3} \\ &\quad \times\Theta(E-V_{\mathrm{bulk}}), \qquad (4.8\mathrm{a}) \\ g_{2\mathrm{D},\alpha j} &= \frac{\sqrt{m_{\alpha x}m_{\alpha y}}}{\pi\hbar^2}\Theta(E-E^0_{\alpha j}), \qquad (4.8\mathrm{b}) \end{aligned}$$

where Θ is the unit step function: $\Theta(x) = 1$ for $x \geq 0$ and 0 otherwise. Using Eq. (4.8b), Eq. (4.7b) can be rewritten so that it does not require any integration during the calculations:

$$\begin{aligned} n_{2\mathrm{D}}(z) &= \sum_{\alpha j}\frac{\sqrt{m_{\alpha x}m_{\alpha y}}}{\pi\hbar^2} \\ &\quad \times\int_{E^0_{\alpha j}}^{\infty} dE\left[1+\exp\left\{\frac{E-E_{\mathrm{F}}}{k_{\mathrm{B}}T}\right\}\right]^{-1}|\phi_{\alpha k_{\parallel} j}(z)|^2 \\ &= \sum_{\alpha j}\frac{\sqrt{m_{\alpha x}m_{\alpha y}}}{\pi\hbar^2}|\phi_{\alpha k_{\parallel} j}(z)|^2 k_{\mathrm{B}}T \\ &\quad \times\ln\left\{1+\exp\left(\frac{E_{\mathrm{F}}-E^0_{\alpha j}}{k_{\mathrm{B}}T}\right)\right\}. \qquad (4.9\mathrm{a}) \end{aligned}$$

Once the Fermi energy (E_{F}) has been obtained using Eq. (4.7a), by taking $N_{\mathrm{D}} = n_{3\mathrm{D}}$ in the bulk, Poisson's equation (4.5) can be simplified to

$$\frac{d^2V(z)}{dz^2} = \frac{e^2\ n_{2\mathrm{D}}(z)}{\epsilon(z)\epsilon_0}. \qquad (4.10)$$

Both $\phi_{\alpha k_{\parallel} j}(z)$ and $E^0_{\alpha j}$ can be calculated using Eq. (4.3) with the $V(z)$ value obtained with Eq. (4.10) (see Appendix A.3).

The potential at the surface can be written as $V_{\mathrm{s}} = V(0)$, and the surface carrier density can be written as N_{ss}, which is given by:

$$N_{\mathrm{ss}} = \frac{\epsilon(0)\epsilon_0}{e^2}\left[\frac{dV(z)}{dz}\right]_{z=0}. \qquad (4.11)$$

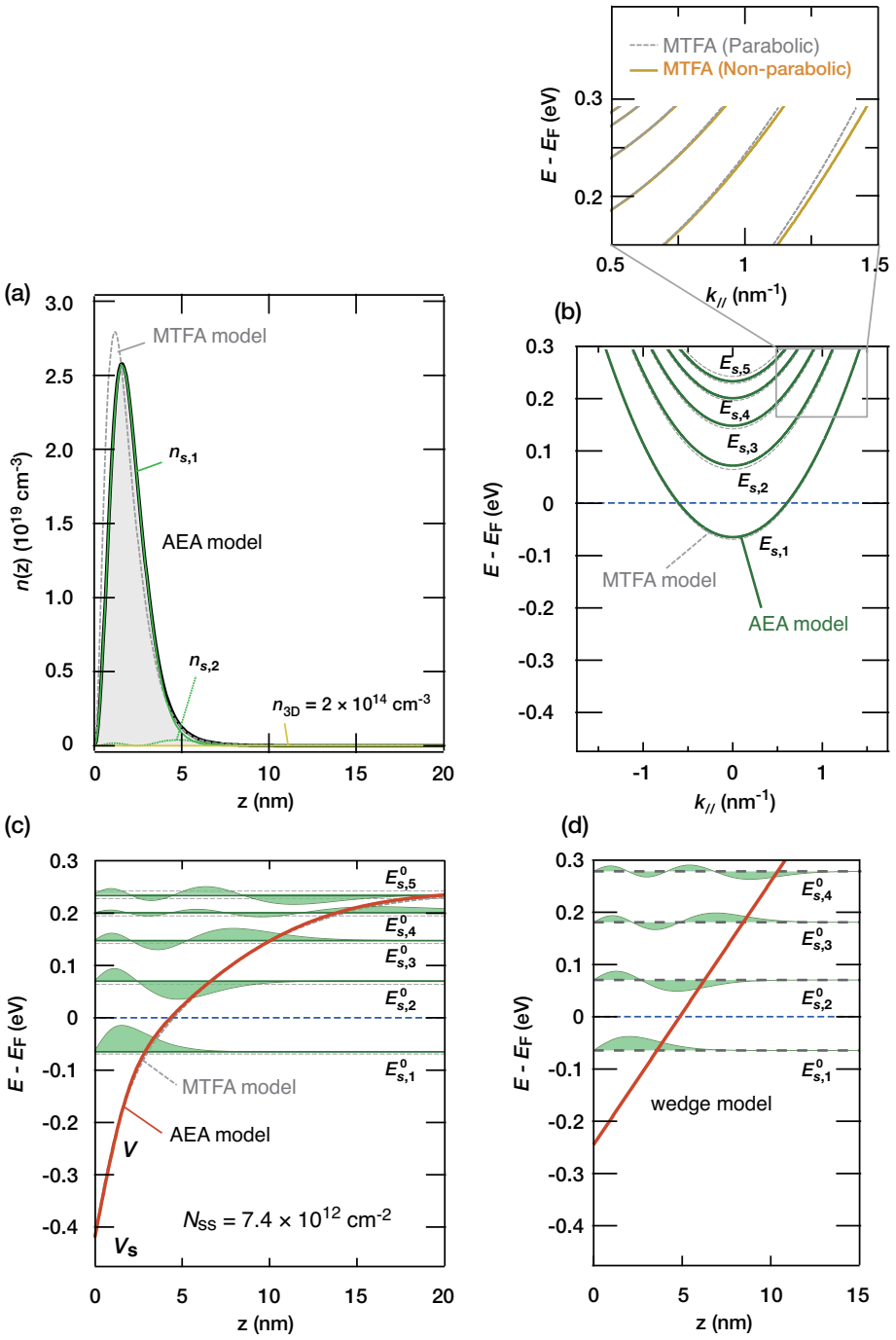

FIGURE 4.2: Distribution of the electron densities (a), dispersion curves of the subbands (b), and potential curves (c) for a ZnO surface calculated using the AEA (solid curves) and MTFA (gray dashed curves) models at room temperature (T = 300 K). The partial electron densities for the first and second subbands and n_{3D} are indicated with green curves and with an orange line in (a), respectively. The inset in (b) shows the parabolic (gray dashed) and non-parabolic (orange solid) dispersion curves for the ZnO conduction bands, obtained using the MTFA model. (d) The linear potential and eigenenergies of the subband minima were calculated using the wedge model. The corresponding eigenfunctions are displayed (filled green curves) for the AEA and wedge models in (c) and (d).

TABLE 4.1: List of the energies of the subband minima and the surface carrier densities calculated for a ZnO surface with the AEA, MTFA, and wedge models.

	V_s (eV)	$E^0_{s,1}$ (eV)	$E^0_{s,2}$ (eV)	$E^0_{s,3}$ (eV)	$E^0_{s,4}$ (eV)	N_{ss} (cm^{-2})
AEA	−0.420	−0.065	0.070	0.148	0.200	7.4×10^{12}
MTFA	−0.420	−0.068	0.064	0.142	0.195	7.8×10^{12}
wedge	−0.245	−0.065	0.070	0.181	0.279	

4.3 Results and discussion

4.3.1 Accumulation layer at a ZnO surface

In this subsection, the band structures for an accumulation layer at a ZnO surface are calculated with the AEA, MTFA, and wedge models to compare the results and validate the approximations employed in each model. ZnO is a wide-gap semiconductor with a conduction band made of isotropic Zn 4*s* orbitals. Because widely-spread *s* electrons are insensitive to the crystal structure, the Miller indexes of the ZnO crystals could be neglected for the calculation. The effective mass could be regarded as isotropic and it was set such that[1] $m_{s,x} = m_{s,y} = m_{s,z} = 0.21 m_e$, where m_e is the mass of a free electron.

The electron densities, band bending and corresponding eigenenergies were calculated at the ZnO surface with the AEA and MTFA models [Fig. 4.2(a–c)] and the wedge model [Fig. 4.2(d)]. The constants: $\epsilon(z) = 2.88$ [67], $N_D = 2.0 \times 10^{14}$ cm^{-3},[2] and $V_s = -0.42$ eV relative to E_F at $T = 300$ K were used in the MTFA and AEA models. V_s has an one-to-one correspondence with N_{ss} [see Eq. (4.11)], and V_s and N_{ss} were the initial parameters used in the calculations.

As listed in Table 4.1, the subband minima $E^0_{s,1} = -0.065$ eV, $E^0_{s,2} = 0.070$ eV and $E^0_{s,3} = 0.148$ eV, determined with the AEA model, were only slightly larger by 3 meV, 6 meV and 6 meV, respectively, than the energies determined with the MTFA model. The electron densities found using the MTFA model were distributed more on the surface side than those found using the AEA model [Fig. 4.2(a)]. Because only

[1] The theoretically or mathematically obtained effective masses of the ZnO crystal differ from $0.13 m_e$ to $0.3 m_e$, [see H. Morkoç and Ü. Özgur, *Zinc Oxide : Fundamentals, Materials and Device Technology*. (WILEY-VCH Verlag GmbH & Co. KGaA, Weinheim, 2009)]. Therefore, we used the mean value of them for the calculations in this thesis.

[2] The bulk carrier densities of ZnO and $SrTiO_3$ crystals used in this thesis are obtained by Hall measurements. The measurements have been carried out on hydrothermally-grown ZnO wafers (purchased from Goodwill Co., Russia) and on a Verneuil-grown $SrTiO_3$ wafer (Nb 0.05 wt% Nb-doped, purchased from Shinkosha Co. Ltd., Japan).

$E^0_{s,1}$ was located below the Fermi energy, the partial electron density of $n_{s,1}$ was much larger than the others.

To estimate the effect of the $\mathbf{k}\cdot\mathbf{p}$ perturbations on the subband structure at the ZnO surface, the subband structures were calculated using the MTFA model with a non-parabolic band dispersion, obtained using Kane's $\mathbf{k}\cdot\mathbf{p}$ perturbations [24, 68] [see inset in Fig. 4.2(b)]. When the band gap of a semiconductor is large enough, compared with both the spin-orbit splitting and the energy differences between the Fermi energy and the subband minima, modulation of the band structure by the $\mathbf{k}\cdot\mathbf{p}$ perturbations can be neglected. ZnO has a large band gap of 3.37 eV [69] and a small spin-orbit parameter of 0.016 eV [70]. Using these parameters, small energy differences (< 1 meV) in the subband minima $E^0_{s,j}$ between the parabolic and non-parabolic MTFA models were obtained. This result confirms that parabolic band dispersion is a reasonable approximation for the accumulation layers in wide-gap semiconductors.

Figure 4.2(d) shows the subband structures determined using the wedge model, where $E^0_{s,1}$ and $E^0_{s,2}$ were taken to have the same energies as those used with the AEA model. It was found that $V_{\rm s} = -0.245$ eV and $F = 5.0 \times 10^7$ eV/m. Although the conduction band edge of 5 nm at the Fermi energy is close to the values obtained using the AEA and MTFA models, there were large discrepancies in $V_{\rm s}$, $E^0_{s,3}$ and $E^0_{s,4}$.

When one considers a comparison with the experimental results, the accumulation layers at ZnO surfaces have been reported for hydrogen-, methanol- and water-adsorbed ZnO($10\bar{1}0$) surfaces [10, 12, 71] and on a hydrogen-adsorbed ZnO($000\bar{1}$) surface by ARPES experiments [12]. However, the subband structures were not clearly observed in these measurements because the ARPES results contained incoherent spectral tails at the peaks of the metallic bands. Systematic theoretical and experimental studies are required to properly understand the subband structures.

4.3.2 Accumulation layer at the $SrTiO_3$(001) surface

The accumulation layer at the $SrTiO_3$(001) surface was calculated using the AEA model proposed in this chapter. The conduction bands for the $SrTiO_3$ crystal are originated from the Ti 3d t_{2g} bands of the d_{xy}, d_{yz} and d_{xz} orbitals. Because the wave function of the d_{xy} electrons extends in the xy plane, the transfer integral of the d_{xy} electrons is larger than that in the plane along the z direction. Therefore, the effective mass of the d_{xy} electrons is anisotropic, with smaller values along the x and y directions than along the z direction. The same discussion can be applied for the d_{yz} and d_{xz}

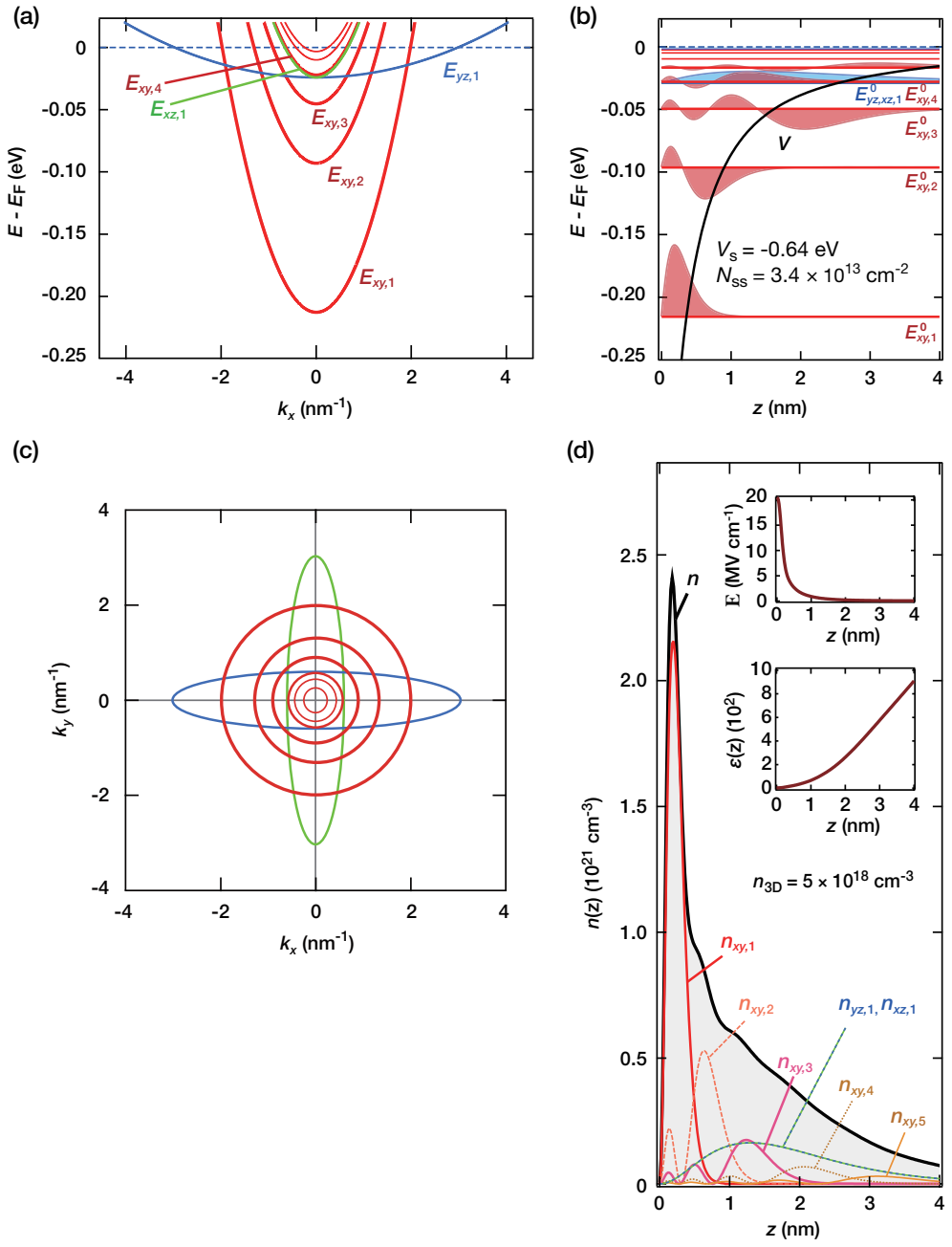

FIGURE 4.3: Calculated results for an accumulation layer at a $SrTiO_3(001)$ surface with $N_{ss} = 3.4 \times 10^{13}$ cm^{-2} at $T = 25$ K. (a) Band dispersion curves along the k_x direction for the d_{xy} (red), d_{yz} (blue) and d_{xz} (green) orbitals. (b) Potential variation and the subband energy minima. The corresponding eigenfunctions are shown for $j = 1{-}5$ for d_{xy} (filled red curves), $j = 1$ for d_{yz} and d_{xz} (filled blue curve). (c) Fermi surface map for the k_x and k_y plane. (d) Total electron density (black solid) and partial electron densities of each subband. The variations in the electric field and dielectric constant are shown in the insets.

electrons (Table 4.2). Here, the x-, y- and z-axes were set along the [100], [010] and [001] directions of $SrTiO_3$, respectively.

TABLE 4.2: List of the effective masses of the $SrTiO_3$ Ti $3d$ bands for the d_{xy}, d_{yz} and d_{xz} orbitals, relative to m_e [20, 23].

	m_x	m_y	m_z
d_{xy}	0.7	0.7	14
d_{yz}	14	0.7	0.7
d_{xz}	0.7	14	0.7

Because $E^0_{\alpha j}$ was calculated using Eq. (4.3) with $m_{\alpha z}$ and $V(z)$, essentially an electron with a larger $m_{\alpha z}$ has a lower subband minimum than an electron with a smaller $m_{\alpha z}$ (see Appendix A.3). Therefore, the d_{xy} electrons have lower energies than the d_{yz} and d_{xz} electrons in the accumulation layer and the degeneracy of the three bands at $\boldsymbol{k}_{\parallel} = 0$ is lifted.

The effective mass parameters for the three orbitals in Table 4.2 were used in the calculations on the accumulation layer. The dielectric constant of a $SrTiO_3$ crystal depends on the temperature and the electronic field [72–75]. Therefore, the field-dependent dielectric constant proposed by Copie *et al.* was used [75]:

$$\epsilon(z) = \frac{\epsilon^0}{1 + \frac{\mathbb{E}(z)}{\mathbb{E}_c}}, \tag{4.12}$$

where $\mathbb{E}(z) = \frac{1}{e}\frac{dV(z)}{dz}$ is the electric field at z, $\mathbb{E}_c$ is the critical electric field and ϵ^0 is the dielectric constant at $\mathbb{E} = 0$. The values $\mathbb{E}_c = 470$ kVm^{-1} and $\epsilon^0 = 13000$ at $T = 25$ K were used in the calculations [72, 75]. For $N_D = 5 \times 10^{18}$ cm^{-3}, the conduction band minimum was located about 1 meV below E_F in the bulk.

The results calculated with $N_{ss} = 3.4 \times 10^{13}$ cm^{-2} are shown in Fig. 4.3 and listed in Table 4.3. $E^0_{xy,1}$, $E^0_{xy,2}$ and $E^0_{xy,3}$ were located at -0.215 eV, -0.096 eV and -0.050 eV relative to E_F, respectively, and both $E^0_{yz,1}$ and $E^0_{xz,1}$ were degenerate at $\boldsymbol{k}_{\parallel} = 0$ and located at -0.029 eV. In Table III and in Fig. 4.4, the calculated results are compared with the experimental ARPES results measured on a cleaved $SrTiO_3(001)$ surface [23]. All of the calculated results agree with the ARPES results, within the experimental resolution. This indicates that the potential modulation by the atomic nuclei was not significant for the itinerant d electrons in the conduction band even though the electron density was densely distributed over the surface of the atomic layer, as shown in Fig. 4.3(d). A sharp increase in the potential and a moderate increase in the dielectric constant from the surface to $z \sim 0.4$ nm are shown in Fig. 4.3(d). Moreover, a large

TABLE 4.3: List of the subband minima, calculated with the AEA model (upper) and estimated from the ARPES data measured on a $SrTiO_3(001)$ surface (lower) shown in Fig 4.4 [23].

	V_s (eV)	$E^0_{xy,1}$ (eV)	$E^0_{xy,2}$ (eV)	$E^0_{xy,3}$ (eV)
AEA	-0.640	-0.215	-0.096	-0.050
ARPES results [23]		-0.21 ± 0.02	-0.105 ± 0.015	-0.045 ± 0.01

	$E^0_{yz,1}$, $E^0_{xz,1}$ (eV)	N_{ss} (cm^{-2})
AEA	-0.029	3.4×10^{13}
ARPES results [23]	-0.03 ± 0.01	

electron density exceeding 2×10^{21} cm^{-3} and a high electric field of 20 MV cm^{-1} were calculated at the surface. At the accumulation layer, $n(z)$ was large compared with n_{3D}, confirming the validity of Eq. (4.6b). N_{ss} was set to the initial parameter used in the calculations.

After the subband energies were obtained from the ARPES measurements, $V(z)$ and the partial electron densities could be calculated using the AEA model. The partial electron density distribution obtained gives further insight into the ARPES intensities, which is helpful for analyzing ARPES results. Figure 4.3(d) shows that most of $n_{xy,1}$ is confined at $z < 0.6$ nm, whereas $n_{yz,1}$ and $n_{xz,1}$ were spread over 4 nm. From the distributions of the partial electron densities, the mean-escape-depth of the photoelectrons (analyzing depths, $L^A_{\alpha,j}$) and the ARPES intensity ($I_{\alpha,j}$) could be obtained by

$$L^A_{\alpha,j}(\lambda) = \frac{\int_0^\infty dz\ n_{\alpha,j}(z) \exp(-z/\lambda)}{\int_0^\infty dz\ n_{\alpha,j}(z)} \tag{4.13a}$$

$$I_{\alpha,j}(\lambda) = \int_0^\infty dz\ n_{\alpha,j}(z) \exp(-z/\lambda), \tag{4.13b}$$

where λ is the mean-free-path of a photoelectron. Here, the matrix elements and cross sections of the photoemission process were not considered for simplicity. $L^A_{\alpha,j}(\lambda)$ and the ARPES intensity ratios [$= I_{\alpha,j}(\lambda)/\{\sum_{\alpha',j'} I_{\alpha',j'}(\lambda)\}$] are plotted as a function of λ in Fig. 4.5. When λ is smaller than 1 nm, all of the analyzing depths are located below 0.4 nm and they are within the first unit cell, whereas $L^A_{yz,1}$, $L^A_{xz,1}$, $L^A_{xy,4}$ and $L^A_{xz,5}$ exceed 1.5 nm when $\lambda > 10$ nm. The large intensity ratio of $I_{xy,1}/I_{yz,1} = I_{xy,1}/I_{xz,1} \sim 6$ at $\lambda = 1$ nm becomes smaller than 2 at $\lambda > 10$ nm. Because the mean-free-paths of the photoelectrons with kinetic energies of 10−500 eV are on the order $\lambda < 1$ nm [39], most of the photoelectrons elastically emitted by synchrotron radiation or by a He lamp are in the first unit cell and the ARPES signals of the d_{xz} and d_{yz} electrons are

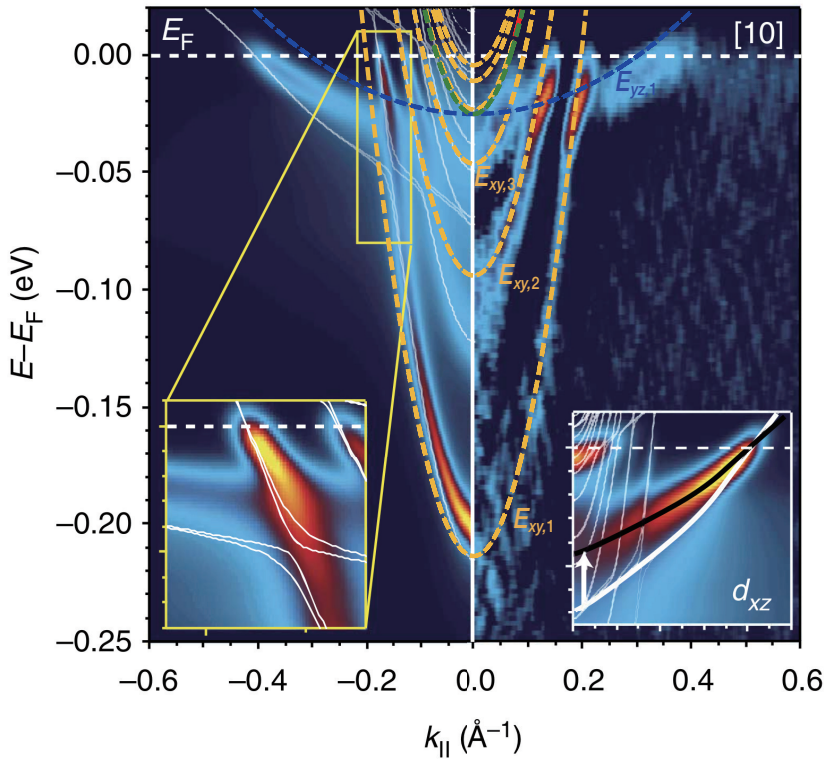

FIGURE 4.4: Comparison of the calculated results with the ARPES results taken at a $SrTiO_3(001)$ surface. Band dispersion curves calculated with the AEA model (dashed curves) are displayed on the calculated electron spectral function $A(k,\omega)$ (left) and the curvature analysis [76] of the ARPES data of the $SrTiO_3(001)$ surface taken at 20−30 K along the (100) direction using *s*-polarized photons of 51 or 55 eV (right) [23]. The kinks in the d_{xy} subband and the d_{xz} subband are shown in the left and right insets, respectively. The $SrTiO_3$ crystal was cleaved *in situ* and exposed to intense UV synchrotron light to saturate the formation of the 2DEG.

easily suppressed by those from the d_{xy} electrons. However, when a laser is used as the probing light, the kinetic energies of the photoelectrons are small (< 5 eV) and the mean-free-path is $\lambda > 10$ nm. In this case, most of the photoelectrons from the $d_{xy,1}$ and $d_{yz,1}$ bands are excited in the 1st and 4th unit cells, respectively.

4.4 Conclusion

We proposed a simple and effective anisotropic approach to self-consistently solve the Poisson-Schrödinger equations to reproduce previous ARPES results. The calculated electronic structures of a 2DEG at a ZnO surface revealed that the AEA and MTFA models yielded similar results and the structures were barely reproduced by the

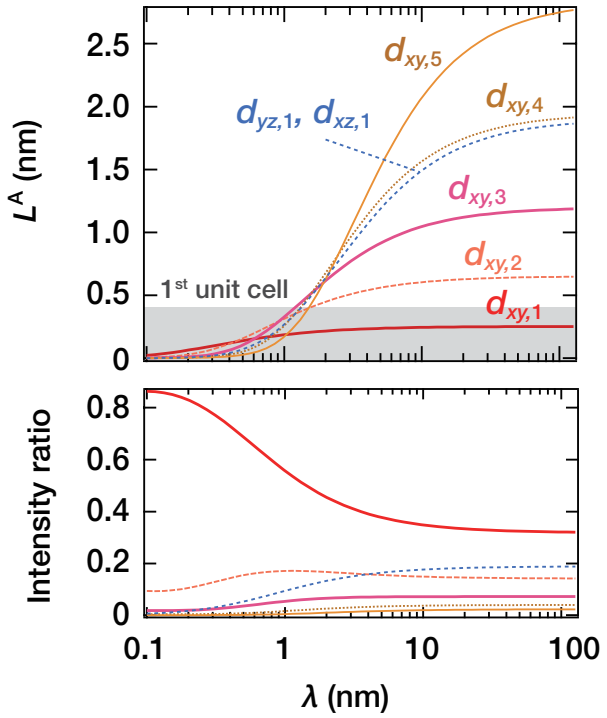

FIGURE 4.5: Analyzed depths (upper) and ARPES intensity ratios (lower) for the corresponding subbands, plotted as a function of the mean-free-path of a photoelectron.

wedge model. The *d*-derived multiple subband structures at the $SrTiO_3$ surface were obtained using the AEA model. The calculations successfully reproduced the experimentally determined subband structures, confirming the validity of the model. From the calculations, a large electron density exceeding 2×10^{21} cm^{-3} and a high electric field of 20 MV cm^{-1} at the surface were obtained. Moreover, we believe that the mean-escape-depths and intensities of the photoelectrons obtained by the calculations give further insight into the ARPES results.

Chapter 5

Hydrogen-induced metallization of $SrTiO_3(001)$ surfaces

Surface metallization of $SrTiO_3(001)$ by hydrogen adsorption is experimentally confirmed for the first time by photoelectron spectroscopy (PES) and surface conductivity measurements. The metallic state is assigned to a quantized state in the space charge layer induced by electron doping from hydrogen atoms. The measured 2D conductivity is well above the 2D Ioffe-Regel (2D-IR) limit indicating that the system is in a metallic conduction regime. The mean free path of the surface electron is estimated to be several nm at room temperature. The metallic band structure of the hydrogen-adsorbed $SrTiO_3(001)$ surface is studied by polarization-dependent PES.

5.1 Introduction

Transition-metal oxides, especially perovskite-type oxides, have been extensively studied in the past decades for their wide range of interesting properties such as superconductivity, magnetoresistance, and ferroelectricity. Until recently, it was believed that due to their chemical complexity these oxides could not be used for oxide based electronics. However, it is now widely admitted that oxide also devices not only can meet the standard, of semiconductor-based electronics but also show new intriguing properties due to electron correlations [77]. Among those oxides, $SrTiO_3$ appears as a key material for this new emerging field of all-oxide electronics [78, 79]. A first breakthrough was achieved with the discovery of a two-dimensional electron gas (2DEG) at the interface of the two insulating oxides $LaAlO_3$ and $SrTiO_3$ [80]. This system

attracted great interest and further studies revealed that this interface not only shows high mobility electron gas [13] but also large magnetoresistance [15] and even superconductivity [18]. Yet, the detailed mechanisms giving rise to the conductivity at the interface are still not understood. Proposed explanations involve different processes at the interface such as La diffusion [81], oxygen vacancies [14, 82] or electronic reorganization to avoid polar catastrophe [83]. Moreover, recent angle-resolved photoemission studies evidenced a highly metallic universal 2DEG at the vacuum-cleaved STO surface, suggesting that the properties of STO surface itself might actually play a crucial role in metallization of the $LaAlO_3/SrTiO_3$ interface [19, 20]. Difficulty in the interpretation is partly due to sample preparation of the oxide surfaces or interfaces. As mentioned above, preparation of heterojunctions or crystal cleavage are associated with possible diffusion of metal atoms and creation of oxygen vacancies.

On the other hand, it has been predicted recently by *ab initio* calculations that hydrogen adsorption on a SrO or TiO_2 terminated $SrTiO_3$(001) surface leads to a metallic state at the surface [84]. Such H-induced metallization was already reported for H/ZnO [10] and H/β-SiC [85] crystal surfaces. In the case of $SrTiO_3$ surface, the metallicity is assigned to the bulk band-bending near the surface, where the bulk conduction band is filled with electrons donated from the H atoms on the surface [84]. As hydrogen adsorption on a crystal surface prepared under ultrahigh vacuum (UHV) is a well-controlled procedure, experimental examination of the H-induced metallization of a $SrTiO_3$(001) surface is strongly called for.

In the present study, we have performed both photoemission and transport experiments on the H/$SrTiO_3$(001) system. We find a dispersing metallic band and an increase of the surface conductivity after H adsorption. The metallic state is assigned to a quantized state in the space charge layer near the surface. After the metallization, an electronic state is found in the bulk band gap (in-gap state, IGS) and a state, assigned to the O-H bond, is also observed. The details of the O-H bond is described in Sec. 5.3. The measured two-dimensional (2D) conductivity exceeds the 2D-IR limit, indicating band conduction regime, and the mean free path of surface electrons is estimated to be several nm at room temperature. The metallic band structure of the hydrogen-adsorbed $SrTiO_3$(001) surface is studied by polarization-dependent photoelectron spectroscopy measurements.

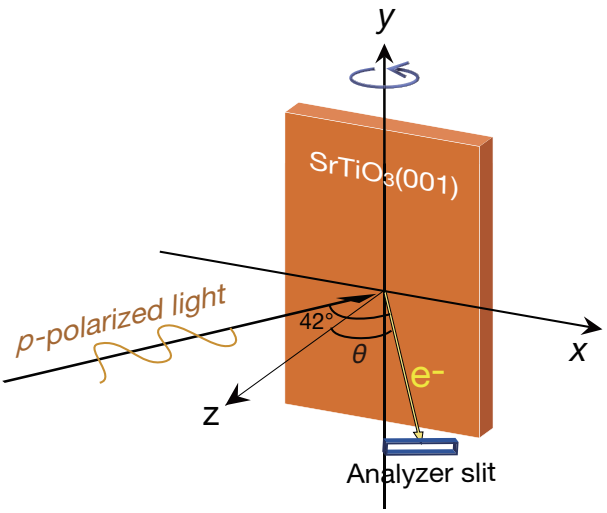

FIGURE 5.1: Schematic drawing of the experimental geometry of the PES measurements. The x, y, and z axes are set parallel to the [100], [010], and [001] directions of the STO crystal, respectively. The angle between the analyzer slit and the incident light was fixed to 42°.

5.2 Experimental setup for surface metallization

The electronic structure of the clean and H-adsorbed $SrTiO_3(001)$ surfaces has been investigated by core-level and valence band photoelectron spectroscopy measurements at the TEMPO beamline, SOLEIL, France [86, 87] and at the beamline BL07LSU, SPring-8. The measurements were performed with p-polarized light under ultra-high vacuum conditions (base pressure of 4×10^{-8} Pa) at room and low temperature (~ 20 K). Schematic drawing of the experimental setup for the PES measurements is shown in Fig. 5.1. The energy and angle resolution were 60 meV and 0.3°, respectively. Electrical conductivity was measured *in situ* during H-exposure by four terminal method under UHV conditions with linearly aligned four probes.

We used n-type $SrTiO_3(001)$ wafers (0.05 wt% Nb-doped, PI-KEM Ltd., U.K. and Shinkosha Co. Ltd., Japan). Before the introduction of the wafers into the UHV chambers, they were treated with buffered HF solution (pH$\sim$ 3.5) for 30 s, followed by rinsing with distilled water. This process is known to leave the (001) surface terminated by a TiO_2 plane [88]. Most of the previous photoemission researches on STO have been done on cleaved [19, 20, 89] or annealed [88, 90–94] surfaces. However, cleavage and annealing of the STO samples in UHV chambers are considered to make oxygen vacancies on the surfaces [20, 95, 96]. In order to avoid the oxygen vacancies on the surface, a clean STO(001) surface was prepared by annealing at 870 K under $6 \times$

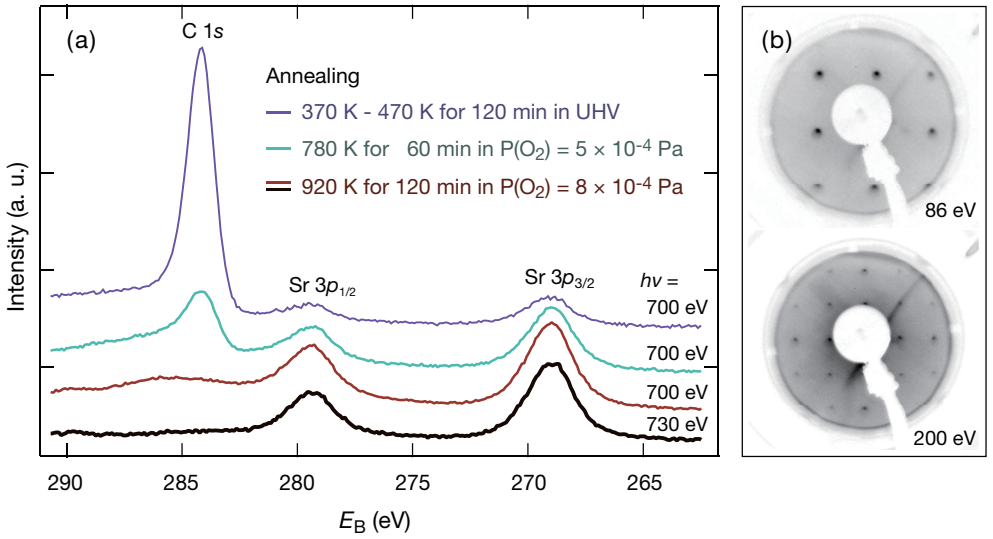

FIGURE 5.2: (a) Core-level PES spectra of the $SrTiO_3(001)$ crystal prepared with different annealing procedures. (b) LEED patterns of $SrTiO_3(001)$ prepared by annealing the crystal at 980 K in the oxygen pressure of 6×10^{-4} Pa for 120 min. The images are taken with the electron energies of 86 eV and 200 eV. The broad peak at $E_B = 285$ eV observed with $h\nu = 700$ eV is attributed to an Auger peak.

10^{-4} Pa of oxygen gas (99.999 % purity). Under these conditions, negligible carbon contamination and the absence of Sr segregation or oxygen vacancies were confirmed by the observation of C 1s, Sr 3d, Ti 2p/O 1s core-level photoemission spectra, respectively [97]. Figure 5.2(a) shows the core-level PES spectra taken after the sequence of the heat treatments. The C 1s peak at the binding energy (E_B) of $E_B = 284$ eV are barely discernible after the heat treatments at 920 K for 120 minutes under 8×10^{-4} Pa of oxygen atmosphere. The broad peak at $E_B = 285$ eV observed with $h\nu = 700$ eV is not detected with $h\nu = 730$ eV. Therefore, the broad peak can be attributed to an Auger peak. A high-quality bulk truncated ordered surface was confirmed by observation of a sharp 1×1 pattern in low-energy electron diffraction [see Fig. 5.2(b)].

The $SrTiO_3(001)$ surface was exposed to atomic hydrogen produced by cracking hydrogen molecules with a hot tungsten filament. In order to prevent direct heating and contamination of the sample surface from the hot filament, a shielding cover was mounted between the sample and the filament. During the hydrogen adsorption, temperature near the sample was monitored. Increase of the monitored temperature during the hydrogen dosage was less than 30 K. No change of the photoemission spectra or surface conductivity was observed by exposing the sample to hydrogen molecules.

The dissociation rate of hydrogen molecules and the adsorption probability of hydrogen atoms depend on the experimental setup. The results for the H-covered surfaces showing saturation of the photoemission peak shift and of the conductivity change are referred to as "H-saturated" $SrTiO_3(001)$ surfaces.

5.3 Metallization of $SrTiO_3(001)$ surface

5.3.1 Photoemission study

Figure 5.3(a) shows photoemission spectra near the Fermi level for the clean, intermediate, and hydrogen saturated surfaces taken at $h\nu = 81$ eV. For the clean surface, no state is observed at the Fermi level, indicating its insulating behavior. With the hydrogen exposure, a sharp photoemission signal, denoted as Metallic State (MS), develops at the Fermi level. The H-saturated surface is metallic and thus the $SrTiO_3(001)$ crystal exhibits a surface insulator-to-metal transition or surface metallization by hydrogen adsorption. On the hydrogenated surface, an electronic state, located within the bulk band gap of $SrTiO_3(001)$, is observed at a binding energy of 1.5 eV. This in-gap state (IGS) has been reported in previous photoemission studies on electron-doped $SrTiO_3(001)$ crystals [98]. The origin of the IGS has been discussed based on various models: it has been attributed to a locally screened incoherent state of the Ti $3d$-O $2p$ band [98], a precursor of the "lower-Hubbard band" of the d^1 insulator [99], chemical disorder [89], and polaron effect [100]. The observation of the IGS on the well-defined surface in the present study seems to exclude the chemical origin such as an oxygen vacancy state. Valence-band photoemission spectra before and after hydrogen exposure, in Fig. 5.3(b), show also the appearance of a new state, assigned to the O-H bond. The hydrogen atoms likely adsorb on the oxygen sites, as predicted by first principle calculations [84].

Figure 5.4 shows wavenumber-resolved photoemission spectra of the H-saturated $SrTiO_3(001)$ surface around the Γ point. Two main features can be observed: a sharp peak as noted MS and a broader feature at around 200 meV. This might indicate that, whereas the MS band is a coherent state, the broad feature can be attributed to an incoherent state due to electron correlation effect [19, 101] or electron-phonon interaction [91]. The MS band shows dispersion with the band minimum at Γ and the Fermi wavenumber of $k_F = 2.0\ \mathrm{nm}^{-1}$. A parabolic fit to the band dispersion gives the effective mass of $m^*/m_e = 2.5$, where m_e is the free electron mass (Fig. 5.4). From the k_F value,

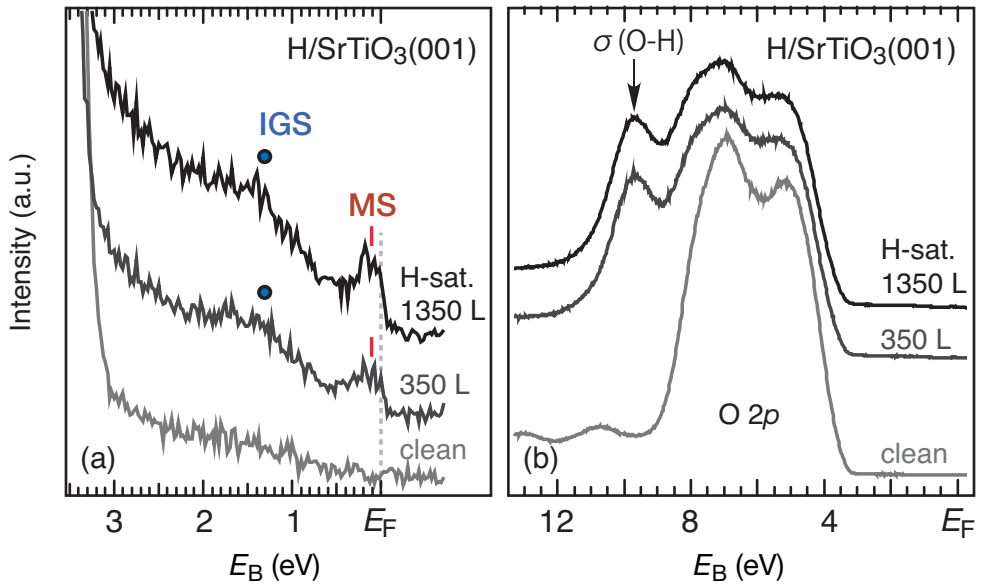

FIGURE 5.3: Normal-emission PES spectra of the bare, H-covered (intermediate coverage) and H-saturated $SrTiO_3(001)$ surfaces (a) at the Fermi level (E_F) and (b) at the O $2p$ band. The spectra were taken at $h\nu = 81$ eV at room temperature. MS indicates the metallic state and IGS the in-gap state.

the carrier density can be deduced to be $n_{2D} = 6 \times 10^{13}$ cm^{-2}, which gives around 0.1 electron per 2D unit cell. In this calculation, the circular shape of the Fermi surface is supposed, which is confirmed in Chapter 6.

To evaluate the bulk band change Ti $2p$ core-level photoemission spectra were measured before and after the H exposure, as shown in Fig. 5.5. The Ti $2p$ peak shifts by 200 meV toward higher binding energies by the band bending effect after H adsorption.

From the valence-band photoemission spectra on the clean surface in Fig. 5.4, the valence-band maximum (VBM) position is deduced to be around 3.1 eV below the Fermi level. Thus, the edge of the bulk conduction band is likely located around 100 meV above E_F for the clean $SrTiO_3(001)$ surface. After H deposition, taking into account a 200 meV downwards band bending, the conduction band minimum is located approximatively 100 meV below the Fermi level, lower than the minimum of the metallic state. MS state is thus attributed to a quantized state due to confinement in the potential well of the space charge layer [20]. The sample doping level is 10^{19} cm^{-3}. Taking the conduction- and valence-band density of states, $N_C(T) = 4.1 \times 10^{16} \cdot T^{3/2}$ cm^{-3} and $N_V(T) = 2.5 \times 10^{16} \cdot T^{3/2}$ cm^{-3}, respectively [102], we found from standard semiconductor equations that in the bulk STO the Fermi level is located 80 meV below the conduction band minimum. This means that on the clean surface the

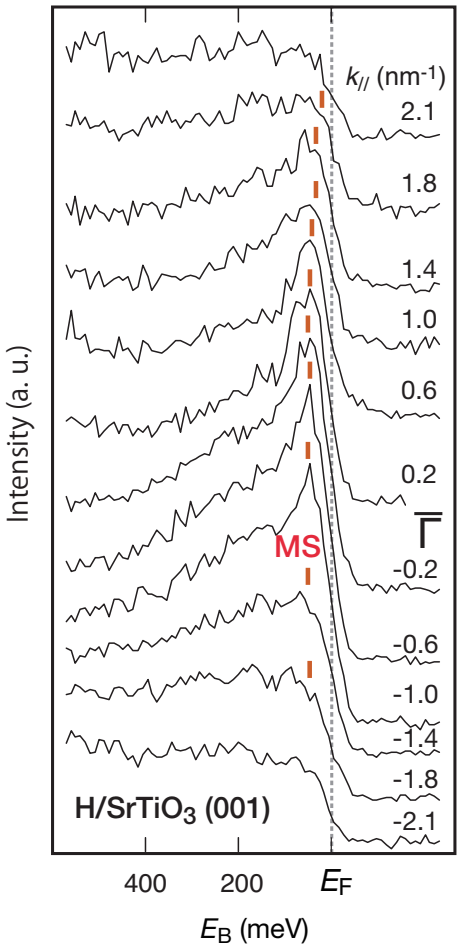

FIGURE 5.4: Wavenumber-resolved photoemission spectra of the H-saturated (1350 L) $SrTiO_3(001)$ surface along the Γ-X direction taken at $h\nu = 81$ eV and at 20 K. MS denotes the metallic state. The red line indicates the parabolic fit to the metallic state.

bands are bended upwards. Changes in band bending by H adsorption on $SrTiO_3(001)$ is schematically drawn in Fig. 5.6. With increasing H exposure, the conduction band at the surface is progressively filled with electrons from the hydrogen adatoms and the consequent downward shift eventually leads to the surface metallization. It should be noted that the peak shift shown in Fig. 5.5 does not indicate the exact energy shift at the topmost surface, because the observed PES intensities are the weighted sum of photoelectrons from titanium atoms located over the layers [103]. As shown in Fig. 3.4, the probing depth for the PES measurements is about 0.6 nm. Therefore, the actual energy shift at the surface may be larger than 200 meV. In order to discuss the band-bending structure more precisely, high-resolution ARPES measurements are required (see Chapter 6).

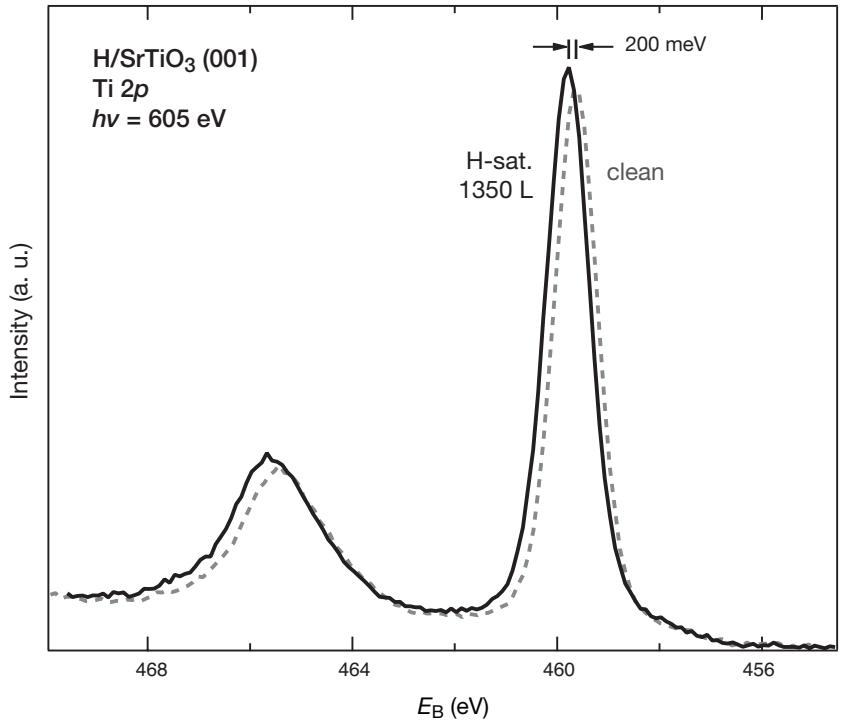

FIGURE 5.5: Ti 2p core-level photoemission spectra of the clean and H-saturated SrTiO$_3$(001) surfaces at room temperature. The photon energy is $h\nu = 605$ eV.

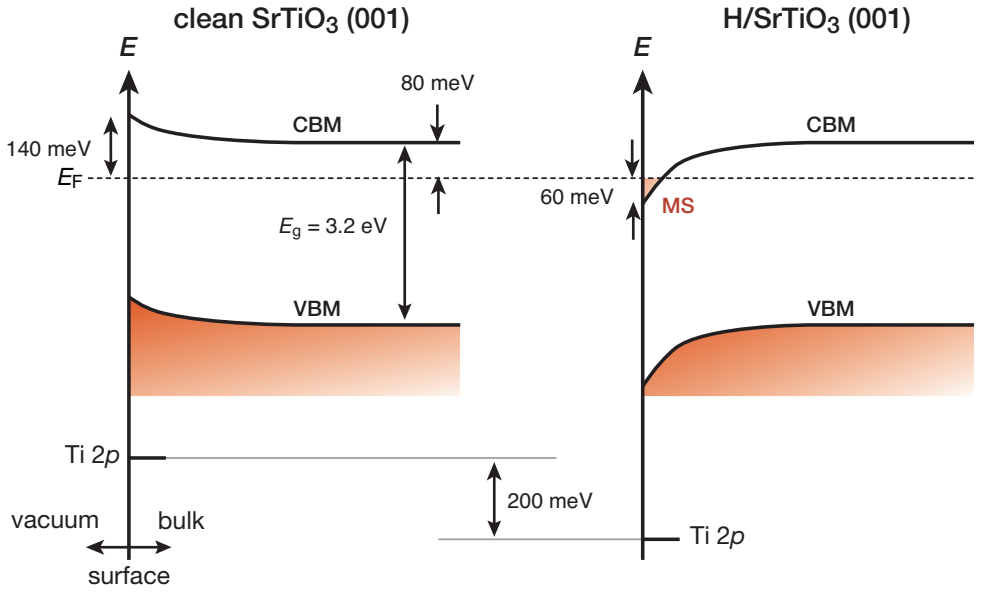

FIGURE 5.6: Schematic drawing of the band bending change induced by surface metallization during hydrogen adsorption on the SrTiO$_3$(001) surface. The Debye length is estimated to 6 nm.

5.3.2 Electrical conductivity measurements with four-point probes

The insulator-to-metal transition at the surface indicates an increase of the conductivity by hydrogen adsorption on the $SrTiO_3$(001) surface. To correlate with the changes in electronic structures observed by photoemission, surface conductivity measurements were performed for the H/$SrTiO_3$(001) system. The experimental setup is schematically drawn in Fig. 5.7(a). The probe distance was ~ 6 mm, which provided enough area between probes to make *in situ* transport measurement during the H adsorption on the surface [49, 50].

Figure 5.7(c) shows the sheet conductivity change, $\Delta\sigma$, of the $SrTiO_3$(001) surface as a function of H exposure. The $\Delta\sigma$ value was derived from the measured electrical resistance R by the relation, $\Delta\sigma = \frac{L}{W}\left(\frac{1}{R} - \frac{1}{R_0}\right)$, where L and W represent the length (8 mm) and width (5 mm) of the measured area. R_0 is the initial resistance of the clean surface and R the resistance of the surface after H deposition.

The transport results in Fig. 5.7(c) reveal an increase of the conductivity by the H adsorption. H adsorption is associated with changes only at the space-charge layer and there is no transport variation in the internal bulk. Since the largest contribution originates from an increase of carriers in the accumulation layers, as shown in Fig. 5.6, $\Delta\sigma$ after the saturation, $\Delta\sigma_{\mathrm{sat}} = 440\ \mu\mathrm{S}/\square$, corresponds to the conductivity of the H-saturated $SrTiO_3$(001) surface, $\Delta\sigma_{\mathrm{sat}} = \sigma_{\mathrm{H/STO}}$.

The conductivity measured on the H-saturated $SrTiO_3$(001) surface indicates that the electron transport is in the metallic conduction regime. Indeed, electron transport is in the metallic conduction regime if conductivity exceeds the 2D-IR limit, $\sigma_{\mathrm{2D-IR}} = e^2/h \cdot (k_{\mathrm{F}} l) = e^2/h \cdot (1) = 39\ \mu\mathrm{S}$, where k_{F} and l are the Fermi wavenumber and carrier mean-free path, respectively. In contrast, electron transport is in the hopping or strong localization regime if conductivity is smaller than $\sigma_{\mathrm{2D-IR}}$. Since $\sigma_{\mathrm{H/STO}}$ is much larger than $\sigma_{\mathrm{2D-IR}}$, the measured conductivity is in the band conduction regime and the increase agrees to the band-bending scenario in Fig. 5.6.

In addition, the electron mean free path of the H-saturated $SrTiO_3$(001) surface is derived to be $l \sim 2$ nm from the isotropic 2D Boltzmann equation [104], $\sigma_{\mathrm{H/STO}} = e^2/h \cdot (k_{\mathrm{F}} l)$. The relaxation time, $\tau = l/v_{\mathrm{F}}$, is thus $\tau = 7.5 \times 10^{-15}$ s, which is similar to those (10^{-15} s) evaluated from resistivity of Nb-doped $SrTiO_3$ crystals at room temperature [105] through the Drude model. The conduction process at room temperature is generally dominated by electron-phonon interaction. In the high temperature limit ($T > T_{\mathrm{D}}/3$ with $T_{\mathrm{D}} = 413$ K being the Debye temperature for $SrTiO_3$ [106]),

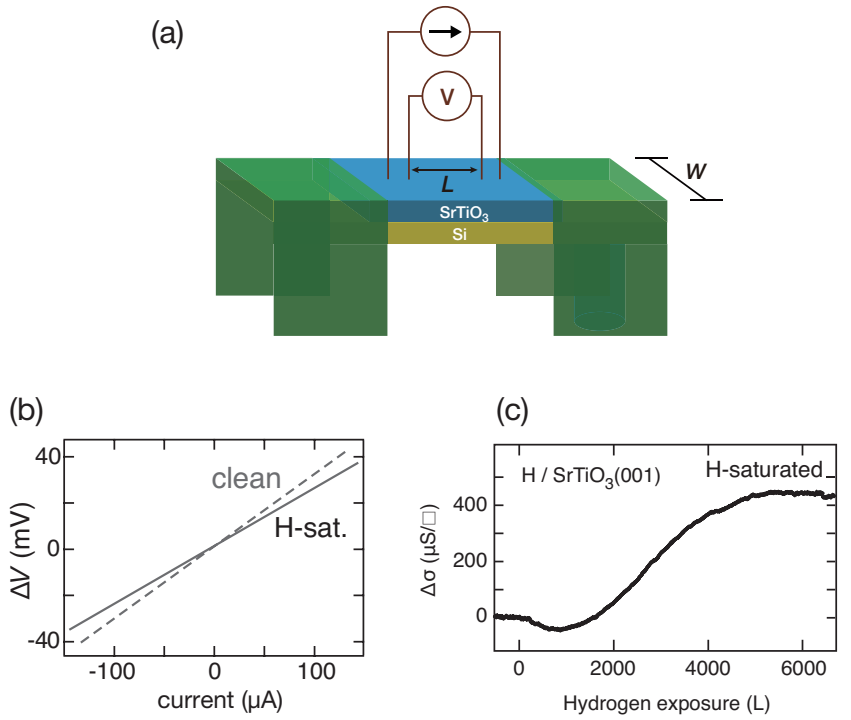

FIGURE 5.7: (a)Schematic drawing of 4-terminal method transport measurements on the H/SrTiO$_3$(001) surface. (b) Conductivity change, $\Delta\sigma$, with H exposure, referred to the conductivity of the clean surface. Measurements were performed at room temperature.

τ is given by $\tau \sim \tau_{e-ph} = \hbar/2\pi\lambda_{e-ph}k_{\mathrm{B}}T$ with λ_{e-ph} representing the strength of the electron-phonon coupling. From our experimental τ value, a relatively moderate value of $\lambda_{e-ph} = 0.5$ is obtained, which is comparable to the value from a previous photoemission study on the cleaved SrTiO$_3$ surface [107].

5.4 Polarization-dependent PES studies

In this section, metallic band structure of the hydrogen-adsorbed SrTiO$_3$(001) surface is studied by polarization-dependent PES measurements. With dipole-selection-rule argument, we attributed the metallic states into the Ti $3d_{xz}$, $3d_{yz}$, and $3d_{xy}$ bands. These t_{2g} bands are partially filled with electrons upon H-induced downward band bending at the surface. The energy splitting of the Ti $3d$ t_{2g} bands is considered to be induced by a quantum confinement along the surface normal (z) direction. The metallic peaks are accompanied by incoherent states induced by many-body interaction, which likely indicates that the electronic system forms a two-dimensional liquid phase.

The possible origin and the feature of these states and the in-gap state and the σ(O-H) state shall be discussed from the polarization dependence of the photoemission intensity. From changes of the Ti, Sr, and O core-level spectra by hydrogen adsorption, the hydrogen atoms are found to adsorb on the oxygen sites. In addition, from the size of Fermi surface, a net amount of the transferred electrons from hydrogen to the surface is estimated.

5.4.1 Experimental setup for the polarization-dependent PES studies

The polarization-dependent PES experiments have been carried out at the TEMPO beamline of SOLEIL and at BL07LSU of SPring-8, where p- and s-polarized undulator beams were available [45, 86, 87]. The measurements were made at 300 K and 80 K under UHV condition with a base pressure of $< 4 \times 10^{-8}$ Pa.

In this study, n-type STO(001) wafers (0.05 wt% Nb-doped, PI-KEM Ltd., U.K. and Shinkosha Co. Ltd., Japan) were treated with HF solution for 30 s and annealed in oxygen atmosphere using the same methods descried in Sec. 5.2. An ordered surface was ascertained by observation of a sharp 1×1 pattern of low-energy electron diffraction. Negligible carbon contamination was ascertained by absence of the C $1s$ peak in the core-level photoemission. Adsorption of atomic hydrogen on the STO(001) surface was made at room temperature by cracking hydrogen molecules with a hot tungsten filament under the atmosphere of hydrogen gas; $\mathrm{P(H_2)} = 1.5 \times 10^{-4}$ Pa.

5.4.2 Polarization dependencies of the photoelectron spectra

Measurement geometry for valence band photoelectron spectroscopy is schematically shown in Fig. 5.8(a) and (b). With the orthogonal basis defined on the surface, a set of polarization vectors of the incident light is expressed as $\mathbf{A} = (A_x,\, A_y,\, A_z) = (A^p \cos\alpha,\, A^s,\, A^p \sin\alpha)$, where A^p and A^s correspond to the p- and s-polarization vectors, respectively. The angle α is referred from the surface normal. Recalling the dipole approximation for the photoemission process [35], photoemission intensities taken with p-polarized (I^p) and s-polarized (I^s) photons, and the matrix element for the electron-photon interaction can be expressed as;

$$I^{s,p} \propto \left|\left\langle \Psi_f \left| \mathbf{A}^{s,p}_{pes} \cdot \nabla \right| \Psi_i \right\rangle\right|^2 A_{\mathrm{spectral}}, \tag{5.1}$$

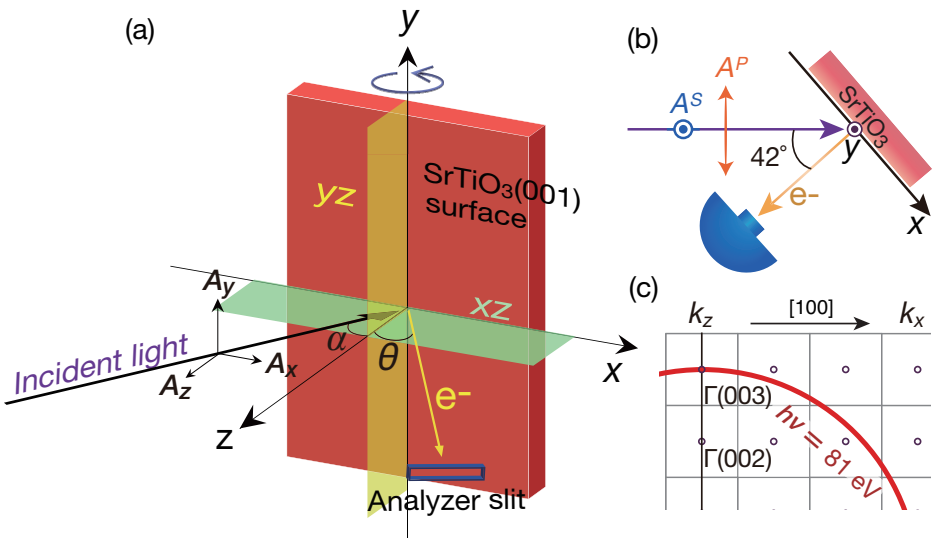

FIGURE 5.8: (a), (b) Schematic drawings of the experimental geometry with the light polarization vectors. The x, y, and z axes are set parallel to the [100], [010], and [001] directions of the STO crystal, respectively. The direction of the incidence light and the analyzer slit are in the xz mirror plane (green). Photoelectrons emitted in the yz mirror plane (yellow) are detected at the analyzer only at the normal emission ($\theta = 0°$) position. The sum of the incidence angle α and the emission angle θ was fixed at 42°. (c) Schematic representation of the Brillouin zones for the STO crystal in the [100]-[001] plane. Using an inner potential 12 eV measured from E_F [90], a sphere of the final-state free-electron at $h\nu = 81$ eV is obtained.

where $\mathbf{A}^s_{pes}$ and $\mathbf{A}^p_{pes}$ are the vector potentials of the incident light described by $\mathbf{A}^{s,p} = \mathbf{A}^{s,p}_{pes} e^{i(\omega t+\varphi)}$ with the phase shift φ. $|\Psi_i\rangle$ and $|\Psi_f\rangle$ are ket vectors in the initial and final states, respectively. The spectral function, A_{spectral}, contains coherent and incoherent parts of the photoemission process, which carries information about the many-body interaction of the probed electronic states [108, 109]. Briefly, a sharp peak and accompanying spectral tails correspond to the coherent and incoherent parts, respectively. The appearance of the photoemission tail has been regarded as a signature of strong many-body interaction, such as that in high-temperature superconductor [110].

In the present measurement configuration, photoemission intensities with polarized light are expressed in terms of the matrix elements as:

$$\begin{aligned} I^p &\propto \left|\left\langle \Psi_f \left| \mathbf{A}^p_{pes} \cdot \nabla \right| \Psi_i \right\rangle\right|^2 \\ &= A^2 \left| \int_{-\infty}^{\infty} dx \Psi_f^*(x,y,z) \frac{\hbar}{i} \frac{\partial}{\partial x} \Psi_i(x,y,z) \cos\alpha \right. \\ &\quad \left. + \int_{-\infty}^{\infty} dz \Psi_f^*(x,y,z) \frac{\hbar}{i} \frac{\partial}{\partial z} \Psi_i(x,y,z) \sin\alpha \right|^2, \qquad (5.2a) \\ I^s &\propto \left|\left\langle \Psi_f \left| \mathbf{A}^s_{pes} \cdot \nabla \right| \Psi_i \right\rangle\right|^2 \\ &= A^2 \left| \int_{-\infty}^{\infty} dy \Psi_f^*(x,y,z) \frac{\hbar}{i} \frac{\partial}{\partial y} \Psi_i(x,y,z) \right|^2, \qquad (5.2b) \end{aligned}$$

where the photon intensities are normalized to $|\mathbf{A}^{s,p}|^2 = A^2$.

When one assumes that the initial states and the final states are isotropic along the x, y, and z directions, the intensity ratio becomes $I^p/I^s = (\cos\alpha + \sin\alpha)^2 \approx 2.0$ at the normal emission geometry ($\alpha = 42^\circ$ in the present measurement condition). It is noted that, considering the existence of refraction and reflection on the STO surface, A_z ($= A^p \sin\alpha$) should be weakened inside the bulk [111], and therefore this intensity ratio would become smaller than the calculated value of 2. Thus, when the ratio is larger than 2, the state is considered to be mainly composed of the orbitals extending along the surface normal (the out-of-plane components). Similarly, if one assumes that the contribution to the matrix element from A_z is zero, the intensity ratio becomes $I^p/I^s = \cos^2\alpha \approx 0.55$. This simple analysis helps us to assign the anisotropy of an electronic state.

5.4.3 Polarization dependencies of the valence band

Figure 5.9(a) shows angle-integrated spectra of the clean STO and H/STO surfaces taken around $\theta = 0^\circ$ with p- and s-polarized light and using the transmission mode of the analyzer. Surface metallization was achieved by the 4000 L H-dosage (1 L $= 1.3 \times 10^{-4}$ Pa s). The metallic band is observed at the photon energy of $h\nu = 81$ eV, which corresponds to the $\Gamma(003)$ point in the momentum space as shown in Fig. 5.8(c). The spectra have been normalized to the photon flux (a drain current of the focusing mirror in the beamline). On the clean STO surface, the energy region between the Fermi level and the O $2p$ band-edge at $E_\mathrm{B} \sim 3$ eV corresponds to the bulk band gap, and there is no spectral feature in this energy region. By dosing hydrogen atoms

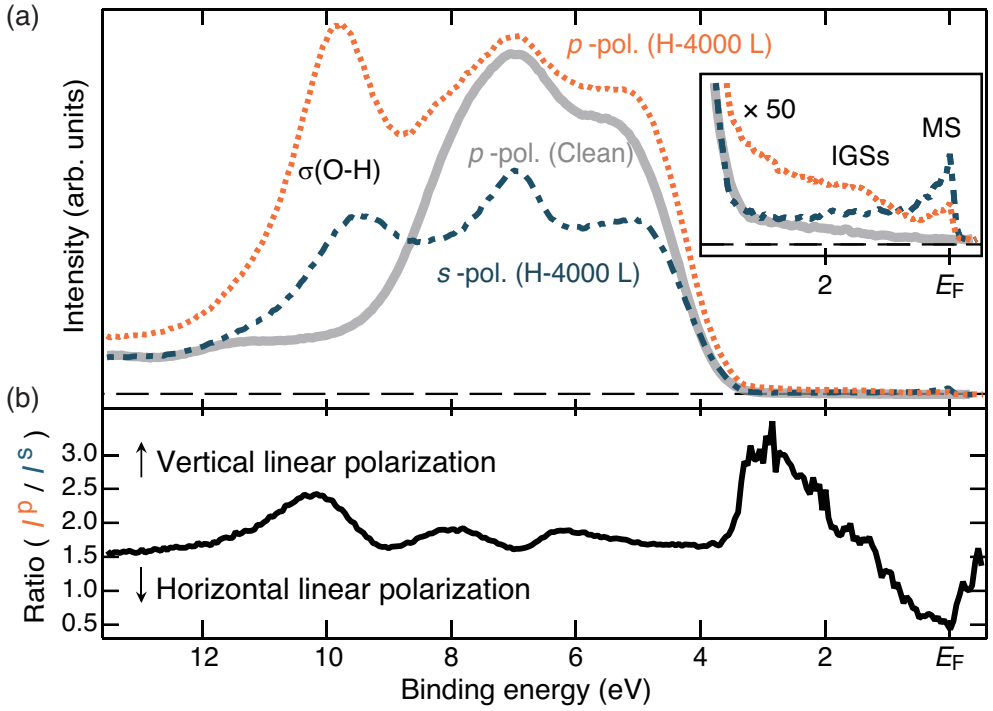

FIGURE 5.9: (a) Angle-integrated valence band spectra of the H-covered STO(001) surface measured at 80 K with p-polarized (orange dots) and s-polarized (blue dashed) light at $h\nu = 81$ eV. For comparisons, a spectrum of a clean STO(001) surface, taken at 300 K with p-polarized light, is shown (gray solid). The inset is magnified spectra near the Fermi level (E_F). (b) Intensity ratio of the H/STO spectra taken with p-polarized (I^p) and s-polarized (I^s) light.

on the STO surface, there emerges a MS with a spectral tail at the Fermi level and the IGS at $E_B \sim 1.3$ eV. The spectral change indicates surface metallization, as described in Sec. 5.3. Also, a peak appears at $E_B \sim$10 eV by hydrogen adsorption. By annealing the H-dosed STO under oxygen gas, these peaks disappear and the peak positions of the core-level spectra shift back to the original values on the clean surface.

In Fig. 5.9(b), the photoemission intensity ratio, I^p/I^s, of the H/STO spectra taken with the different polarized light is plotted. In the present measurement configuration, shown in Fig. 5.8, $I^p/I^s \sim 2$ means that the electronic state is isotropic with respect to the out-of-plane and in-plane directions. The intensity ratio of both the MS peak and the spectral tail exhibit the in-plane character ($I^p/I^s < 1$). Thus, these spectral features have the same origin and can naturally be assigned to coherent and incoherent parts of A_{spectral} in Eq. (5.1). The clear appearance of the spectral tail, or the incoherent part, indicates strong electron correlations in the MS [19, 91]. The MS band is likely assigned to the bulk conduction band of the Ti 3d t_{2g} orbitals that are partially

filled with electrons at the H/STO surface [64]. The in-plane character of the MS band indicates that the Ti 3d t_{2g} band has the x- or y-component. On the other hand, the IGS peak seems isotropic and it is expected to have a different origin from the MS band as discussed below. The peak at $E_{\rm B} \sim 10$ eV, which appeared after the hydrogen dosage, is assigned to the σ(O-H) state [92]. The assignment is consistent with the change of the O 1s core-level peak, as will be described in Fig. 5.12. Enhancement of the photoemission intensity at 10.5 eV by the p-polarized light ($I^p/I^s > 2$) indicates that the O-H bond is along the surface normal direction. According to the previous photoemission study on a dissociated H_2O on STO(001), the energy separation between σ(O-H) and π(O-H) states is 3.6 eV [92]. Thus, a small dip at $E_{\rm B} \sim 7$ eV in Fig. 5.9(b) may be assigned to the π(O-H) state having the in-plane character. Intensity ratio of the dip ($I^p/I^s \sim 1.5$) is larger than the calculated ratio for the in-plane character ($I^p/I^s \sim 0.55$). This can be explained by the overlap of the isotropic O 2p states and the π(O-H) states at $E_{\rm B} \sim 7$ eV. It should be noted that adsorption of the hydrogen atoms on the oxygen sites has been predicted by the *ab initio* calculation [84].

Around $E_{\rm B} \sim 3$ eV, one notices that the I^p background intensity becomes large after the hydrogen adsorption and I^p/I^s becomes greater than 2, although there is no notable peak in the spectra [the inset of Fig. 5.9(a)]. The properties are similar to those of the surface photoemission (SP) effect [37, 38, 112], which is neglected in the approximation of Eq. (5.2). Since SP is caused by the change of A_z by the difference of the permittivity between the vacuum and the sample surface, this emission is considered to be observable only by p-polarized light. Thus, the spectral feature may tentatively be assigned to the SP channel, however, further discussion is beyond the scope of the present chapter.

5.4.4 Metallic states

Figure 5.10(a) and (b) shows ARPES data around Γ(003) taken with (a) p-polarized and (b) s-polarized light with an angular mode of the analyzer. As described in the previous section, the MS has the in-plane character and, thus, it appears much clearer in the s-polarization geometry, Fig. 5.10(b), than in the p-polarization case, Fig. 5.10(a). In both angle-resolved spectra in Fig. 5.10, the obvious MS peaks are identified at $k_x \sim 0.5$ nm^{-1} and $k_x \sim 1.5$ nm^{-1} for p- and s-polarized light, respectively, while the intensities become significantly weaken at $k_x = 0$ nm^{-1}. The sharp intensity variation depending on k_x can be understood by symmetry arguments of the Ti 3d t_{2g} orbitals that contribute to the metallic band. To see the precise structure of the metallic band,

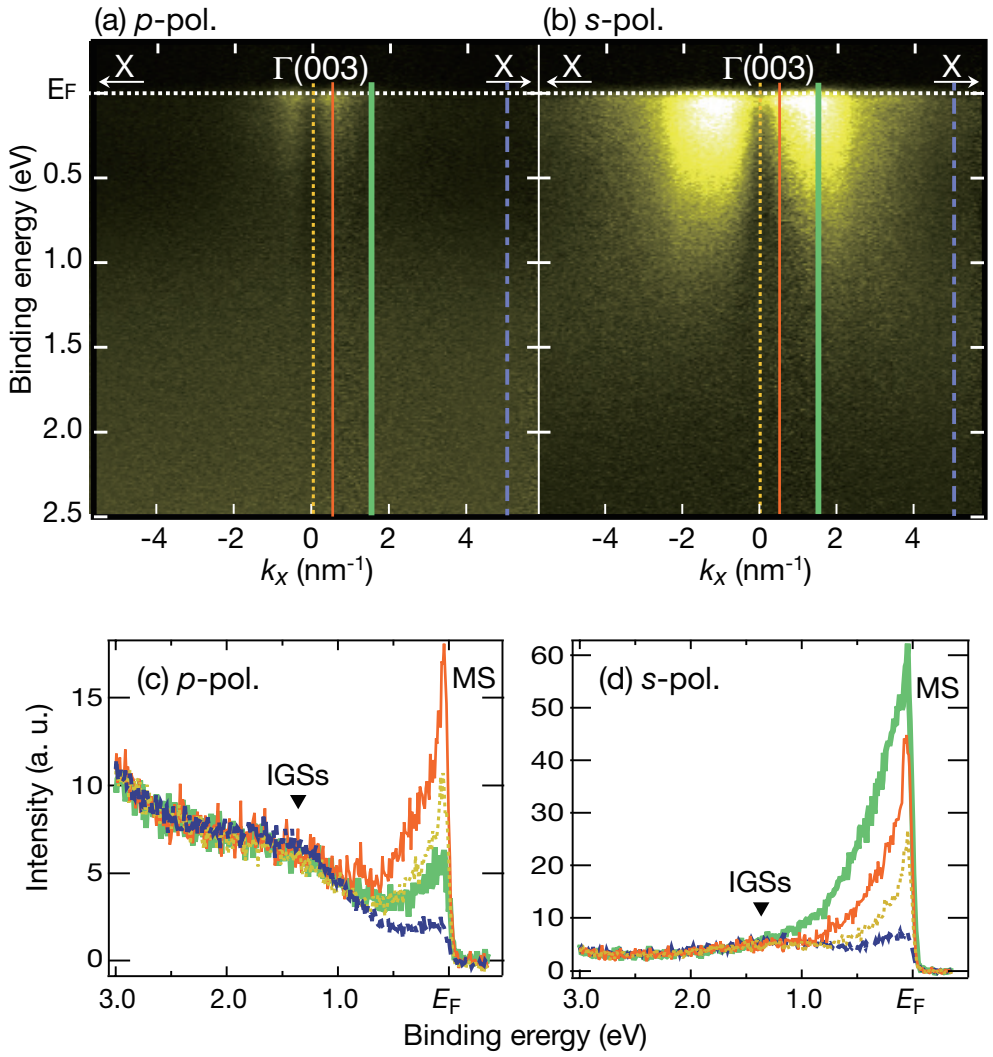

FIGURE 5.10: Photoemission intensity map of the 4000 L H-dosed STO(001) along the k_x direction. The data were taken at 80 K using p-polarized (a) and s-polarized (b) light at $h\nu = 81$ eV. The same color scales against the intensities are applied for both spectra. The energy distribution curves (EDCs) at $k_x = 0.0$, 0.5, 1.5, and 5.0 nm^{-1} are listed in (c) and (d), and their k_x positions are indicated on (a) and (b) as vertical lines. The characteristic humps are marked with black triangles. All spectra are normalized to the photon flux.

the enlarged ARPES spectra are examined. Figure 5.11 shows that the metallic band is composed of several branches. In the spectra measured with the p-polarized light [Fig. 5.11(a)], a single branch is observed at just below the Fermi level ($E_{\rm B} < 60$ meV) in a narrow k_x region. For the s-polarization in Fig. 5.11(b), three branches are observable: one is located at $E_{\rm B} < 60$ meV in a relatively wide k_x region, the second one shows rather large energy dispersion at $E_{\rm B} < 120$ meV, and the third one also has large dispersion but is located at deeper energies ($E_{\rm B} \sim 200$ meV).

Relation between the symmetry of the Ti 3d t_{2g} orbitals (d_{xy}, d_{xz}, and d_{yz}) and the measurement geometry is summarized in Table 5.1. Since only d_{xz} in Ti 3d t_{2g} can be observed with p-polarized light ($A_x + A_z$) in our experimental geometry, the dispersive feature in Fig. 5.11(a) is assigned to the d_{xz} band. The drop of the photoemission intensity from the d_{xz} band at Γ(003) in Fig. 5.10[(a), (c)] and Fig. 5.11[(a), (c)] is understood from the existence of the yz mirror plane at the normal emission geometry, where emissions from d_{xz} by A_z disappear and emissions by A_x are obtained. Similarly, d_{xy} and d_{yz} in Ti 3d t_{2g} can be observed with s-polarized light (A_y). A peak observed at Γ(003) can emerge from the d_{yz} orbital. Thus, a rather flat band at $E_{\rm B} < 60$ meV in Fig. 5.11(b) is attributed to the d_{yz} band. On the other hand, a significant drop of the intensities of the bands at $E_{\rm B} < 120$ meV and $E_{\rm B} \sim 200$ meV indicates that they have the d_{xy} symmetry.

TABLE 5.1: List of s, p, and d orbitals which have non-zero matrix elements against the vector potentials listed on the left, and have final states with even parities in the mirror planes at the top. The parities of orbitals with respect to the mirror plane is written inside the parenthesis. It is noted that, in the present measurement geometry, p-polarized light excites electronic states in the A_x and A_z rows, while s-polarized light in the A_y row.

	xz mirror plane	yz mirror plane	normal emission
A_x	s, p_x, d_{xz} $_{(even)}$	p_x, d_{xy}, d_{xz} $_{(odd)}$	p_x, d_{xz}
A_y	p_y, d_{xy}, d_{yz} $_{(odd)}$	s, p_y, d_{yz} $_{(even)}$	p_y, d_{yz}
A_z	s, p_z, d_{xz} $_{(even)}$	s, p_z, d_{yz} $_{(even)}$	s, p_z

Based on these symmetry arguments, the dispersion curves of the metallic Ti 3d bands are summarized in Fig. 5.11(c) and (d). The Ti 3d_{xz} and 3d_{yz} bands have the band bottom at $E_{\rm B} = 60 \pm 15$ meV and effective mass of $m_x^* \sim 1.8$ m_e and $m_x^* \sim 22$ m_e, respectively, along the k_x direction. Although the spectral tail of the MS peak prevents from the accurate determination of the Ti 3d_{xy} band dispersion curve, it may have the band bottom at $E_{\rm B} \sim 120$ meV with $m_x^* \sim 1.5$ m_e as judged from the

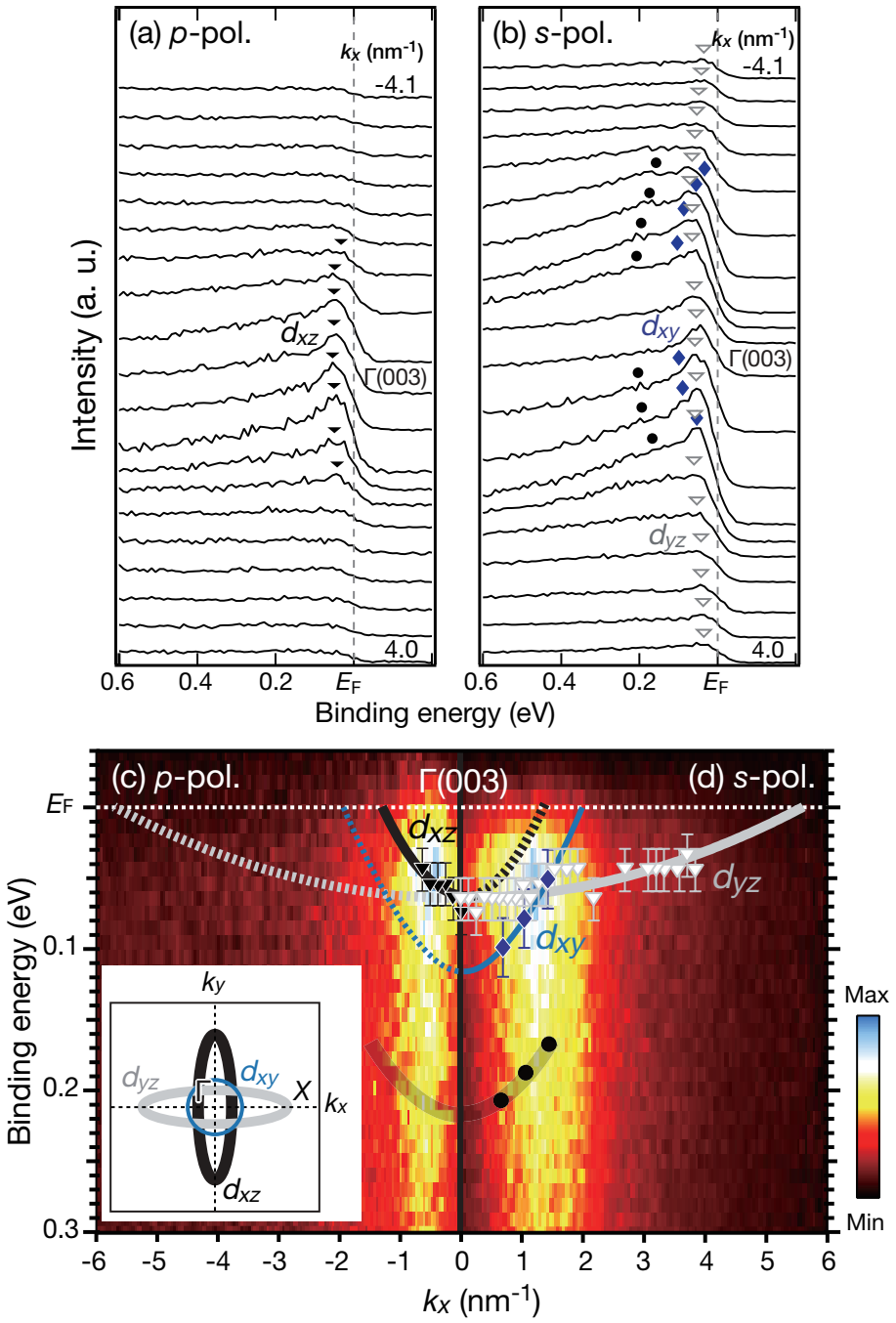

FIGURE 5.11: Summary of the subbands for the metallic states at Γ(003) for the 4000 L H-dosed sample ($T = 80$ K, $\theta = 0°$, $h\nu = 81$ eV). (a) and (b) are EDC's along the k_x direction with the integration of about 0.4 nm^{-1}.(c) and (d) are ARPES intensity data taken with p-polarization and s-polarization respectively. The peak positions of d_{xz} (black triangle), d_{yz} (gray triangle), d_{xy} (blue diamond), and hump structure (black circle) are indicated. The inset shows a schematic picture of the Fermi surfaces in the surface Brillouin zone.

spectral feature in Fig. 5.11(b). The obtained effective mass of the d_{xy} band differs from that obtained in the previous section due to the experimental resolution of the ARPES systems and the suppression of the PES intensities around $k_x = 0$ nm^{-1} due to the different experimental geometry. The intensities of the hump states at $E_{\rm B} \sim 200$ meV become small at $|k_x| > 2$ nm^{-1}, where the edges of the dispersion curve of the d_{xy} band cross the Fermi level. Thus, the hump states at $E_{\rm B} \sim 200$ meV is likely to be assigned to the incoherent peak of the Ti $3d_{xy}$ band enhanced by the polaronic or plasmonic interactions [91, 93, 113]. The energy separation between the d_{xy} peaks at $E_{\rm B} < 120$ meV and incoherent peak at $E_{\rm B} \sim 200$ meV in Fig. 5.11(b) is close to the separation measured in a recent temperature dependent ARPES study on STO, into which electrons are induced by annealing the STO in the ultrahigh vacuum [91]. The presence of the d_{xy} band at higher binding energy than the d_{xz} and d_{yz} bands is also supported by the polarization dependence of the MS as observed in Fig. 5.9(b). The small intensity ratio of the MS ($I^p/I^s < 1$) precludes the case where the Ti $3d$ bands are triply degenerated and isotropic ($I^p/I^s \sim 2$). The d_{xy} band at higher binding energy would be less-influenced by the smearing-out effect of density of state near the Fermi level by the Fermi-Dirac distribution. This may also contribute to the small intensity ratio of the MS.

The energy separation of the d_{xy} band from the doubly degenerate d_{xz} and d_{yz} at $\Gamma(003)$ can be explained by the electron-confinement effect in the surface-vertical direction [20] and/or by the lowering of the crystal symmetry induced by the phase transition at the low temperature ($\lesssim 105$ K) [91, 114]. Theoretical calculations predict that the d_{xy} band should energetically be lifted up from the d_{xz} and d_{yz} band in STO with the low crystal symmetry [114], while the experimentally obserbed band structure [91] is opposite to the theoretical prediction. Band bending (~ 200 meV) by hydrogen adsorption on the STO surface [64] rather supports the electron-confinement model than the lowering-of-symmetry model. Based on the energy positions of the Ti $3d$ t_{2g} bands, the thickness of the confinement layer at the energy where electrons in the d_{xz} and d_{yz} states are confined is estimated to be 2.1 nm by a triangular-potential approximation[1]. The estimated thickness is close to the effective thickness of confined 2D electron systems on STO surfaces (1.4−5 nm) reported in previous studies [19, 20].

[1]To calculate the thickness of the confinement layer, the depth and the width of the triangular potential well are adjusted so as to reproduce the energy positions of the d_{xy} band and the doubly degenerated d_{xz} and d_{yz} bands at the Γ point. In addition the effective mass of $m_z^* = 1.8\ m_e$ for the d_{xz} and d_{yz} bands is applied. For details of the triangular potential well approximation, see J. H. Davies, *The Physics of Low − Dimensional Semiconductors : An Introduction* (Cambridge, New York, 1998).

5.4.5 In-gap states

Concerning the IGS at $E_B \sim 1.3$ eV, it shows no dependence on either incident light polarizations or k_x (emission angles). Since the IGS energetically locates between the Ti 3d and O 2p bands, it may have contributions from both the Ti 3d or O 2p states, or it may result from Ti 3d-O 2p hybridized states. Table 5.1 shows that emission from the p orbitals is independent of the mirror planes and is not weakened even for the normal emission. Thus, the IGS is mainly composed of the O 2p orbitals. The isotropic nature likely originates from the six O 2p-Ti 3d bonding coordination along the three different orthogonal axes. The origin of the IGS has been discussed based on various models: it has been attributed to a locally screened incoherent state of the Ti 3d-O 2p band [98], a precursor of the "lower-Hubbard band" of the d^1 insulator [115], chemical disorder [89], and the polaron effect [100]. Identification of the O 2p nature for the IGS on the well-defined surface rather favors the locally screening Ti 3d-O 2p band model [98].

5.4.6 2D electron density

From the band dispersion plots in Fig. 5.11, Fermi surfaces of the metallic H/STO surface are inferred as shown in the inset. The Ti 3d_{xz} and d_{yz} bands have oval Fermi surfaces with the long axes along the k_x and k_y directions, respectively, while the Ti 3d_{xy} band has an isotropic Fermi circle. Within the electron confinement model, the 2D electron density, n_{2D}, is estimated as $n_{2D} \approx 3.9 \times 10^{14}$ cm^{-2}, which corresponds to 0.54 electrons in a surface unit cell (1.52×10^{-15} cm^2). The value is similar to those of the partially filled Ti 3d band reported on the cleaved STO(001) surfaces [19, 20]. In our previous report [64], the n_{2D} on the H/STO surface prepared by the 1350 L H-dosed was estimated to be $n_{2D} \approx 6 \times 10^{13}$ cm^{-2} at 20 K based on the assumption of a single metallic band. The three subband structures revealed in this study re-evaluate n_{2D} on the 1350 L H-dosed STO surface to be $n_{2D} \approx 3.1 \times 10^{14}$ cm^{-2}.

5.4.7 Core-level analysis

To study the adsorption site of the hydrogen atoms and to evaluate the ratio between numbers of electrons occupying the Ti 3d t_{2g} bands and the adsorbed hydrogen atoms, core-level photoemission measurements were carried out on the clean and hydrogen adsorbed STO(001) surfaces (Fig. 5.12). The multiple doublets and shoulders on the high

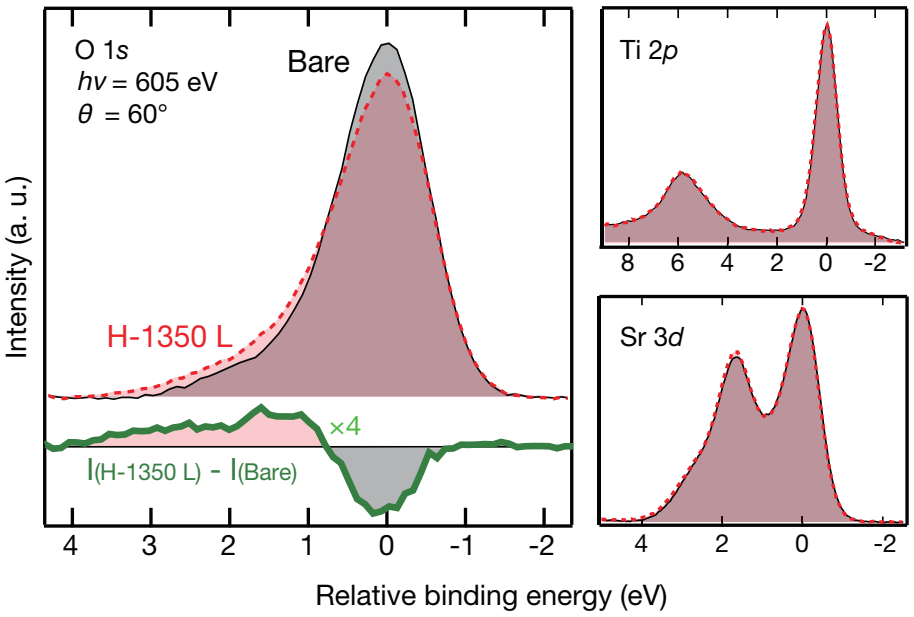

FIGURE 5.12: Core-level spectra of the clean (black solid) and 1350 L H-dosed STO surfaces (red dots) taken at $h\nu = 605$ eV and $\theta = 60°$. All the spectra were taken with p-polarization at 300 K. In order to evaluate the changes in the line shape of the spectra, all the peak shifts caused by hydrogen adsorption were calibrated, and the intensities were normalized to their peak areas. The difference plot (green solid) shows the increase of the shoulder on the higher binding energy side of the O 1s peak.

binding energy side of the O 1s and Sr 3d spectra were observed on the clean STO(001) surface, indicating the segregation of Sr oxides on the TiO_2 terminated surface [97, 116]. By 1350 L-hydrogen dosage, the core-level peak of O 1s shows a discernible variation, while those of Ti 2p and Sr 3d show negligibly small changes. These results show that metallization is induced by hydrogen adsorption on the oxygen site, and segregated Sr atoms on the surface do not play an important role in metallization. In the O 1s spectra, the main peak intensity decreases and, at the same time, a spectral shoulder is enhanced at ~ 1.5 eV a higher binding energy than the main peak. Since the emission from the O-H species on oxide surfaces usually appears at ~ 1.5 eV higher binding energy than that from oxygen in bulk oxide, the shoulder structure is attributed to O-H [94, 117, 118]. The area of the O-H feature corresponds to about 5.1 % of the total area of the O 1s peak. The hydrogen coverage can be quantitatively evaluated from the photoemission intensity through the following equation [119, 120]:

$$I = C \sum_{j=1}^{\infty} N_j \cdot \exp\left(-\frac{t_j}{\lambda \cdot \cos\theta}\right). \tag{5.3}$$

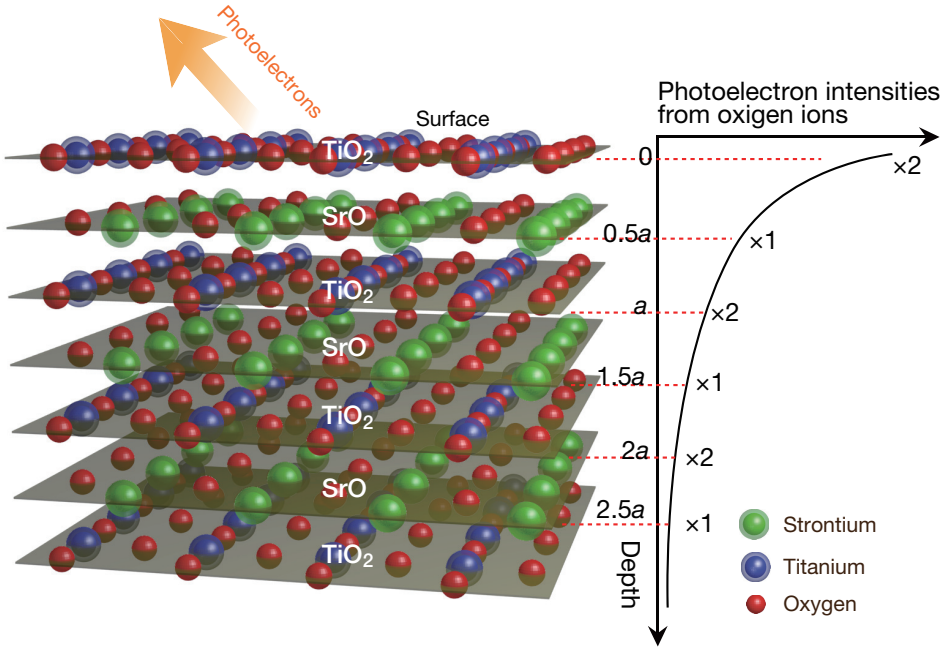

FIGURE 5.13: Illustration of a layered structure of the $SrTiO_3$ crystal near the surface. The photoelectron intensities from each oxygen atoms located on corresponding layers are illustrated on the right hand side.

The constant C depends on the spectrometer efficiency, asymmetry parameter, photon flux, and photo-ionization cross section. N_j and t_j are the atomic density and the depth of the jth layer from the surface, respectively. The peak intensity I is the sum of photoelectrons from the oxygen atoms located over the layers. The layered structure illustrated in Fig. 5.13 is used for the estimation. The inelastic mean-free path (λ) is $\lambda = 0.575$ nm as estimated from the empirical formulation by Tanuma, Penn, and Powell (TPP-2M) [121]. Under the assumption that the hydrogen atoms adsorb only on oxygen atoms in the topmost TiO_2 layer, the number of hydrogen atoms on the surface is evaluated to be $0.8-1.1 \times 10^{14}$ cm^{-2} (or 0.12−0.17 atoms par 2D unit cell) at 300 K. When one assumes that each hydrogen atom provides one electron to the STO surface, the 2D electron density is estimated as $n_{2D} \sim 1 \times 10^{14}$ cm^{-2}, which is the same order of magnitude as the 2D electron density estimated from the Fermi surface. The simple estimation thus indicates that there is a good correlation between the number of hydrogen atoms adsorbed on the surface and that of electrons doped into the unoccupied Ti 3d band.

5.5 Conclusion

In summary, through photoelectron spectroscopy and transport measurements on the $SrTiO_3$(001)-1 $\times$ 1 surface, we confirmed an insulator-to-metal transition induced by hydrogen adsorption. The surface metallization is due to electron doping into the conduction band, which shifts below the Fermi level with the appearance of a quantized state in the space charge layer. The value of the surface conductivity and derived mean free path show that the system is in the metallic conduction regime.

Details of the electronic structure of the metallic band on the hydrogen adsorbed STO(001) surface are revealed by the valence band and core-level photoelectron spectroscopy study with polarized light. With the symmetric arguments, the H-induced peaks in the valence-band region are attributed to σ(O-H) oriented along the out-of-plane direction, the metallic states mainly composed of the Ti 3d t_{2g} components, and the IGS mainly composed of O 2p orbitals. Furthermore, the state at 3 eV is also the H-induced one, which shows strong polarization dependence. The electrons at the MS partially fill in the Ti 3d_{xy} band and the doubly degenerate Ti 3d_{xz} and Ti 3d_{yz} bands. On the basis of the band bending effect by hydrogen adsorption on STO and the appearance of the incoherent peak for the MS, the realization of the two-dimensional electron liquid (2DEL) phase on the H/STO surface is suggested.

Chapter 6

High-resolution ARPES studies of $ZnO(10\bar{1}0)$ and $SrTiO_3(001)$ surfaces

Two-dimensional (2D) electronic structures of the $ZnO(10\bar{1}0)$ and $SrTiO_3(001)$ surfaces have been studied by high-resolution angle-resolved photoelectron spectroscopy (ARPES) measurements. Incoherent states at the bottom of the two- dimensional metallic states (MSs) have been observed for both surfaces. The two-dimensionality of the electronic states is confirmed. The band bending structures are calculated with the anisotropic effective-mass approximations (AEA) described in Chapter 4. We have concluded that the incoherent states originate from many-body effect where photoelectron excite phonons or plasmons.

6.1 Introduction

Hydrogen-induced metallization of ZnO surfaces have been observed by electrical conductivity and scanning tunneling microscope (STM) measurements [5, 9, 122, 123]. Recent ARPES measurements have revealed that two-dimensional electron gases (2DEGs) with parabolic band dispersions are induced at the $ZnO(10\bar{1}0)$ and $ZnO(000\bar{1})$ surfaces by hydrogen adsorption but not induced at the hydrogen-adsorbed Zn-polar ZnO(0001) surface [5, 10–12]. This is because hydrogen adsorbed on topmost oxygen atoms at $(10\bar{1}0)$ and $(000\bar{1})$ surfaces can be electron donors to the ZnO surfaces. The effective

masses of $0.16\pm0.05\ m_e$, where m_e is the mass of a free electron, for a H/ZnO($10\bar{1}0$) surface and $0.5\pm0.1\ m_e$ for a H/ZnO($000\bar{1}$) surface were observed by ARPES studies [12]. However, these effective masses differ from the value of $0.21-0.3\ m_e$, which have been experimentally obtained by infrared-reflectivity measurements and various cyclotron-resonance measurements [124]. One of the possible explanations for the discrepancies is that the spectral tails accompanying quasiparticle excitations in the photoemission processes prevent the accurate fittings of the dispersion of the 2DEGs. Therefore, high-resolution ARPES studies are needed to clarify the electronic structures and the origin of the quasiparticle excitations.

In addition to the 2DEG at the ZnO surfaces, recent ARPES studies have shown that 2DEG can be observed at cleaved and ultra-violet (UV) light-irradiated $SrTiO_3$(001) surfaces [19–21]. The ARPES spectra show that there exist long tails of ARPES intensities at the lower energy sides of the 2DEGs. Possible origins of the tails are the enhanced many body effect inherent in the 2DEG states [19]. As described in Chapter 5, we have found the creation of the 2DEG at the hydrogen-adsorbed $SrTiO_3$(001) surfaces, and also found that there exist the long tails of the ARPES intensities at the bottom of the 2DEG band. Since the tails take the Ti $3d$ t_{2g} like polarization dependencies, it is natural to think that these tails are originated from electrons in the Ti $3d$ t_{2g} bands.

In this Chapter, the high-resolution ARPES results of the 2DEG observed at the hydrogen-adsorbed $SrTiO_3$(001) and ZnO($10\bar{1}0$) surfaces are shown. The metallic states are originated mainly from electrons in the symmetric Zn $4s$ band for the ZnO($10\bar{1}0$) surface and electrons in the asymmetric Ti $3d$ t_{2g} bands for the $SrTiO_3$(001) surface. The 2DEGs have shown much different characters. However, the ARPES measurements show that spectral tails are observed at the both $SrTiO_3$(001) and ZnO($10\bar{1}0$) surfaces. We concluded that the tails originated from many-body interactions of the photoemission process of the ARPES measurements. The electronic and band bending structures of the semiconductors are studied by solving the Poisson-Schrödinger equations described in Chapter 4.

6.2 Experimental

ARPES experiments of ZnO($10\bar{1}0$) and $SrTiO_3$(001) surfaces were conducted at the beamline BL-1 of HiSOR [125, 126] and at the beamline BL-28 of Photon Factory,

respectively. The ionized bulk electron donor densities of both the semiconductor were obtained by Hall measurements[1].

6.2.1 ARPES measurements of the ZnO($10\bar{1}0$) surface

The ARPES experiments on ZnO were performed at the linear-undulator beamline (BL-1) of a compact electron-storage ring (HiSOR) at Hiroshima University [125, 126], using an ARPES system in which the electron analyzer can be rotated around linearly polarized undulator radiation [127]. The vector potential ($\boldsymbol{A}$) of the excitation light was switched between parallel (p polarization) and perpendicular (s polarization) to a plane spanned by the surface normal and photoelectron propagation vectors, as shown in Fig. 6.1(a). High-resolution ARPES measurements were performed using the angular mode of a hemispherical electron energy analyzer (R4000, VG-Scienta).

A hydrothermally grown ZnO($10\bar{1}0$) wafer was commercially purchased from Goodwill, Russia. Single crystal ZnO samples with a ($10\bar{1}0$) orientation were cleaned *in situ* by a well-established procedure [128]. H_2 molecules were cracked by a hot tungsten filament and 2000 L (1 L = 1.3×10^{-4} Pa s) of atomic hydrogens were dosed on the ZnO($10\bar{1}0$) surface at room temperature. An ordered surface and negligible carbon contaminations were ascertained by a sharp 1×1 pattern of low-energy electron diffraction (LEED) and auger electron spectroscopy (AES) spectra, respectively. All the ARPES measurements of the ZnO surface were performed at 13 K in the UHV chamber (below 1×10^{-8} Pa) with the total energy resolution of 25 meV.

A schematic drawing of the ARPES measurement system for ZnO($10\bar{1}0$) surface is shown in Fig. 6.1(a). The sample was set so that the [0001] and [$10\bar{1}0$] axes are in the plane of the incident synchrotron radiation (SR) light and analyzer slit (electron detection plane). The x, y, and z axes are set parallel to the [0001], [$11\bar{2}0$], and [$10\bar{1}0$] directions of the ZnO crystal, respectively. A Fermi surface map was obtained by φ rotation of the sample about the x axis.

6.2.2 ARPES measurements of the $SrTiO_3$(001) surface

ARPES experiments of $SrTiO_3$ were performed at the undulator beamline BL-28A of Photon Factory, High Energy Accelerator Research Organization (KEK). The measurements were performed with a hemispherical electron-energy analyzer (SES-2002,

[1]See the footnote in Sec. 4.3.

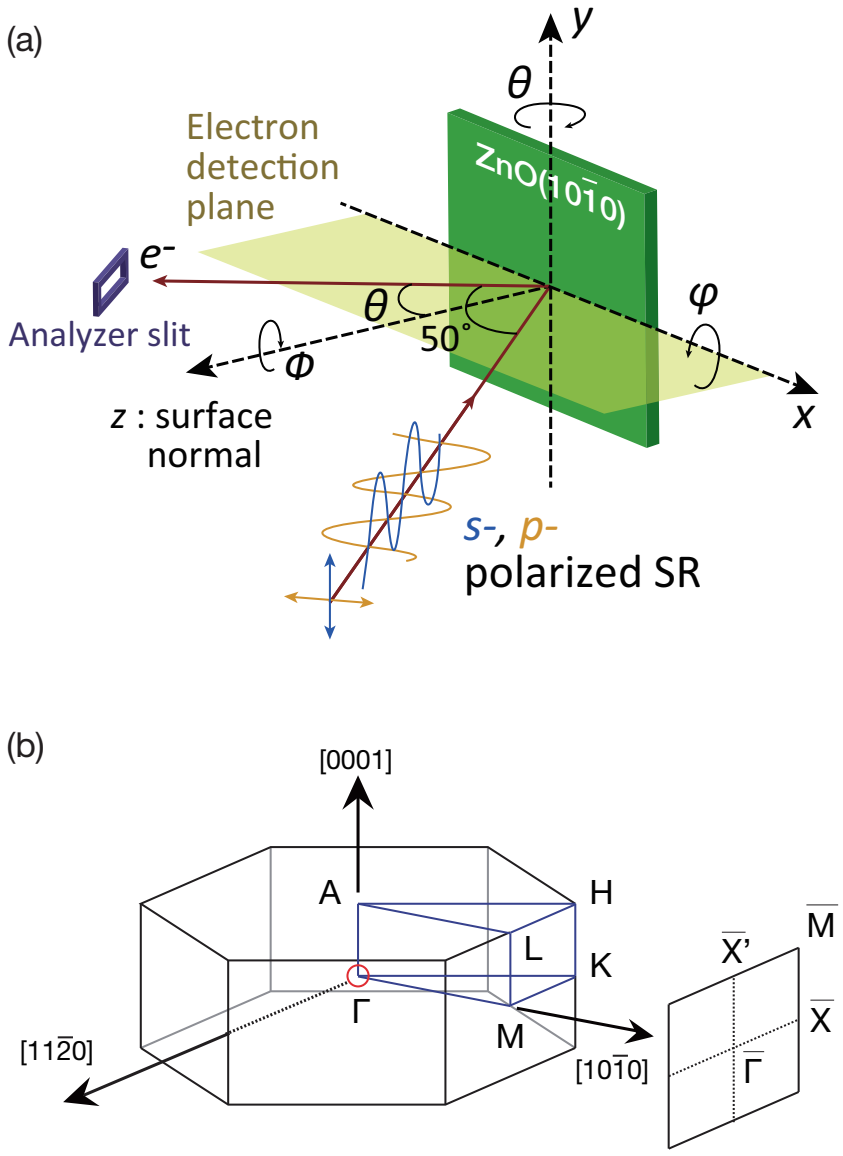

FIGURE 6.1: Schematic picture of the ARPES measurement system for the ZnO(10$\bar{1}$0) surface. (a) The x, y, and z axes are set parallel to the [0001], [11$\bar{2}$0], and [10$\bar{1}$0] directions of the ZnO crystal, respectively. Direction of the incident light and the analyzer slit are in the xz mirror plane (light green). The sum of the incidence angle α and the emission angle θ was fixed at 50°. (b) Schematic representation of the bulk Brillouin zones and the surface Brillouin zones in the [11$\bar{2}$0]-[10$\bar{1}$0] plane of the ZnO crystal.

VG-Scienta), and circularly and linearly polarized light were used with the total energy resolution of 25 meV. The ARPES measurements were performed at $T \sim 20$ K in an ultrahigh vacuum below 1×10^{-8} Pa.

In the present study, an n-type STO(001) wafer (0.05 wt% Nb-doped, Shinkosha Co. Ltd., Japan) was used as the sample. The sample was treated with buffered-HF solution to obtain the TiO_2-terminated surface [129]. After introducing the sample into the UHV chamber, the sample was annealed in the UHV at 1220 K for 60 min prior to the hydrogen adsorption 13000 L. Hydrogen molecules were cracked by a hot tungsten filament. It should be noted that no change of the half-transparent purple colored wafer was found by eyes between before and after the sample annealing and hydrogen adsorption procedures.

A schematic drawing of the ARPES measurement system of $SrTiO_3$ is shown in Fig. 6.2(a). The $SrTiO_3$ crystal was set so that the [100] and [001] axes are on the electron detection plane. The x, y, and z axes are set parallel to the [100], [010], and [001] directions of the STO crystal, respectively. The Fermi surface map was obtained by φ rotation of the sample about the x axis.

6.3 Two-dimensional metallic states

Figure 6.3(b) shows the spectra integrated around $\bar{\Gamma}_0$ of the ZnO($10\bar{1}0$) surface Brillouin zone with $h\nu = 48$, 65, and 81 eV. These photon energies correspond to electron excitations at the circles in the Brillouin zones shown in Fig. 6.3(a). All the spectra show clear metallic states near the Fermi level, indicating the k_z independencies of the metallic states. Therefore, the observed MS is two-dimensional. The same discussion can be applied to the metallic states observed at the $SrTiO_3$(001) surface. Figure 6.4(b) shows spectra integrated around $\bar{\Gamma}_{10}$ [Fig. 6.4(a)] with the photon energies of $h\nu = 53$, 63, 73, and 83 eV. These photon energies correspond to the electron excitations at the circles in the Brillouin zones shown in Fig. 6.4(a). Therefore, the metallic states observed at the $SrTiO_3$ surface are also two-dimensional.

The photon energy dependence of the photoelectron intensities can be explained by the transition probability of the photoexcitation process. As can be seen from Fig. 6.3(a), the sphere of the final-state free-electron with $h\nu = 65$ crosses $\bar{\Gamma}_{20\bar{2}0}$ of the bulk Brillouin zones of the ZnO crystal. Therefore, the excitation probabilities of electrons in the metallic states, which locate around each Γ points in the bulk Brillouin zones,

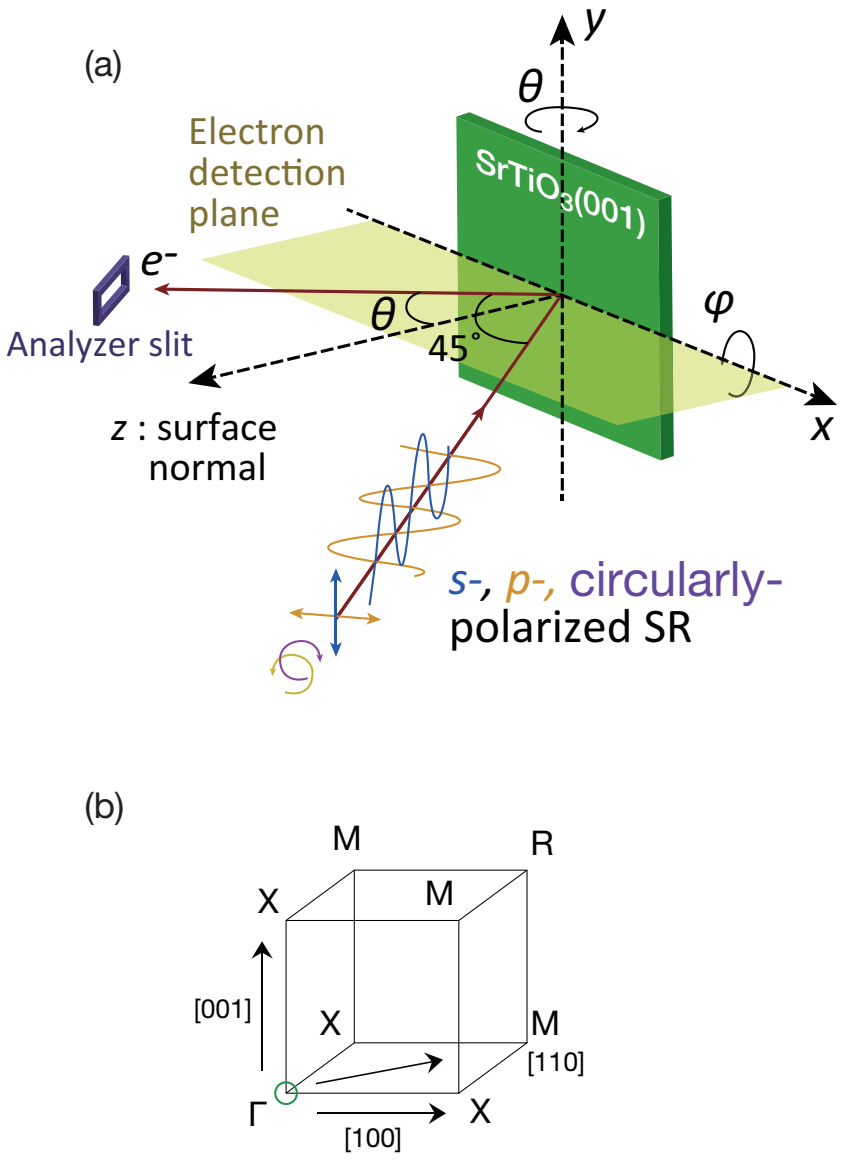

FIGURE 6.2: Schematic picture of the ARPES measurement system for the $SrTiO_3(001)$ surface. (a) The x, y, and z axes are set parallel to the [100], [010], and [001] directions of the $SrTiO_3$ crystal, respectively. Direction of the incident light and the analyzer slit are in the xz mirror plane (light green). The sum of the incidence angle α and the emission angle θ was fixed at 45°. (b) Schematic representation of the bulk Brillouin zone for the $SrTiO_3$ crystal.

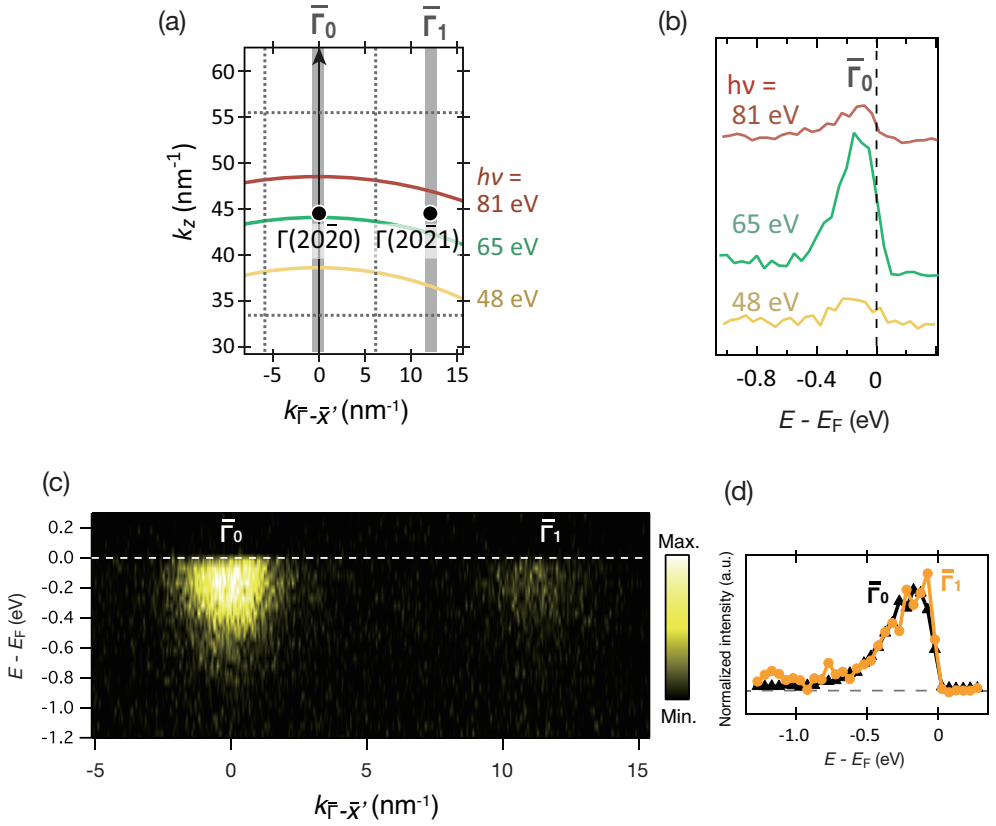

FIGURE 6.3: (a) Schematic representation of the Brillouin zones for the crystal in the [0001]-[10$\bar{1}$0] plane. Using an inner potential 9.8 eV measured from E_F [130], spheres of the final-state free-electron at $h\nu$ = 48, 65, and 81 eV are obtained. (b) The spectra integrated around $\bar{\Gamma}_0$ with the photon energy of $h\nu$ = 48, 65, and 81 eV shown in (a). (c) ARPES intensity map along the k_x direction taken at the ZnO(10$\bar{1}$0) surface. The data were taken at 13 K using p-polarized light at $h\nu$ = 65 eV. (d) The spectra shown in (c) are integrated aound $\bar{\Gamma}_0$ and $\bar{\Gamma}_1$. The intensities are normalized by the peak heights.

are large with $h\nu = 65$ eV. The effects of the cross section of the photoemission process can also be observed in the ARPES intensity map shown in Fig. 6.3(c), which was taken at $h\nu = 65$ eV along the k_x direction. The ARPES intensities of MS at $\bar{\Gamma}_0$ are stronger than the intensities of MS at $\bar{\Gamma}_1$. This is because the sphere of the final-state free-electron with $h\nu = 65$ eV does not cross the bulk Γ points in the Brillouin zones for the grazing emission angle [see Fig. 6.3(a)].

An ARPES intensity map shown in Fig. 6.4(c) was taken at $h\nu = 81$ eV along the k_x direction. The intensities are normalized to the background intensity above the Fermi level. Even though the spheres of the final-state free-electron cross Γ_{003} of the bulk Brillouin zones [Fig. 6.4(a)], the ARPES intensities around $\bar{\Gamma}_{00}$ (the normal emission) are very weak. This is because the 2DEG of $SrTiO_3$ is originated mainly from

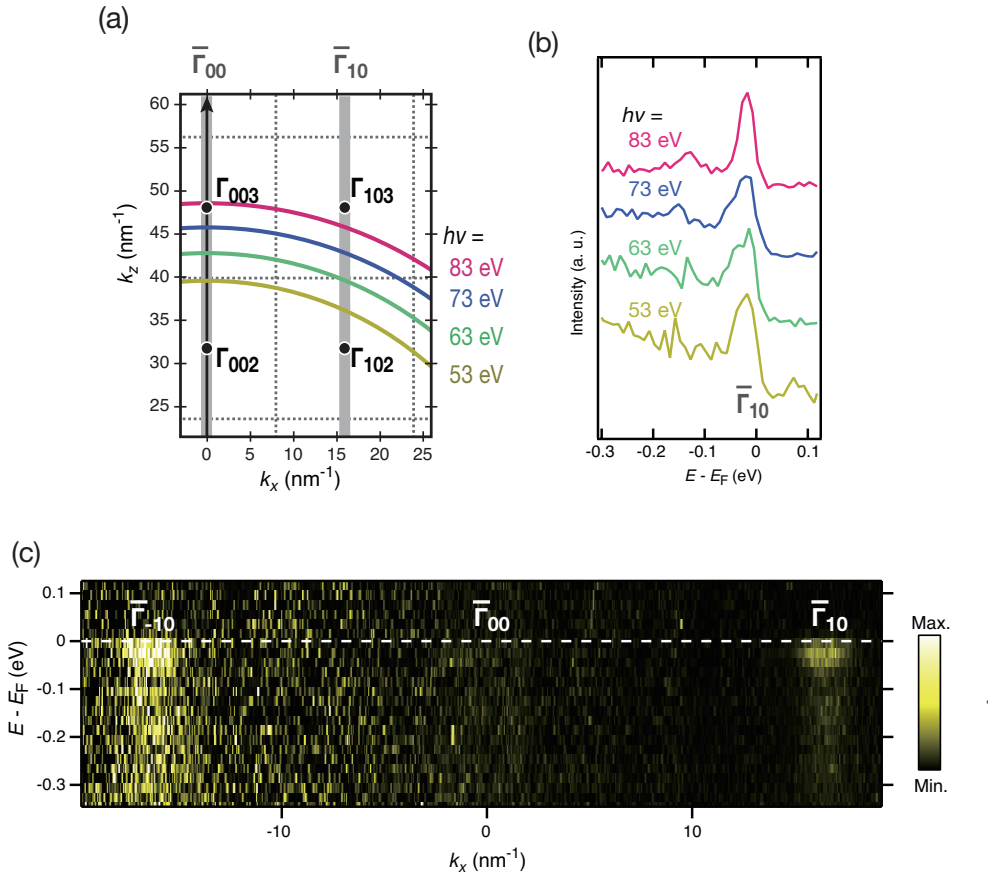

FIGURE 6.4: (a) Schematic representation of the Brillouin zones for the $SrTiO_3$ crystal in the [100]-[001] plane. Using an inner potential 12 eV measured from E_F [90], spheres of the final-state free-electron at $h\nu$ = 53, 63, 73, and 83 eV are obtained. (b) The spectra integrated around $\bar{\Gamma}_{10}$ with the photon energy of $h\nu$ = 53, 63, 73, and 83 eV. (c) ARPES intensity map along the k_x direction taken at the $SrTiO_3$(001) surface. The data were taken using circularly-polarized light at $h\nu$ = 81 eV at $T \sim 20$ K. The intensity map is normalized to the background intensities for all angles.

electrons in the d_{xy} orbitals, and the high-symmetry of the normal emission weakened the photoexcitation probabilities at the yz mirror plane (see Chapter 5). The metallic peaks are compared at $\bar{\Gamma}_0$ and $\bar{\Gamma}_1$ for the ZnO(10$\bar{1}$0) surfaces and show no difference within the experimental resolution [Fig. 6.3(d)]. The ARPES measurements were mainly made at $\bar{\Gamma}_0$ for the ZnO(10$\bar{1}$0) surface and at $\bar{\Gamma}_{10}$ for the $SrTiO_3$(001) surface to obtain strong ARPES intensities.

6.4 Coherent states and incoherent states

High-resolution ARPES intensity maps for the ZnO($10\bar{1}0$) and $SrTiO_3$(001) surfaces are displayed in Fig. 6.5(a) and (d). Both the ARPES intensity maps show non-vanishing spectral weight on the lower energy sides of the MSs. This weight is enhanced by many-body effects of the photoemission processes [19] and can be expressed by the incoherent part of the spectral function (see Section 3.1.3). The energy distribution curves (EDCs) of the $SrTiO_3$(001) surface [Fig. 6.5(e)] show broad dispersion-less states around -1.0 eV. The polarization dependent studies indicate that the origin might be localized O $2p$ states hybridized with Ti $3d$ states (see Chapter 5). It is of interest that the MS peak/incoherent state peak ratio is much larger at the ZnO surface than at the $SrTiO_3$ surface. At the ZnO surface, the sharp metallic states and weak dip-hump structure observed for the $SrTiO_3$ surface are indistinguishable and a large hump of incoherent structures are observed.

Both of the Fermi surface maps show circle-shaped structures centered at $k_x \sim 0$ nm^{-1} for ZnO and at $k_x \sim 16$ nm^{-1} $SrTiO_3$ surfaces. The Brillouin zones of the ZnO surface are rectangle-shaped [Fig. 6.5(f)]. However, the Fermi surface map indicates metallic states which take isotropic circle-shaped electronic structures within the experimental resolution. From the symmetry argument (Chapter. 4), the MSs observed in these ARPES maps are subbands for Zn $4s$ of ZnO and of Ti $3d_{xy}$ for STO.

In order to obtain the structures of MSs, ARPES intensities in Fig. 6.5(a) and (d) are divided by the Fermi-Dirac distribution functions convoluted with Gaussian functions [Fig. 6.6(a),(c)]. Additionally, the curvature methods developed by P. Zhang *et al.* [76] were employed to clarify the peak structures [Fig. 6.6(b),(d)]. By plotting the peak positions, we obtained the band structures of the metallic states with the effective mass of $m^* = 0.23\ m_e$ and the band minimum of -85 meV for the ZnO($10\bar{1}0$) surface and $m^* = 0.81\ m_e$ and the band minimum of -55 meV for the $SrTiO_3$(001) surface. Both of the obtained effective masses are in reasonable agreement with values reported in previous studies [23, 124]. It should be noted that the effective mass at the $SrTiO_3$(001) surface obtained in this chapter differs from that obtained in Chapter 5 due to the poor experimental resolution and the weak PES intensities at the normal emission in Chapter 5.

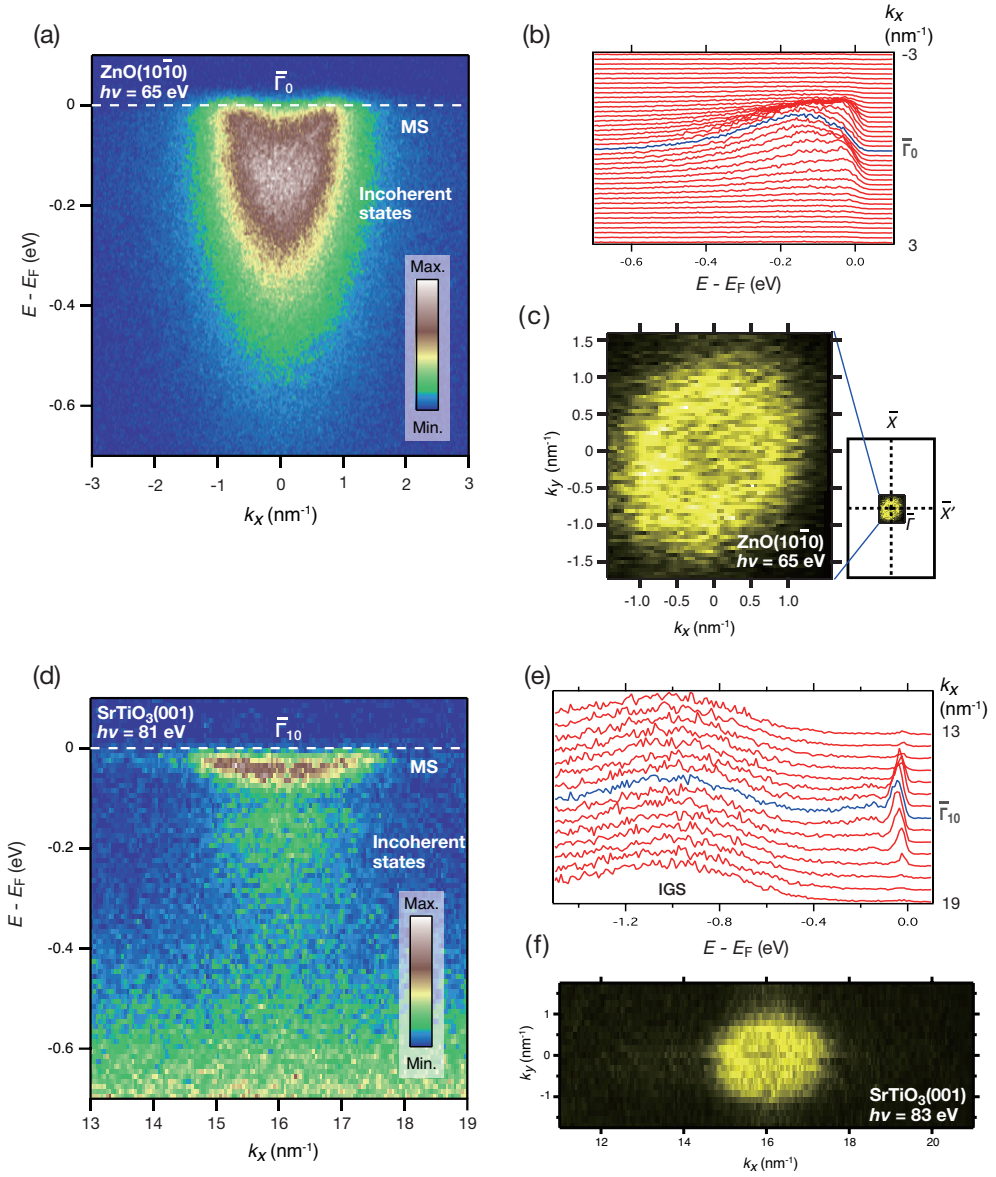

FIGURE 6.5: ARPES intensity maps [(a),(d)] and the corresponding EDCs [(b),(e)] for the ZnO(10$\bar{1}$0) surface [(a),(b)] taken with $h\nu = 65$ eV and for the $SrTiO_3$(001) surface [(d),(e)] taken with $h\nu = 81$ eV. The peak positions of the MSs and incoherent states located on the lower energy side of the MSs are indicated in (a) and (d). The in-gap-states (IGS) located around -1.0 eV is indicated in (e). The EDCs at $\bar{\Gamma}_0$ and $\bar{\Gamma}_{01}$ are shown by blue curves in (b) and (e), respectively. The Fermi surface maps for the ZnO(10$\bar{1}$0) surface (c) with $h\nu = 65$ eV and for the $SrTiO_3$(001) surface (f) taken with $h\nu = 83$ eV. The surface Brillouin zones are also depicted in (c).

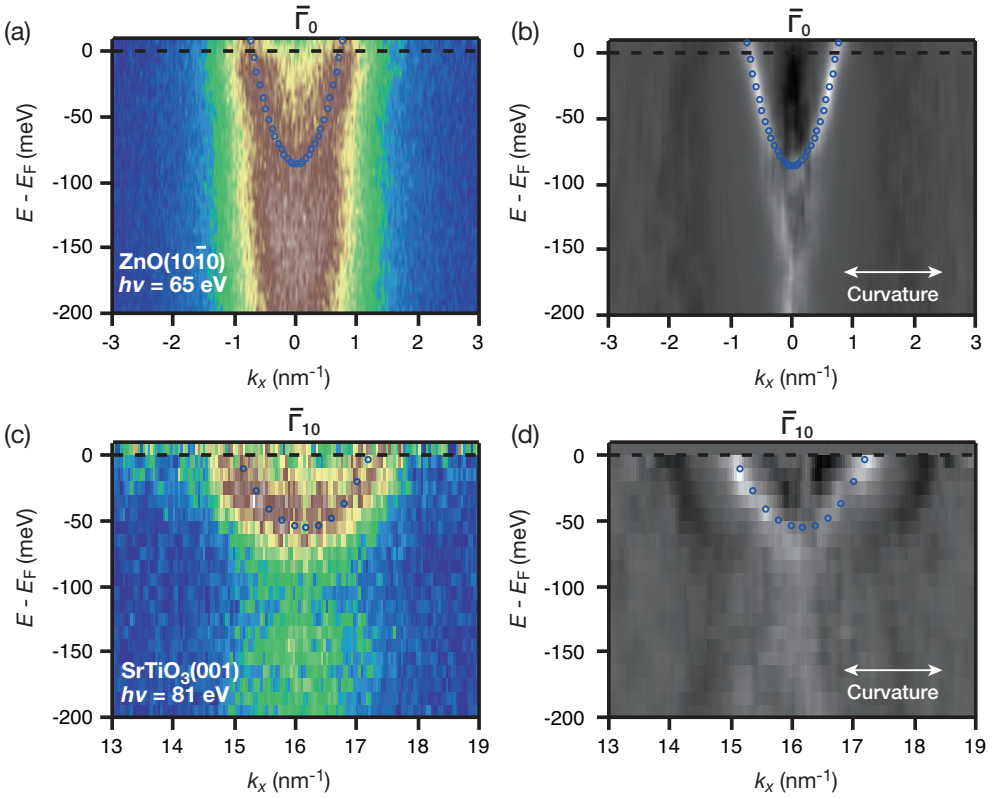

FIGURE 6.6: (a), (c) The ARPES intensity maps of ZnO(10$\bar{1}$0) surface [Fig. 6.5(a)] and $SrTiO_3$(001) surface [Fig. 6.5(d)], respectively, divided by the Fermi-Dirac distribution function convoluted with Gaussian functions. (b), (d) The corresponding curvature intensity plots of (a) and (c), respectively. The blue circles in the images indicate the plotted peak positions.

6.5 Band-bending and subband structures

The subband structure and band bending were calculated with the experimentally obtained effective masses and subband minima given above. The Poisson-Schrödinger equations were numerically calculated with the anisotropic effective-mass approximations (AEA) described in Chapter 4. The isotropic effective mass of 0.23 m_e was used for the ZnO(10$\bar{1}$0). For the calculation of the $SrTiO_3$(001) surface, the anisotropic effective masses listed in Table 6.1 were used. Here, the small effective masses of 0.81 m_e were obtained by the fitted result for the metallic states shown in Fig. 6.6(c) and (d), and the large effective masses of 17 m_e are obtained from the references [20, 23]. Bulk donor densities of $N_D = 1 \times 10^{14}$ cm^{-3} for the ZnO crystal and $N_D = 5 \times 10^{18}$ cm^{-3} for the $SrTiO_3$ crystal were used for the calculations, both of which have been obtained by Hall measurements. The relative dielectric constant of 7.88 [67] was used for the ZnO crystal. The field dependent dielectric constant with the values $\mathbb{E}_c = 470$

TABLE 6.1: Effective masses of the $SrTiO_3$ Ti $3d$ bands of the d_{xy}, d_{yz} and d_{xz} orbital origin in units of m_e [20, 23].

	m_x	m_y	m_z
d_{xy}	0.81	0.81	17
d_{yz}	17	0.81	0.81
d_{xz}	0.81	17	0.81

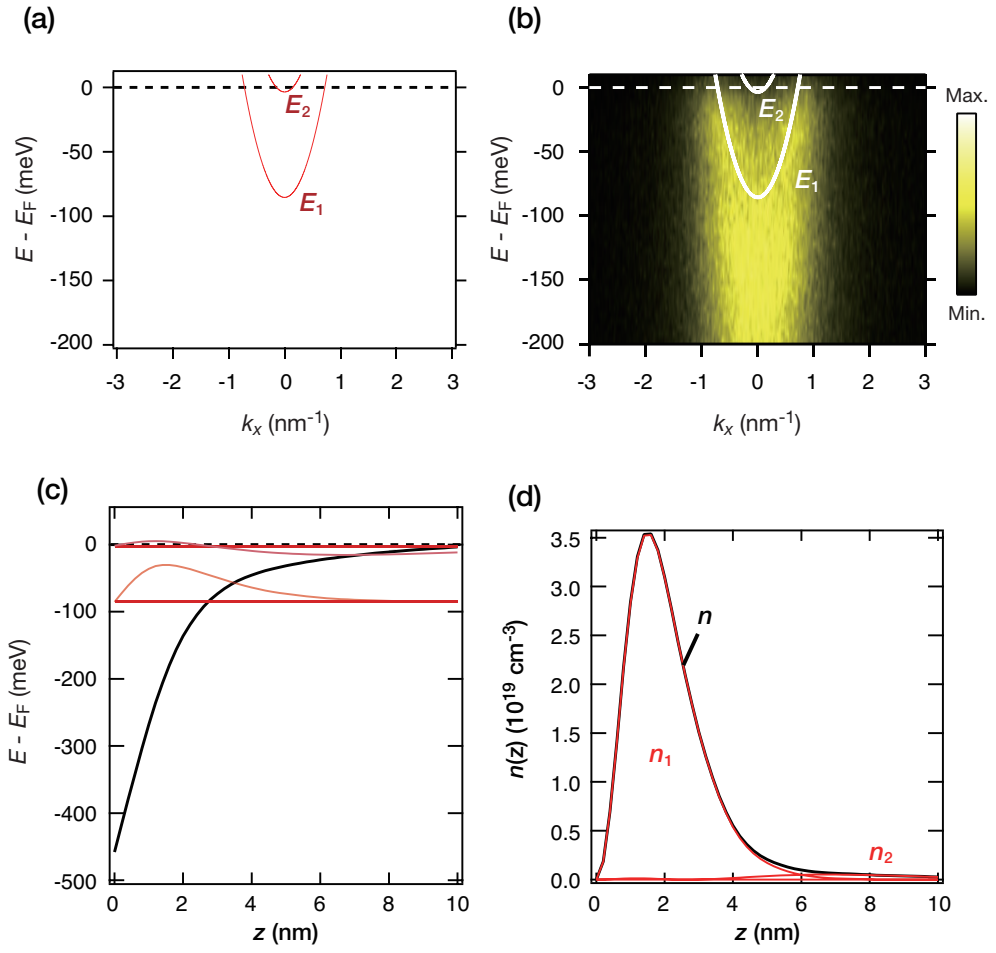

FIGURE 6.7: Calculated subband dispersions (a), potential variations (c), and partial electron densities (d) for the ZnO(10$\bar{1}$0) surface. The calculated subbands are displayed on a ARPES result in (b) for a comparison. The energies of subband minima and the wavefunctions of the confined electrons are displayed in (c).

kVm^{-1} and $\epsilon^0 = 15000$ at $T \sim 20$ K in Eq. (4.12) were used in the calculations for the $SrTiO_3$ crystal [72, 75].

The calculated band structures for the ZnO(10$\bar{1}$0) surface are shown in Fig. 6.7 and their parameters are listed in Table 6.2. The calculated band structures for the

TABLE 6.2: Energies for the subband minima and the surface carrier densities calculated for the ZnO($10\bar{1}0$) surface using the AEA model.

V_s (eV)	$E^0_{s,1}$ (eV)	$E^0_{s,2}$ (eV)	N_{ss} (cm^{-2})
-0.458	-0.085	-0.034	8.6×10^{12}

TABLE 6.3: Energies for the subband minima and surface carrier density of the $SrTiO_3$(001) surface, calculated using the AEA model.

V_s (eV)	$E^0_{xy,1}$ (eV)	$E^0_{xy,2}$ (eV)	$E^0_{xy,3}$ (eV)	$E^0_{yz,1}$, $E^0_{xz,1}$ (eV)	N_{ss} (cm^{-2})
-0.094	-0.055	-0.034	-0.022	-0.016	3.9×10^{13}

$SrTiO_3$(001) surface are shown in Fig. 6.8 and their parameters are listed in Table 6.3. Both of the calculated results show that most of the 2D electrons are confined within 6 nm from the surfaces. Two subband minima are located below the Fermi level for the ZnO surface, while more than nine subband minima are located below the Fermi level for the STO surface. It should be noted that the only first subband with the energy $E_{xy,1}$ is observed in the ARPES measurements (Fig. 6.6). The electrons in the first subband is localized at $z < 1$ nm and the mean-free paths of the photoelectrons with the kinetic energy of ~ 75 eV is about $0.5-1$ nm (see Fig. 3.4) [39]. Therefore, electrons from the first subband dominate the photoelectrons (see Fig. 4.5).

6.6 Conclusion

The subband structures of the $SrTiO_3$(001) and ZnO($10\bar{1}0$) surfaces were studied with the high-resolution ARPES measurements and self-consistent calculations. The photon energy dependence of the metallic states confirmed the two dimensionality of the metallic states. The high-resolution ARPES studies show that the incoherent states on the lower energy sides of the 2D metallic states are observed at both $SrTiO_3$(001) and ZnO($10\bar{1}0$) surfaces, indicating many-body interactions at the surfaces. The calculated subband structures show that the 2D electrons are confined within 6 nm from the surfaces.

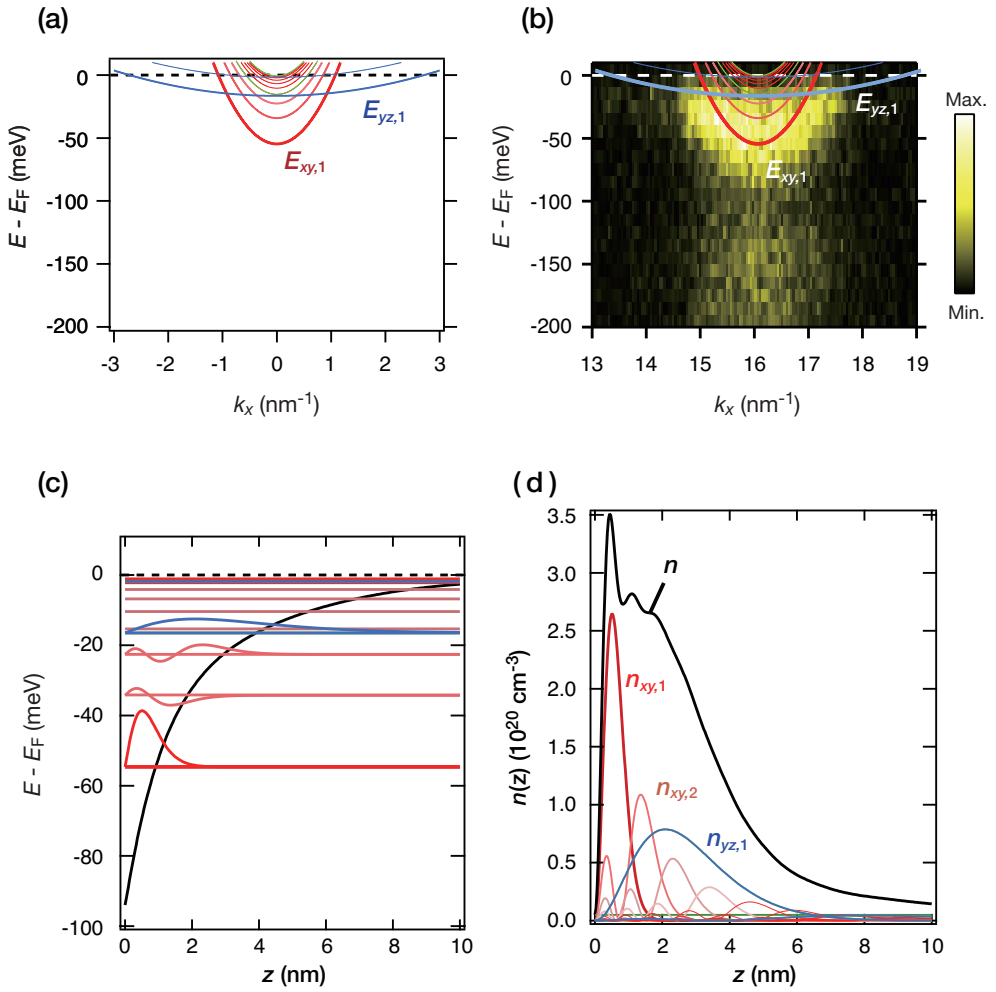

FIGURE 6.8: Calculated subband dispersions (a), potential variations (c), and partial electron densities (d) for the $SrTiO_3(001)$ surface. The calculated subbands are displayed on a ARPES result in (b) for a comparison. The energies of subband minima and the wavefunctions of the confined electrons are displayed in (c).

Chapter 7

Electron-hole recombination on the ZnO(0001) surface

Time-resolved soft X-ray photoelectron spectroscopy (PES) experiments were performed with time scales from picoseconds to nanoseconds to trace relaxation of surface photovoltage on the ZnO(0001) single crystal surface in *real time*. The band diagram of the surface has been obtained numerically using PES data, showing a depletion layer which extends to 1 μm. Temporal evolution of the photovoltage effect is well explained by a recombination process of a thermionic model, giving the photoexcited carrier lifetime of about one picosecond at the surface under the flat band condition. This lifetime agrees with the time scale reported by the previous time-resolved optical experiments.

7.1 Introduction

Zinc oxide (ZnO) has attracted much attention for its optoelectronic applications, *e.g.*, photovoltaics, light-emitting diode, and photocatalyst [131–134]. One of the important factors in the photo-induced function is dynamics of photoexcited carriers that govern optical and electronic phenomena, and their lifetime is directly related to the efficiency of optoelectronic functionalities. Time-resolved measurements of reflection, transmission, and photoluminescence spectroscopies have been carried out by a pump-probe method on various ZnO samples, i.e., nanocrystals and single crystals (Fig. 7.4) [135–140]. These authors have reported that the recombination processes of photogenerated electron-hole (e-h) pairs or excitons are enhanced by the trapping of the

carriers at impurity levels in the bulk band gap. Recently, time-resolved photoelectron spectroscopy (PES) experiments were carried out on a ZnO($10\bar{1}0$) surface to trace the relaxation process of the surface photovoltage (SPV) effect to clarify the photogenerated carrier dynamics as one of the important elementary processes [31]. Surface-sensitive results are obtained by PES as compared to optical methods [135–140]. The temporal variation of the relaxation process was described in terms of surface *e*-*h* recombination after the carrier transfer from the internal bulk to the surface over the surface potential. Time-resolved PES measures the temporal variations of the surface potential. On the other hand, time-resolved optical reflectivity and photoluminescence experiments monitor the variations of the reflectivity by the change in the carrier density and of photoluminescence by electron-hole recombination, respectively. Each experimental technique measures different physical quantities in the relaxation processes of photo-excitations. Therefore, it is essential to understand the systematic relationship between the results obtained by different experimental probes for developing optoelectronic devices.

Here, we report the detailed investigation of time-resolved soft X-ray PES experiments on the ZnO(0001) surface to clarify the surface recombination process. ZnO has the wurtzite structure and the (0001) surface is terminated with zinc atoms [Fig. 7.1(a)]. The *e*-*h* pairs are generated by the irradiation of femtosecond-pulse laser light, and the subsequent *e*-*h* charge separation leads to the SPV generation. The relaxation of the SPV was found to take nanoseconds. The relaxation process is fairly well described by the thermionic model, in which photoexcited carriers overcome the surface potential, V_{s}, to be transported to the surface and then recombine withd counterparts accumulated at the surface. The potential generated by the bulk band-bending effect near the surface and the V_{s} value, are evaluated by the valence band PES measurements of the sample surface. By tracing the relaxation of the SPV effect, we determined a photoexcited carrier lifetime at the surface under the flat band condition on the ZnO(0001) surface to be 1.7 ps. The obtained carrier lifetime at the surface is close to the values reported by the previous time-resolved optical experiments [136–138]. The agreements draw an overall temporal picture during the relaxation of the photovoltage effect at the ZnO surface.

7.2 Experimental

Time-resolved PES experiments were conducted with a pump-probe method at the soft X-ray beamline BL07LSU of SPring-8 [45–47]. The photon energies $h\nu$ of the pumping laser and the probing synchrotron radiation were 3.1 eV (a pulse width of < 50 fs) and 253 eV (about 50 ps), respectively. A detailed experimental set-up is described in Chapter 3. All the measurements were performed at room temperature. A hydrothermally grown ZnO(0001) wafer was commercially purchased from Goodwill Co., Russia. Figure 7.1(b) shows the absorption spectrum of the ZnO wafer taken in the photon energy range of 1.2−3.7 eV. The absorption edge is located at $h\nu = 3.16$ eV, which is smaller than the bulk band gap of ZnO ($E_{\mathrm{g}}^{\mathrm{ZnO}} = 3.37$ eV) [69]. The spectral features within the band gap are likely to be assigned to defects or impurity states, which would be a recombination center of the photoexcited carriers [141]. The surface of the ZnO wafer was cleaned by Ar^+ sputtering for 10 min and by successive annealing at 920−1000 K for 10 min in an oxygen atmosphere of 2×10^{-4} Pa. The quality of the crystal surface was confirmed by a 1×1 pattern of low-energy electron diffraction.

7.3 Excitation power dependence

Figure 7.1(c) is the valence-band PES spectrum which shows a spectral edge at the binding energy of $E_{\mathrm{B}} = 2.66$ eV. Since the escape depth of photoelectrons is about 1 nm [121], the energy position corresponds to the valence band maximum (VBM) of the bulk band near the surface. Using the effective mass of $0.3m_e$ [143, 144] (m_e is the free electron mass) and a bulk carrier density, the energy position of the conduction band minimum (CBM) in the bulk was calculated to be located 0.26 eV above the Fermi level. The bulk carrier density was obtained by Hall measurements to be 2×10^{14} cm^{-3}, which is of the same order of magnitude as the carrier densities of ZnO crystals grown by the hydrothermal method [145]. The magnitude of the surface potential V_{s} was determined to be $V_{\mathrm{s}} = 0.45$ eV from $E_{\mathrm{g}}^{\mathrm{ZnO}}$, the VBM at the surface, and the CBM in the bulk.

Using the relative dielectric constant of $\epsilon = 7.88$ [67], the band diagram at the ZnO(0001) surface was calculated self-consistently by solving the Poisson equation with the Fermi-Dirac distribution function so that V_{s} and the CBM position in the bulk agree with the experimentally obtained results [Fig. 7.1(d)] [1]. In the calculation, the distribution of the bulk carriers within the band bending region was solved under the

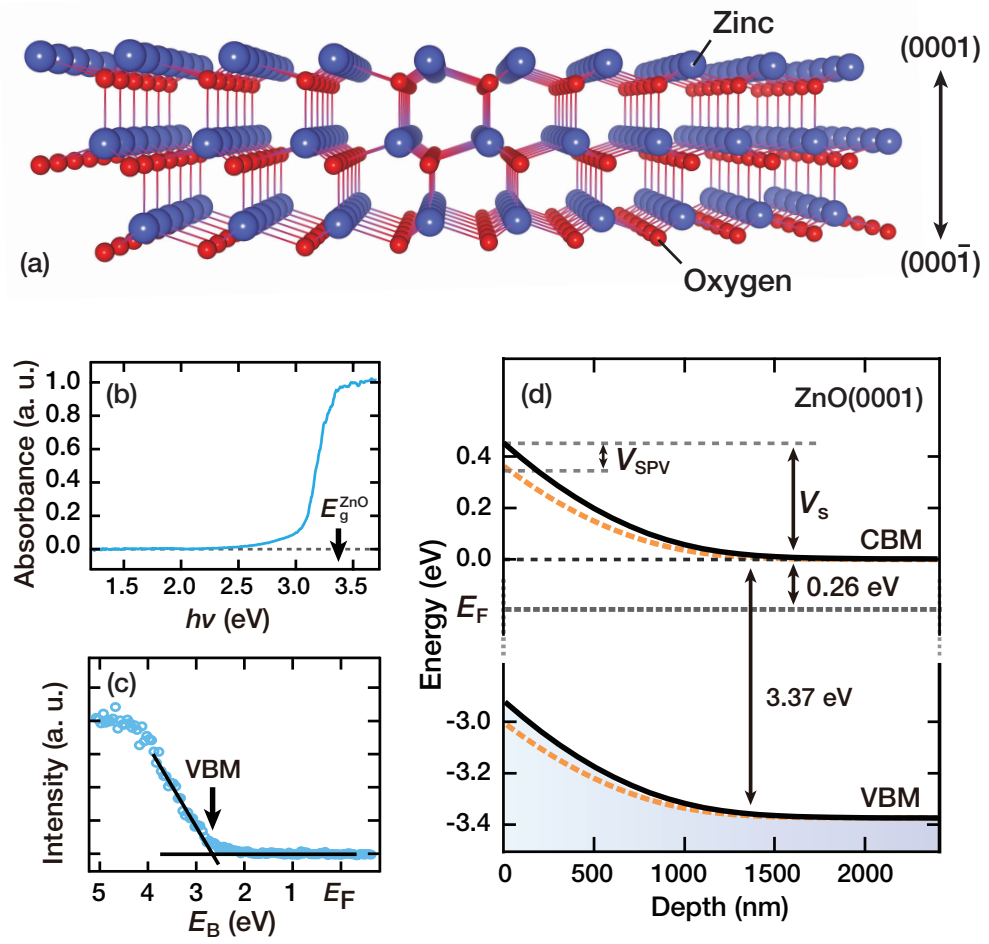

FIGURE 7.1: (a) Crystal structure of the ideal ZnO crystal [142]. The formation of facet structures is neglected in the figure. (b) Absorption spectrum of the ZnO crystal with an arrow indicating the bulk band gap position, $E_g^{ZnO} = 3.37$ eV. (c) Valence-band PES spectrum taken at the normal emission with a photon energy of $h\nu = 253$ eV. The spectral edge corresponds to the bulk valence band maximum (VBM) at the surface. (d) Calculated bulk band bending near the ZnO(0001) surface. The black solid curve is the calculated band diagram and the orange broken curve shows the band diagram at the delay time of $t = 0.2$ ns with the laser intensity (I) of 113 mJ/cm^2/pulse.

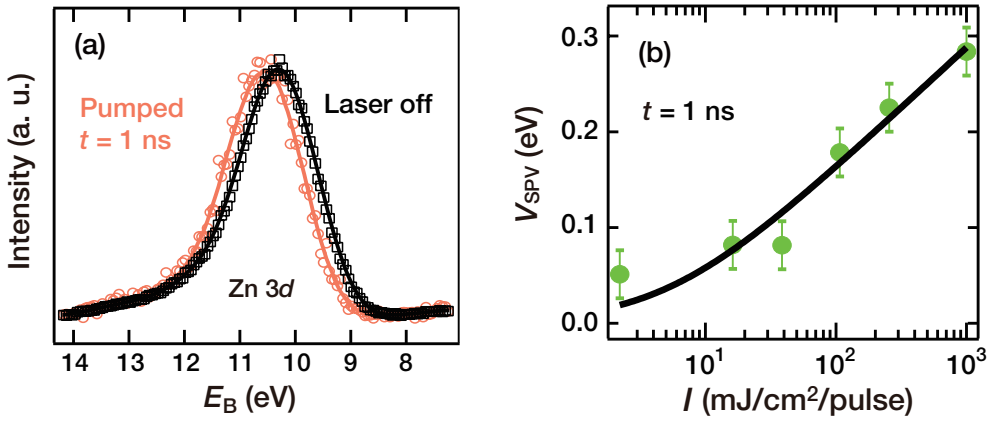

FIGURE 7.2: (a) PES spectra ($h\nu = 253$ eV) of the Zn 3d states with (circles) or without (squares) the pumping laser. The smoothed curves are shown as solid lines. The pumped spectrum was taken at the delay time of $t = 1$ ns with the laser intensity (I) of 998 mJ/cm^2/pulse. (b) V_{SPV} taken at delay time of $t = 1$ ns with different I. The solid curve is obtained by fitting the SPV shifts using Eq. (7.1).

assumption that the bulk donors, whose density N_{D} was the same as the bulk carrier density, were distributed uniformly in the sample. The space-charge layer is of the depletion-type and extends to ~ 1 μm from the surface. The depth of the depletion layer L_{D} is roughly estimated by the equation [1] $L_{\mathrm{D}} = \sqrt{2V_{\mathrm{s}}\epsilon\epsilon_0/(e^2N_{\mathrm{D}})}$, where ϵ_0 is the vacuum dielectric constant (see Chapter 2). $L_{\mathrm{D}} = 1400$ nm is obtained for our sample, supporting the calculated band structure in Fig. 7.1(d). With laser irradiation on the surface, the photoexcited electrons and holes are transferred to the bulk and surface sides, respectively, by the driving force of the potential gradient near the surface. As a result, the reduction of the bulk band bending and the potential variation by the surface photovoltage effect V_{SPV} are induced [27, 29, 32].

The energy variation of the bulk bands of a material is directly traced by following the PES peak positions [27, 29, 32]. Figure 7.2(a) shows the Zn 3d peaks with and without pumping laser irradiation. The shift of the Zn 3d peak to the higher binding energy side is clearly observed. Since the bulk band gap of ZnO is 3.37 eV, the direct transition of electrons from the VBM to the CBM in a ZnO crystal requires the photon energies larger than 3.37 eV. Thus, the optical pumping is associated with a multiphoton-absorption process or an optical transition mediated by the in-gap states as detected in Fig. 7.2(b).

The laser power dependence of the SPV shifts is shown in Fig. 7.3(b). The V_{SPV} increases with the laser intensity (I), and the data are fitted to the following equation

[27]:

$$V_{\mathrm{SPV}} = \eta' k_{\mathrm{B}} T \ln(1 + \gamma I), \tag{7.1}$$

where k_{B}, T, and γ denote the Boltzmann constant, temperature, and a proportional constant, respectively. η' is an ideality factor, which is obtained from the curve fitting to be 2.1. The proportional constant, γ, relates the number of photoexcited carriers against the laser intensity I. In the present case, we obtained $\gamma = 1.9 \times 10^{-4}$ cm$^2\mu$J^{-1} for the ZnO crystal irradiated by the laser light of $h\nu = 3.1$ eV. This γ value is much smaller than $\gamma = 10{-}20$ cm$^2\mu$J^{-1} which is reported on Si crystal surfaces pumped by photons of $h\nu = 1.55$ eV [29]. The difference can be understood by the photoexcitation process. In the latter case, the photon energy exceeds the Si bulk band gap ($E_{\mathrm{g}}^{\mathrm{Si}} = 1.1$ eV), and the photoexcitation proceeds with a single step. The former case may require the multiphoton-absorption process for photoexcitation, which is likely to result in the smaller γ value for the present ZnO experiment.

7.4 Relaxation of SPV

Relaxation of the SPV effect proceeds through recombination between the holes accumulated at the surface and the electrons transferred to the surface (Fig. 7.3, inset) [26, 27, 29, 31]. Figure 7.3(a) shows the temporal variation of V_{SPV} that shows completion of measurable relaxation after 20 ns. The time dependence is well-fitted to the following equation of the thermionic relaxation model [26, 27, 29, 31] (see Chapter 2) as shown in the inset of Fig. 7.3(a):

$$V_{\mathrm{SPV}}(t) = -\eta k_{\mathrm{B}} T \ln\left[1 - \left\{1 - \exp\left(-\frac{V_{\mathrm{SPV}}(0)}{\eta k_{\mathrm{B}} T}\right)\right\} \mathrm{e}^{-t/\tau_{\mathrm{s}}}\right], \tag{7.2}$$

where $V_{\mathrm{SPV}}(0)$ is V_{SPV} at $t = 0$, and τ_{s} is a relaxation time in the absence of the SPV (a dark carrier lifetime). The data were well-fitted as displayed in Fig. 7.3. The ideality factor was determined to be $\eta = 2.0$, which is almost the same as η' obtained from the power dependence of V_{SPV} shown in Fig. 7.2(b). The ideality factors of the Schottky contacts on various metal/ZnO interfaces [146] lie in the range between 1 and 5, and the present η (η') values are consistent with these results. In the thermionic relaxation model, the electron-hole recombination time depends on the amount of bulk band bending in a depletion layer, and thus, it varies with the delay time. The fitted relaxation time of $\tau_{\mathrm{s}} = 13.6 \pm 1.5$ ns corresponds to the value evaluated for the initial

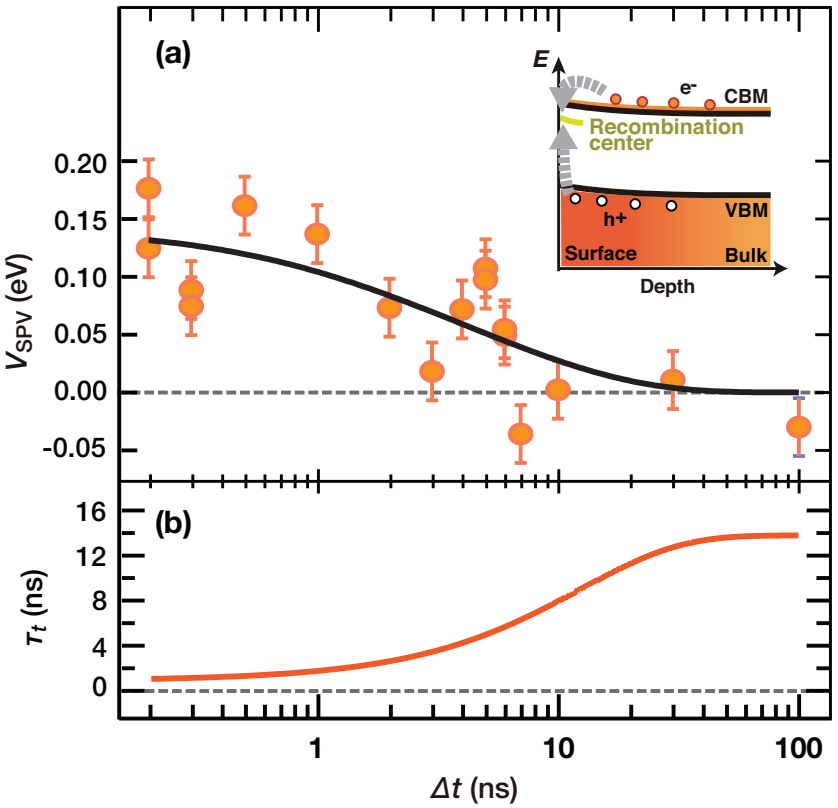

FIGURE 7.3: Time-dependences of (a) V_{SPV} taken with the laser intensity of 113 mJ/cm^2/pulse, and (b) carrier lifetime (τ_t) during the relaxation of the SPV effect. The inset shows the schematic drawing of electron-hole recombination at or near the surface. In (a), the data points are curve-fitted with the Eq. (7.2) of the thermionic model. Variation of τ_t is obtained with $\tau_t = \tau_0 \exp\{(V_{\mathrm{s}} - V_{\mathrm{SPV}})/(\eta k_{\mathrm{B}} T)\}$, where $\eta = 2.0$ and $\tau_0 = 1.7$ ps.

band bending state before the optical pumping (the dark condition with a barrier height of $V_{\mathrm{s}} = 0.45$ eV).

The relaxation time obtained in this thesis is compared with the relaxation times observed for ZnO by various experimental methods. Figure 7.4 shows that the relatively fast relaxation times of 0.5−10 ps were observed by pump-probe reflectivity and transmissivity measurements [135, 135–138]. The photoluminescence and THz absorption studies show that the relaxation times vary from 20 ps to 10000 ps [139, 140, 147, 148]. The slowest relaxations are SPV observed by PES measurements [31]. According to the reflectivity experimental results [137], a possible explanation of the fastest relaxation $\sim$ 300 fs can be due to electron-hole plasma (EHP) or carrier-carrier and carrier-LO-phonon interactions. The second fastest decay time 2.5−5.5 ps is explained by electron-acoustic-phonon interactions. The decay time of $\sim$ 55 ps are by the exciton recombinations. According to the photoluminescence experimental results [139, 140, 148], the

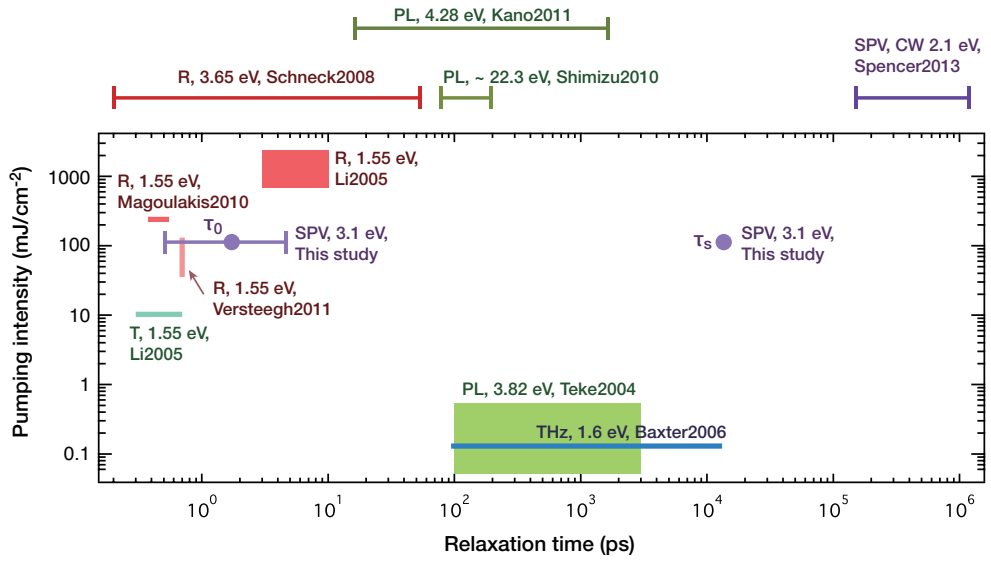

FIGURE 7.4: Pumping laser power dependencies of relaxation times detected on ZnO by various experimental methods: Reflectivity changes [135–138] denoted by R, transmissivity changes [135] denoted by T, a THz absorption change [147] denoted by THz, photoluminescence intensity changes [139, 140, 148] denoted by PL, and surface photovoltage changes [31] denoted SPV. The pumping energies of the irradiated photons are also shown in the figure in units of eV. The bars above the frame show the relaxation times, where no pumping intensity is available from the references. τ_0 and τ_s obtained in this study are shown in the purple dots.

relaxations of photoluminescence intensities are explained by the lifetimes of free or bound excitons. With the time-resolved PES measurement, the potential change of SPV shifts is observed and much longer relaxation time is obtained.

In the case of the flat band condition, or absence of the band bending effect, the carrier lifetime τ_0 can be expressed as a following equation [26, 27, 29, 31]:

$$\tau_0 = \tau_s \exp\left(- \frac{V_s}{\eta k_B T} \right). \tag{7.3}$$

By using the band parameter of $V_s = 0.45$ eV, as depicted in Fig. 7.1, one obtains $\tau_0 = 1.7$ ps for the present ZnO(0001) sample surface. It should be noted that the τ_0 is in the time range of 0.5−4.9 ps when one takes into account the resolution of ±1.5 ns for τ_s, ±0.03 eV for V_s, and ±0.1 for η in the calculations (Fig. 7.4). The surface recombination time of 1.7 ps for the photoexcited carriers at the ZnO(0001) surface is in good agreement with values of the surface carrier decay time ($\sim$ 1 ps) reported in the literatures of time-resolved reflectivity and transmissivity experiments (see Fig. 7.3) [135–138]. These agreements indicate that the relaxation of the SPV

effect on the ZnO(0001) crystal proceeds with thermal diffusion of the electrons over the surface potential from the internal bulk, followed by *e*-*h* recombination at the same recombination centers reported in the literatures [135–138]. A proper value of the recombination time allows one to evaluate the diffusion length of the photocarriers as $l = \sqrt{\tau_0 \mu k_B T/e}$, where μ is a carrier mobility. Taking the value ($\mu = 131-205$ $cm^2V^{-1}s^{-1}$) for a bulk ZnO crystal [146], the diffusion length is estimated as $l \sim 30$ nm at room temperature. In a previous time-resolved reflectivity study, the thickness of the surface layer, which is responsible for the *e*-*h* recombination, is estimated to be 30−100 nm [136]. It was discussed that the density of singly ionized oxygen vacancy traps (which can be the recombination centers) is much higher in such a surface recombination layer than in the interior of the crystal [136, 138, 141]. Therefore, the photocarriers located between the surface and 30 nm from the surface recombination layer play an important role for the ultrafast ($\sim$ 1 ps) recombination process in the flat-band ZnO crystals. On the other hand, it has been known that the electronic properties of the topmost surface electronic structure are completely different from those in the bulk [39], and electronic states localized in the topmost surface (surface states) can also become the recombination centers in the bulk band gap. We infer that *e*-*h* recombination takes place at the trapping sites at the topmost surface (the surface state) and in the subsurface layer (the impurity states) with the different carrier-capturing cross-sections.

The bulk band-bending effect, dealt in the present work, is inevitable in studying carrier dynamics on semiconductor surfaces. The amount of band bending depends sensitively on the surface and its treatment [1, 12]. The flat-band carrier lifetime, τ_0, allows evaluation of the relaxation time of various depletion layers depending on the surface and its treatment. The carrier lifetime increases exponentially with the amount of band bending at the surface (V_s). The relation can be used to design ZnO-based photocatalysts or photovoltaics elements [131–134].

7.5 Conclusion

In summary, time-resolved soft X-ray PES experiments were carried out on the ZnO(0001) surface to trace the relaxation of SPV effect. With the simultaneous evaluation of the bulk band bending effect, the flat-band carrier lifetime at the surface was estimated to be 1.7 ps, which is similar to those reported by the previous time-resolved optical experiments. The consistency allows one to draw the overall temporal evolution

of photoexcited carriers at the ZnO surface, which leads to both developments of a new optoelectronically functional materials and improvements of the efficiency.

Chapter 8

Summary and future prospect

8.1 Summary

In the present thesis, the band structures and carrier dynamics related with their band bending structures of metal-oxide surfaces have been studied by the polarization-dependent angle-resolved and time-resolved photoelectron spectroscopy measurements.

In Chapter 4, a simple and effective anisotropic approach to self-consistently solve the Poisson-Schrödinger equations have been proposed to reproduced the previous angle-resolved photoelectron spectroscopy (ARPES) results. Previous studies have used the wedge model and the *ab initio* calculations to obtain the subband structures and potential variations at $SrTiO_3(001)$ surfaces. However, the wedge model barely reproduce ARPES results and *ab initio* calculations require a large amount of the computational power and initial parameters. Moreover, important physics are sometimes hidden in the calculations. Therefore, the anisotropic effective-mass approximations (AEA) model has been proposed. The calculated electronic structures of a two-dimensional electron gas (2DEG) at the ZnO surface revealed that the AEA and modified Thomas-Fermi approximation (MTFA) models yielded similar results. The AEA model succeeded in reproducing the experimentally obtained subband structure at $SrTiO_3(001)$ surfaces which is originated from the anisotropic Ti $3d$ $2t_g$ bands. The calculations further indicate the existence of the high electron density, exceeding 2×10^{21} cm^{-3} and the high electric field of 20 MVcm^{-1} at the surface. Furthermore, we show that the appearance of the two-dimensional (2D) metallic states in the ARPES spectra can be discussed in terms of their depth profile and the mean-escape-depth of the photoelectrons by the calculated results.

In Chapter 5, the experimental demonstrations of metallization of the hydrogen-adsorbed $SrTiO_3(001)$ surface are described. Former studies have shown that 2DEGs of $SrTiO_3(001)$ surfaces are induced by oxygen vacancies created by cleaving the crystal or by irradiation of ultra-violet light. The oxygen vacancies can be scatterers for conducting electrons and 2DEGs of an ordered $SrTiO_3(001)$ surface is desired. Metallization of the $SrTiO_3(001)$ surface induced by the hydrogen adsorption has been theoretically predicted. However, no experimental realization has been reported. We have succeeded in obtaining carbon-free and well-ordered $SrTiO_3(001)$ surfaces by annealing the crystal at relatively low temperature in an oxygen atmosphere. ARPES and four-point probes (4PP) electrical conductivity measurements have been conducted to prove the metal-insulator transitions at the hydrogen-adsorbed $SrTiO_3(001)$ surfaces. The increase of the surface conductivities and the increase of the photoelectron intensities at the Fermi level induced by hydrogen adsorption at the surface clearly show the metallization of the surface. Our results show that the sheet conductivity exceeds the 2D Ioffe-Regel limit and the electron transport is in the metallic conduction regime. The core-level shifts to the higher binding energy side by hydrogen adsorption show that the metallization is induced by charge transfer from the hydrogen atoms to the $SrTiO_3(001)$ surface. Moreover, characterizations of the electronic structures have been carried out by the polarization-dependent ARPES studies and clarified the origins of the peak structures of the valence bands. The number of hydrogen atoms on the surface is evaluated to be $0.8-1.1 \times 10^{14}$ cm^{-2} (or $0.12-0.17$ atoms per unit cell) from the core-level photoelectron spectroscopy (PES) intensity analysis.

In Chapter 6, further studies on the 2DEG at the hydrogen-adsorbed $SrTiO_3(001)$ and $ZnO(10\bar{1}0)$ surfaces have been performed. Photon energy dependences of the PES spectra show the two dimensionality of the metallic states. The subband structures and potential variations are clarified by the self-consistent calculations with the AEA model proposed in Chapter 4. The high-resolution ARPES studies show that the incoherent states on the lower energy sides of the 2D metallic states are observed at both $SrTiO_3(001)$ and $ZnO(10\bar{1}0)$ surfaces, indicating the many-body interactions at the surfaces.

In Chapter 7, the relaxation process of the surface photovoltage effect on the ZnO(0001) single crystal surface has been studied by the time-resolved soft X-ray photoelectron spectroscopy experiments. The band bending structure of the surface has been calculated with the parameters obtained from the PES results and the Hall measurements and the upward band bending structure extending 1 μm was clarified. The temporal evolution of the photovoltage effect is well explained by a recombination process of

a thermionic model, giving the photoexcited carrier lifetime of about one picosecond at the surface under the flat band condition. The obtained lifetime agrees with the temporal range reported by the previous time-resolved optical experiments, indicating that recombination of the photoexcited carriers takes the same process reported in the time-resolved reflectivity and transmissivity studies.

8.2 Future prospect

In the discussion above, the band bending electronic structures and electron-hole recombination processes have been clarified. By using the discussion in this thesis, it will be interesting to analyze the standing waves of the 2D metallic states created on the $SrTiO_3(001)$ and $ZnO(10\bar{1}0)$ surfaces at very low temperatures. It is known that $SrTiO_3(001)$ crystal becomes superconductor below 400 mK [149]. Moreover, recent spin-resolved PES measurements indicate the existence of a giant Rashba splitting of the 2D metallic states [21]. Therefore, spin-resolved ARPES study is also an interesting experiment. In order to understand the band-bending structures and to prove the theoretical model, comparisons of the calculated results and the experimental results are needed. Because the probing depths of hard X-ray PES (HAXPES) measurements exceed 1 nm (see Fig. 3.5), the depth profile of the band bending structure can be experimentally obtained by HAXPES studies. As shown in the map of the relaxation time on ZnO in Fig. 7.4, there are large order of differences in the relaxation time depending on the experimental methods. In order to understand the whole picture of the carrier dynamics of electrons, holes, excitons, and phonons, the ideal approach is that one measures temporal variations of relaxation processes in various time-resolved experimental systems using the same sample.

Appendix A

Calculation methods

A.1 Wedge model

The most simplified model for the potential variation was obtained using the linear function, $V(z) = eFz + V_{\mathrm{s}}$, where F is a constant with the same dimension as the electric field. This model is called the wedge model or the triangular model. Equation (4.3) can be rewritten as

$$\frac{\partial^2 \phi_{\alpha k_{\parallel} j}(z)}{\partial z^2} = -\frac{2m_{\alpha z}}{\hbar^2}(E^0_{\alpha j} \ - eFz \ - V_{\mathrm{s}})\phi_{\alpha k_{\parallel} j}(z). \tag{A.1}$$

By taking

$$t_\alpha = \left(\frac{2m_{\alpha z}eF}{\hbar^2}\right)^{\frac{1}{3}}\left(z \ - \frac{E^0_{\alpha j} - V_{\mathrm{s}}}{eF}\right), \tag{A.2}$$

Eq. (A.1) becomes

$$\frac{\partial^2 \phi_{\alpha k_{\parallel} j}(t_\alpha)}{\partial t_\alpha^2} = t_\alpha \cdot \phi_{\alpha k_{\parallel} j}(t_\alpha). \tag{A.3}$$

This equation can be solved analytically and the solution is given descried by an Airy function [150]. It is required that $\phi_{\alpha k_{\parallel} j}(z) = 0$ at $z = \infty$, to obtain $\phi_{\alpha k_{\parallel} j}(t_\alpha) = C \cdot \mathrm{Ai}(t_\alpha)$, or

$$\phi_{\alpha k_{\parallel} j}(z) = C \cdot \mathrm{Ai}\left\{\left(\frac{2m_{\alpha z}eF}{\hbar^2}\right)^{\frac{1}{3}}\left(z \ - \frac{E^0_{\alpha j} - V_{\mathrm{s}}}{eF}\right)\right\}, \tag{A.4}$$

where C is the normalization constant. The eigenenergies of this equation could be well-approximated by [53]

$$E^0_{\alpha j} \approx \left(\frac{\hbar^2}{2m_{\alpha z}}\right)^{\frac{1}{3}} \left\{\frac{3}{2}eF\left(j-\frac{1}{4}\right)\right\} + V_{\rm s}, \tag{A.5}$$

where j $(= 1, 2, 3, ...)$ denotes the quantum number. It should be noted that the electrons with a larger effective mass along the z direction $m_{\alpha z}$ takes lower subbnad energies within the wedge model.

A.2 MTFA model

In the modified Thomas-Fermi approximation (MTFA) model for an accumulation layer with parabolic band dispersion, the electron density $[n(z)]$ in Eq. (4.5) is given by [24]

$$n(z) = \int_{-\infty}^{\infty} dE\ g'_{\rm 3D}(E) f_{\rm FD}(E) f(E,z), \tag{A.6}$$

where $g'_{\rm 3D}(E)$ is the density of states with an isotropic effective mass (m^*), and $f(E,z)$ is the MTFA factor given by [151, 152]

$$g'_{\rm 3D}(E,z) = \frac{\sqrt{2(E-V(z))}}{\pi^2\hbar^3} m^{*\frac{3}{2}} \theta(E-V(z)), \tag{A.7a}$$

$$f(E,z) = 1 - {\rm sinc}\left\{\frac{2z}{L_{\rm th}}\left(\frac{E}{k_{\rm B}T}\right)^{\frac{1}{2}}\left(1+\frac{E}{E_{\rm g}}\right)^{\frac{1}{2}}\right\}. \tag{A.7b}$$

The thermal length $(L_{\rm th})$ is given by $L_{\rm th} = \hbar/(2m^* k_{\rm B}T)^{1/2}$, where $E_{\rm g}$ is the bulk band gap. The eigenenergies and eigenfunctions were obtained using Eq. (A.9) (see Appendix C) after self-consistent calculations using the Poisson equation were performed [Eq. (4.5)].

A.3 Eigenenergies and eigenfunctions

For a given potential variation, the wave functions and eigenenergies of electrons in the accumulation layer can be obtained by taking the Fourier transform of the wave

function [24, 66]

$$\phi_{\alpha k_{\parallel} j}(z) = \sum_{\nu=0}^{\infty} \sqrt{\frac{2}{L}} a_{\nu}^{\alpha k_{\parallel} j} \sin(\frac{\nu\pi}{L} z), \tag{A.8}$$

where L is the full depth of the band. By using Eq. (A.8), Eq. (4.3) can be rewritten as

$$\mathbf{M}_{\alpha}\ \mathbf{a}_{\alpha} = \mathbf{E}_{\alpha}^{0} \mathbf{a}_{\alpha}. \tag{A.9}$$

The matrix elements are given by

$$\begin{aligned} [\mathbf{M}_{\alpha}]_{\nu\nu'} &= \frac{\hbar^2}{2m_{\alpha z}} \left(\frac{\nu\pi}{L}\right)^2 \delta_{\nu\nu'} \\ &\quad + \frac{2}{L} \int_0^L dz V(z) \sin\left(\frac{\nu\pi}{L} z\right) \left(\frac{\nu'\pi}{L} z\right), \end{aligned} \tag{A.10}$$

where $\delta_{\nu\nu'}$ is the Kronecker delta. The eigenfunctions and eigenenergies were obtained by solving the determinant of the matrix in Eq. (A.9). For numerical calculations, L can be set to be the depth where the variation in the potential is saturated. The computation time increases on ν^2. Reasonable results could be obtained using $\nu = 150 - 500$.

Publications

Publications included in this thesis

1. **Angle-resolved photoelectron spectroscopy studies of two-dimensional electronic states at ZnO and $SrTiO_3$ surfaces**
   R. Yukawa, K. Ozawa, S. Yamamoto, H.Iwasawa, K. Shimada, Eike F. Schwier, K. Yoshimatsu, H. Kumigashira, H. Namatame, M. Taniguchi, and I. Matsuda
   to be submitted for publication.

2. **Anisotropic effective mass approach for multiple subband structures at wide-gap semiconductor surfaces: Application to accumulation layers of $SrTiO_3$ and ZnO**
   R. Yukawa, K. Ozawa, R.-Y. Liu, S. Yamamoto, and I. Matsuda
   submitted to Phys. Rev. B.

3. **Electron-hole recombination on ZnO(0001) single-crystal surface studied by time-resolved soft X-ray photoelectron spectroscopy**
   R. Yukawa, S. Yamamoto, K. Ozawa, M. Emori, M. Ogawa, S. Yamamoto, K. Fujikawa, R. Hobara, S. Kitagawa, H. Daimon, H. Sakama, and I. Matsuda
   Appl. Phys. Lett. **105**, 151602 (2014).

4. **Electronic structure of the hydrogen-adsorbed $SrTiO_3$(001) surface studied by polarization-dependent photoemission spectroscopy**
   R. Yukawa S. Yamamoto, K. Ozawa, M. D'Angelo, M. Ogawa, M.G. Silly, F. Sirotti, and I. Matsuda
   Phys. Rev. B **87**, 115314 (2013).

5. **Hydrogen-Induced Surface Metallization of $SrTiO_3$(001)**
   M. D'Angelo, R. Yukawa, K. Ozawa, S. Yamamoto, T. Hirahara, S. Hasegawa, M. G. Silly, F. Sirotti, and I. Matsuda
   Phys. Rev. Lett. **108**, 116802 (2012).

Bibliography

[1] H. Lüth, *Surfaces and Interfaces of Solid Materials* (Springer-Verlag, 1995).

[2] S. Thiel, G. Hammerl, a. Schmehl, C. W. Schneider, and J. Mannhart, Science **313**, 1942 (2006).

[3] C. Beenakker, Phys. Rev. Lett. **64**, 216 (1990).

[4] S. Koch, R. Haug, K. Klitzing, and K. Ploog, Phys. Rev. Lett. **67**, 883 (1991).

[5] G. Heiland and P. Kunstmann, Surf. Sci. **13**, 72 (1969).

[6] C. G. Van de Walle, Phys. Rev. Lett. **85**, 1012 (2000).

[7] A. Many, I. Wagner, and A. Rosenthal, Phys. Rev. Lett. **46**, 1648 (1981).

[8] M. Wolovelsky, Y. Goldstein, and O. Millo, Phys. Rev. B **57**, 6274 (1998).

[9] Y. Wang, B. Meyer, X. Yin, M. Kunat, D. Langenberg, F. Traeger, A. Birkner, and C. Wöll, Phys. Rev. Lett. **95**, 266104 (2005).

[10] K. Ozawa and K. Mase, Phys. Rev. B **81**, 205322 (2010).

[11] K. Ozawa and K. Mase, Phys. Status Solidi A **207**, 277 (2010).

[12] K. Ozawa and K. Mase, Phys. Rev. B **83**, 125406 (2011).

[13] A. Ohtomo and H. Y. Hwang, Nature **427**, 423 (2004).

[14] W. Siemons, G. Koster, H. Yamamoto, W. Harrison, G. Lucovsky, T. Geballe, D. Blank, and M. Beasley, Phys. Rev. Lett. **98**, 196802 (2007).

[15] A. Brinkman, M. Huijben, M. van Zalk, J. Huijben, U. Zeitler, J. C. Maan, W. G. van der Wiel, G. Rijnders, D. H. a. Blank, and H. Hilgenkamp, Nat. Mater. **6**, 493 (2007).

[16] M. Basletic, J.-L. Maurice, C. Carrétéro, G. Herranz, O. Copie, M. Bibes, E. Jacquet, K. Bouzehouane, S. Fusil, and a. Barthélémy, Nat. Mater. **7**, 621 (2008).

[17] M. Breitschaft, V. Tinkl, N. Pavlenko, S. Paetel, C. Richter, J. R. Kirtley, Y. C. Liao, G. Hammerl, V. Eyert, T. Kopp, et al., Phys. Rev. B **81**, 153414 (2010).

[18] N. Reyren, S. Thiel, a. D. Caviglia, L. F. Kourkoutis, G. Hammerl, C. Richter, C. W. Schneider, T. Kopp, A.-S. Rüetschi, D. Jaccard, et al., Science **317**, 1196 (2007).

[19] W. Meevasana, P. D. C. King, R. H. He, S.-K. Mo, . Hashimoto, A. Tamai, P. Songsiriritthigul, F. Baumberger, and Z.-X. Shen, Nat. Mater. **10**, 114 (2011).

[20] A. F. Santander-Syro, O. Copie, T. Kondo, F. Fortuna, S. Pailhès, R. Weht, X. G. Qiu, F. Bertran, A. Nicolaou, A. Taleb-Ibrahimi, et al., Nature **469**, 189 (2011).

[21] A. F. Santander-Syro, F. Fortuna, C. Bareille, T. C. Rödel, G. Landolt, N. C. Plumb, J. H. Dil, and M. Radović, Nat. Mater. **13**, 1085 (2014).

[22] A. Koitzsch, J. Ocker, M. Knupfer, M. Dekker, K. Dörr, B. Büchner, and P. Hoffmann, Phys. Rev. B **84**, 245121 (2011).

[23] P. D. C. King, S. McKeown Walker, A. Tamai, A. de la Torre, T. Eknapakul, P. Buaphet, S.-K. Mo, W. Meevasana, M. S. Bahramy, and F. Baumberger, Nat. Commun. **5**, 3414 (2014).

[24] P. King, T. Veal, and C. McConville, Phys. Rev. B **77**, 125305 (2008).

[25] S. Moser, L. Moreschini, J. Jaćimović, O. S. Barišić, H. Berger, A. Magrez, Y. J. Chang, K. S. Kim, A. Bostwick, E. Rotenberg, et al., Phys. Rev. Lett. **110**, 196403 (2013).

[26] K. Ozawa, M. Emori, S. Yamamoto, R. Yukawa, Sh. Yamamoto, R. Hobara, K. Fujikawa, H. Sakama, and I. Matsuda, J. Phys. Chem. Lett. **5**, 1953 (2014).

[27] D. Bröcker, T. Gießel, and W. Widdra, Chem. Phys. **299**, 247 (2004).

[28] M. Sze and K. K. Ng, *Physics of Semiconductor Devices* (Wiley, New York, 2007).

[29] M. Ogawa, S. Yamamoto, K. Fujikawa, R. Hobara, R. Yukawa, Sh. Yamamoto, S. Kitagawa, D. Pierucci, M. G. Silly, C.-H. Lin, et al., Phys. Rev. B **88**, 165313 (2013).

[30] Y. Zhang, T. Xie, T. Jiang, X. Wei, S. Pang, X. Wang, and D. Wang, Nanotechnology **20**, 155707 (2009).

[31] B. F. Spencer, D. M. Graham, S. J. O. Hardman, E. A. Seddon, M. J. Cliffe, K. L. Syres, A. G. Thomas, S. K. Stubbs, F. Sirotti, M. G. Silly, et al., Phys. Rev. B **88**, 195301 (2013).

[32] M. Ogawa, S. Yamamoto, R. Yukawa, R. Hobara, C.-H. Lin, R.-Y. Liu, S.-J. Tang, and I. Matsuda, Phys. Rev. B **87**, 235308 (2013).

[33] Winfried Monch, *Semiconductor Surfaces and Interfaces* (Springer, Berlin, 2001).

[34] A. Einstein, Ann. Phys. **322**, 132 (1905).

[35] S. Hüfner, *Photoelectron Spectroscopy* (Springer, 1995).

[36] C. Berglund and W. Spicer, Phys. Rev. **136**, A1030 (1964).

[37] T. Miller, W. McMahon, and T. Chiang, Phys. Rev. Lett. **77**, 1167 (1996).

[38] E. D. Hansen, T. Miller, and T.-C. Chiang, Phys. Rev. B **55**, 1871 (1997).

[39] A. Zangwill, *Physics at surfaces* (Cambridge University Press, 1988).

[40] D. Malterre, M. Grioni, and Y. Baer, Adv. Phys. **45**, 299 (1996).

[41] *VG SCIENTA Co., Ltd.*, URL `http://www.vgscienta.com`.

[42] O. Jagutzki, A. Cerezo, A. Czasch, R. Dörner, M. Hattaß, M. Huang, V. Mergel, U. Spillmann, K. Ullmann-Pfleger, T. Weber, et al., IEEE Trans. Nucl. Sci. **49 II**, 2477 (2002).

[43] P. S. Kirchmann, L. Rettig, D. Nandi, U. Lipowski, M. Wolf, and U. Bovensiepen, Appl. Phys. A Mater. Sci. Process. **91**, 211 (2008).

[44] G. Öhrwall, P. Karlsson, M. Wirde, M. Lundqvist, P. Andersson, D. Ceolin, B. Wannberg, T. Kachel, H. Dürr, W. Eberhardt, et al., J. Electron Spectros. Relat. Phenomena **183**, 125 (2011).

[45] M. Ogawa, S. Yamamoto, Y. Kousa, F. Nakamura, R. Yukawa, A. Fukushima, A. Harasawa, H. Kondoh, Y. Tanaka, A. Kakizaki, et al., Rev. Sci. Instrum. **83**, 023109 (2012).

[46] S. Yamamoto and I. Matsuda, J. Phys. Soc. Japan **82**, 021003 (2013).

[47] S. Yamamoto, Y. Senba, T. Tanaka, H. Ohashi, T. Hirono, H. Kimura, M. Fujisawa, J. Miyawaki, A. Harasawa, T. Seike, et al., J. Synchrotron Radiat. **21**, 352 (2014).

[48] L. J. Van der Pauw, Philips Res. Repts **13**, 1 (1958).

[49] S. Hasegawa and S. Ino, Phys. Rev. Lett. **68**, 1192 (1992).

[50] M. D'angelo, K. Takase, N. Miyata, T. Hirahara, S. Hasegawa, A. Nishide, M. Ogawa, and I. Matsuda, Phys. Rev. B **79**, 035318 (2009).

[51] M. Yamada, T. Hirahara, R. Hobara, S. Hasegawa, H. Mizuno, Y. Miyatake, and T. Nagamura, e-Journal Surf. Sci. Nanotechnol. **10**, 400 (2012).

[52] F. Stern and W. Howard, Phys. Rev. **163**, 816 (1967).

[53] Hans Lüth, *Solid Surfaces, Interfaces and Thin Films* (Springer, 2010), 5th ed.

[54] H. Yu and J. Hermanson, Phys. Rev. B **41**, 5991 (1990).

[55] K. Ishizaka, M. S. Bahramy, H. Murakawa, M. Sakano, T. Shimojima, T. Sonobe, K. Koizumi, S. Shin, H. Miyahara, A. Kimura, et al., Nat. Mater. **10**, 521 (2011).

[56] P. King, T. Veal, C. McConville, J. Zúñiga Pérez, V. Muñoz Sanjosé, M. Hopkinson, E. Rienks, M. Jensen, and P. Hofmann, Phys. Rev. Lett. **104**, 256803 (2010).

[57] T. Ando, Rev. Mod. Phys. **54**, 437 (1982).

[58] J. Shen, H. Lee, R. Valentí, and H. O. Jeschke, Phys. Rev. B **86**, 195119 (2012).

[59] M. S. Bahramy, P. D. C. King, A. de la Torre, J. Chang, M. Shi, L. Patthey, G. Balakrishnan, P. Hofmann, R. Arita, N. Nagaosa, et al., Nat. Commun. **3**, 1159 (2012).

[60] C. Duke, Phys. Rev. **159**, 632 (1967).

[61] G. Baraff and J. Appelbaum, Phys. Rev. B **5**, 475 (1972).

[62] H. Übensee, G. Paasch, J.-P. Zöllner, and S. Handschack, Phys. Status Solidi (B) **147**, 823 (1988).

[63] K. H. L. Zhang, R. G. Egdell, F. Offi, S. Iacobucci, L. Petaccia, S. Gorovikov, and P. D. C. King, Phys. Rev. Lett. **110**, 056803 (2013).

[64] M. D'Angelo, R. Yukawa, K. Ozawa, S. Yamamoto, T. Hirahara, S. Hasegawa, M. G. Silly, F. Sirotti, and I. Matsuda, Phys. Rev. Lett. **108**, 116802 (2012).

[65] R. Yukawa, S. Yamamoto, K. Ozawa, M. DAngelo, M. Ogawa, M. G. Silly, F. Sirotti, and I. Matsuda, Phys. Rev. B **87**, 115314 (2013).

[66] S. Abe, T. Inaoka, and M. Hasegawa, Phys. Rev. B **66**, 205309 (2002).

[67] H. Zheng, A. Weismann, and R. Berndt, Phys. Rev. Lett. **110**, 226101 (2013).

[68] E. O. Kane, J. Phys. Chem. Solids **1**, 249 (1957).

[69] Y. F. Chen, D. M. Bagnall, H. Koh, K. Park, K. Hiraga, Z. Zhu, and T. Yao, J. of Appl. Phys. **84**, 3912 (1998).

[70] D. Reynolds, D. Look, B. Jogai, C. Litton, G. Cantwell, and W. Harsch, Phys. Rev. B **60**, 2340 (1999).

[71] K. Ozawa and K. Mase, Phys. Status Solidi A **207**, 277 (2010).

[72] R. C. Neville, J. Appl. Phys. **43**, 2124 (1972).

[73] C. Ang, R. Guo, A. S. Bhalla, and L. E. Cross, J. Appl. Phys. **87**, 3937 (2000).

[74] H.-M. Christen, J. Mannhart, E. Williams, and C. Gerber, Phys. Rev. B **49**, 12095 (1994).

[75] O. Copie, V. Garcia, C. Bödefeld, C. Carrétéro, M. Bibes, G. Herranz, E. Jacquet, J.-L. Maurice, B. Vinter, S. Fusil, et al., Phys. Rev. Lett. **102**, 216804 (2009).

[76] P. Zhang, P. Richard, T. Qian, Y.-M. Xu, X. Dai, and H. Ding, Rev. Sci. Instrum. **82**, 043712 (2011).

[77] H. Takagi and H. Y. Hwang, Science **327**, 1601 (2010).

[78] C. Cen, S. Thiel, J. Mannhart, and J. Levy, Science **323**, 1026 (2009).

[79] A. P. Ramirez, Science **315**, 1377 (2007).

[80] A. Ohtomo, D. A. Muller, J. L. Grazul, and H. Y. Hwang, Nature **419**, 378 (2002).

[81] P. Willmott, S. Pauli, R. Herger, C. Schlepütz, D. Martoccia, B. Patterson, B. Delley, R. Clarke, D. Kumah, C. Cionca, et al., Phys. Rev. Lett. **99**, 155502 (2007).

[82] A. Kalabukhov, R. Gunnarsson, J. Börjesson, E. Olsson, T. Claeson, and D. Winkler, Phys. Rev. B **75**, 121404 (2007).

[83] N. Nakagawa, H. Y. Hwang, and D. a. Muller, Nat. Mater. **5**, 204 (2006).

[84] F. Lin, S. Wang, F. Zheng, G. Zhou, J. Wu, B.-L. Gu, and W. Duan, Phys. Rev. B **79**, 035311 (2009).

[85] V. Derycke, P. G. Soukiassian, F. Amy, Y. J. Chabal, M. D. D'angelo, H. B. Enriquez, and M. G. Silly, Nat. Mater. **2**, 253 (2003).

[86] F. Polack, M. Silly, C. Chauvet, B. Lagarde, N. Bergeard, M. Izquierdo, O. Chubar, D. Krizmancic, M. Ribbens, J.-P. Duval, et al., AIP Conf. Proc. **1234**, 185 (2010).

[87] N. Bergeard, M. G. Silly, D. Krizmancic, C. Chauvet, M. Guzzo, J. P. Ricaud, M. Izquierdo, L. Stebel, P. Pittana, R. Sergo, et al., J. Synchrotron Radiat. **18**, 245 (2011).

[88] T. Nishimura, A. Ikeda, H. Namba, T. Morishita, and Y. Kido, Surf. Sci. **421**, 273 (1999).

[89] D. D. Sarma, S. R. Barman, H. Kajueter, and G. Kotliar, Europhys. Lett. **36**, 307 (1996).

[90] Y. Haruyama, S. Kodaira, Y. Aiura, H. Bando, Y. Nishihara, T. Maruyama, Y. Sakisaka, and H. Kato, Phys. Rev. B **53**, 8032 (1996).

[91] Y. J. Chang, A. Bostwick, Y. S. Kim, K. Horn, and E. Rotenberg, Phys. Rev. B **81**, 235109 (2010).

[92] N. B. Brookes, F. M. Quinn, and G. Thornton, Phys. Scr. **36**, 711 (1987).

[93] F. Gervais, J.-L. Servoin, A. Baratoff, J. Bednorz, and G. Binnig, Phys. Rev. B **47**, 8187 (1993).

[94] S. Ferrer and G. Somorjai, Surf. Sci. **94**, 41 (1980).

[95] Y. Aiura, H. Bando, T. Maruyama, Y. Nishihara, Y. Haruyama, S. Kodaira, T. Komeda, Y. Sakisaka, and H. Kato, Physica C **235**, 1009 (1994).

[96] Y. Aiura, I. Hase, H. Bando, T. Yasue, T. Saitoh, and D. Dessau, Surf. Sci. **515**, 61 (2002).

[97] D. Kobayashi, H. Kumigashira, M. Oshima, T. Ohnishi, M. Lippmaa, K. Ono, M. Kawasaki, and H. Koinuma, J. Appl. Phys. **96**, 7183 (2004).

[98] Y. Ishida, R. Eguchi, M. Matsunami, K. Horiba, M. Taguchi, A. Chainani, Y. Senba, H. Ohashi, H. Ohta, and S. Shin, Phys. Rev. Lett. **100**, 056401 (2008).

[99] A. Fujimori, I. Hase, H. Namatame, Y. Fujishima, Y. Tokura, K. Takegahara, and F. M. F. de Groot, Phys. Rev. Lett. **69**, 1796 (1992).

[100] A. Fujimori, A. E. Bocquet, K. Morikawa, K. Kobayashi, T. Saitoh, Y. Tokura, I. Hasex, and M. Onoda, J. Phys. Chem. Solids **57**, 1379 (1996).

[101] M. Imada, A. Fujimori, and Y. Tokura, Rev. Mod. Phys. **70**, 1039 (1998).

[102] R. Moss, Ph.D. thesis, Karlsruhe University (1994).

[103] M. Minohara, K. Horiba, H. Kumigashira, E. Ikenaga, and M. Oshima, Phys. Rev. B **85**, 165108 (2012).

[104] I. Matsuda, T. Hirahara, M. Konishi, C. Liu, H. Morikawa, M. Dangelo, S. Hasegawa, T. Okuda, and T. Kinoshita, Phys. Rev. B **71**, 1 (2005).

[105] A. Spinelli, M. A. Torija, C. Liu, C. Jan, and C. Leighton, Phys. Rev. B **81**, 155110 (2010).

[106] W. Lawless, Phys. Rev. B **17**, 1458 (1978).

[107] W. Meevasana, X. J. Zhou, B. Moritz, C.-C. Chen, R. H. He, S.-I. Fujimori, D. H. Lu, S.-K. Mo, R. G. Moore, F. Baumberger, et al., New J. Phys. **12**, 023004 (2010).

[108] M. Guzzo, G. Lani, F. Sottile, P. Romaniello, M. Gatti, J. Kas, J. Rehr, M. Silly, F. Sirotti, and L. Reining, Phys. Rev. Lett. **107**, 166401 (2011).

[109] M. Guzzo, J. J. Kas, F. Sottile, M. G. Silly, F. Sirotti, J. J. Rehr, and L. Reining, Eur. Phys.J.B **85** (2012).

[110] W. Meevasana, X. Zhou, S. Sahrakorpi, W. Lee, W. Yang, K. Tanaka, N. Mannella, T. Yoshida, D. Lu, Y. Chen, et al., Phys. Rev. B **75**, 174506 (2007).

[111] S. L. Weng, E. W. Plummer, and T. Gustafsson, Phys. Rev. B **18**, 1718 (1978).

[112] H. Levinson, E. Plummer, and P. Feibelman, Phys. Rev. Lett. **43**, 952 (1979).

[113] J. van Mechelen, D. van der Marel, C. Grimaldi, A. Kuzmenko, N. Armitage, N. Reyren, H. Hagemann, and I. Mazin, Phys. Rev. Lett. **100**, 226403 (2008).

[114] L. Mattheiss, Phys. Rev. B **6**, 4740 (1972).

[115] Y. Tokura, Y. Taguchi, Y. Okada, Y. Fujishima, T. Arima, K. Kumagai, and Y. Iye, Phys. Rev. Lett. **70**, 2126 (1993).

[116] K. Szot and W. Speier, Phys. Rev. B **60**, 5909 (1999).

[117] G. Ketteler, S. Yamamoto, H. Bluhm, K. Andersson, D. Starr, D. Ogletree, H. Ogasawara, A. Nilsson, and M. Salmeron, J. Phys. Chem. C **111**, 8278 (2007).

[118] M. Knapp, D. Crihan, A. Seitsonen, E. Lundgren, A. Resta, and J. Andersen, J. Phys. Chem. C **111**, 5363 (2007).

[119] S. Yamamoto, O. T. Kendelewicz, J. T. Newberg, G. Ketteler, D. E. Starr, E. R. Mysak, K. J. Andersson, H. Ogasawara, H. Bluhm, M. Salmeron, et al., J. Phys. Chem. C **114**, 2256 (2010).

[120] P. Liu, T. Kendelewicz, G. E. Brown, and G. A. Parks, Surf. Sci. **412/413**, 287 (1998).

[121] S. Tanuma, C. J. Powell, and D. R. Penn, Surf. Interface Anal. **21**, 165 (1994).

[122] H. Qiu, B. Meyer, Y. Wang, and C. Wöll, Phys. Rev. Lett. **101**, 1 (2008).

[123] D. G. Thomas and J. J. Lander, J. Chem. Phys. **25**, 1136 (1956).

[124] H. Morkoç and U. Özgur, *Zinc Oxide: Fundamentals, Materials and Device Technology.* (WILEY-VCH Verlag GmbH & Co. KGaA, Weinheim, 2009).

[125] K. Shimada, M. Arita, Y. Takeda, H. Fujino, K. Kobayashi, T. Narimura, H. Namatame, and M. Taniguchi, Surf. Rev. Lett. **09**, 529 (2002).

[126] H. Hayashi, K. Shimada, J. Jiang, H. Iwasawa, Y. Aiura, T. Oguchi, H. Namatame, and M. Taniguchi, Phys. Rev. B **87**, 035140 (2013).

[127] H. Iwasawa, Y. Yoshida, I. Hase, K. Shimada, H. Namatame, M. Taniguchi, and Y. Aiura, Phys. Rev. Lett. **109**, 066404 (2012).

[128] K. Ozawa, T. Sato, Y. Oba, and K. Edamoto, J. Phys. Chem. C **111**, 4256 (2007).

[129] M. Kawasaki, K. Takahashi, and T. Maeda, Science **266**, 1540 (1994).

[130] G. Zwicker and K. Jacobi, Solid State Commun. **54**, 701 (1985).

[131] K. C. Waugh, Catalysis Today **15**, 51 (1992).

[132] C. Klingshirn, J. Fallert, H. Zhou, J. Sartor, C. Thiele, F. Maier-Flaig, D. Schneider, and H. Kalt, Phys. Status Solidi B **247**, 1424 (2010).

[133] N. Kislov, J. Lahiri, H. Verma, D. Y. Goswami, E. Stefanakos, and M. Batzill, Langmuir **25**, 3310 (2009).

[134] K. Kawano, M. Komatsu, Y. Yajima, H. Haneda, H. Maki, and T. Yamamoto, Appl. Surf. Sci. **189**, 265 (2002).

[135] C. Li, D. Feng, T. Jia, H. Sun, X. Li, S. Xu, X. Wang, and Z. Xu, Solid State Commun. **136**, 389 (2005).

[136] M. A. Versteegh, T. Kuis, H. T. C. Stoof, and J. I. Dijkhuis, Phys. Rev. B **84**, 035207 (2011).

[137] J. R. Schneck, E. Bellotti, P. Lamarre, and L. D. Ziegler, Appl. Phys. Lett. **93**, 102111 (2008).

[138] E. Magoulakis, E. L. Papadopoulou, E. Stratakis, C. Fotakis, and P. A. Loukakos, Appl. Phys. A **98**, 701 (2010).

[139] T. Shimizu, K. Yamamoi, E. Estacio, T. Nakazato, K. Sakai, N. Sarukura, D. Ehrentraut, T. Fukuda, M. Nagasono, T. Togashi, et al., Rev. Sci. Instrum. **81**, 033102 (2010).

[140] M. Kano, A. Wakamiya, K. Sakai, K. Yamanoi, M. Cadatal-Raduban, T. Nakazato, T. Shimizu, N. Sarukura, D. Ehrentraut, and T. Fukuda, J. Cryst. Growth **318**, 788 (2011).

[141] K. Vanheusden, W. L. Warren, C. H. Seager, D. R. Tallant, J. a. Voigt, and B. E. Gnade, J. Appl. Phys. **79**, 7983 (1996).

[142] Structure drawn by VESTA, K. Momma and F. Izumi, J. Appl. Crystallogr. **44**, 1272 (2011).

[143] M. Oshikiri, K. Takehana, T. Asano, and G. Kido, Phys. B Condens. Matter **216**, 351 (1996).

[144] Y. Imanaka, M. Oshikiri, K. Takehana, T. Takamasu, and G. Kido, Phys. B Condens. Matter **298**, 211 (2001).

[145] D. Ehrentraut, H. Sato, Y. Kagamitani, H. Sato, A. Yoshikawa, and T. Fukuda, Prog. Cryst. Growth Charact. Mater. **52**, 280 (2006).

[146] Ü. Özgür, Y. I. Alivov, C. Liu, A. Teke, M. A. Reshchikov, S. Doğan, V. Avrutin, S.-J. Cho, and H. Morkoç , J. Appl. Phys. **98**, 041301 (2005).

[147] J. B. Baxter and C. A. Schmuttenmaer, J. Phys. Chem. B **110**, 25229 (2006).

[148] A. Teke, U. Özgür, S. Doan, X. Gu, H. Morkoç, B. Nemeth, J. Nause, and H. Everitt, Phys. Rev. B **70**, 195207 (2004).

[149] K. Ueno, S. Nakamura, H. Shimotani, a. Ohtomo, N. Kimura, T. Nojima, H. Aoki, Y. Iwasa, and M. Kawasaki, Nat. Mater. **7**, 855 (2008).

[150] F. Stern, Phys. Rev. B **5**, 4891 (1972).

[151] J.-P. Zöllner, H. Übensee, G. Paasch, T. Fiedler, and G. Gobsch, Phys. Status Solidi (B) **134**, 837 (1986).

[152] G. Paasch and H. Übensee, Phys. Status Solidi (B) **113**, 165 (1982).